Preparation and Impedance Spectroscopy of Hybrid Structures Based on CuIn$_3$Se$_5$ Photoabsorber

KRISTJAN LAES

TUT PRESS

TALLINN UNIVERSITY OF TECHNOLOGY
Faculty of Chemical and Materials Technology
Department of Material Science

Dissertation was accepted for the defence of the degree of Doctor of Philosophy in Natural and Exact Sciences on January 29, 2010

Supervisors: Dr. Sergei Bereznev, Department of Material Science, Tallinn University of Technology

Prof. Andres Öpik, Department of Material Science, Tallinn University of Technology

Opponents: Prof. Marc Burgelman, University of Gent, Department of Electronics and Information Systems (ELIS), Pietersnieuwstraat 41, B-9000 Gent, Belgium

Prof. Enn Lust, University of Tartu, Institute of Chemistry, 14a Ravila St., 50411 Tartu, Estonia

Defence of the thesis: March 19, 2010

Declaration:

Hereby I declare that this doctoral thesis, my original investigation and achievement, submitted for the doctoral degree at Tallinn University of Technology has not been submitted for any academic degree.

Hübriidsete CuIn$_3$Se$_5$ fotoabsorberstruktuuride valmistamine ja impedantsispektroskoopia

KRISTJAN LAES

TTÜ
KIRJASTUS

In memory of my grandparents

TABLE OF CONTENTS

INTRODUCTION, THE AIM OF THE STUDY AND OUTLINE OF THE WORK

The modern market of photovoltaics includes mainly solar cells and panels based on the silicon photoabsorber and also on the basis of CdTe, CISe and others prospective photoabsorbers.

CISe and CdTe have attracted with the idea of cheaper processability and almost minimal amount of the physical material needed for creating structures of electronic conversion of light energy. Years of intensive labor with these materials towards and inexpensive solar energy converter have realized for now with production lines of such thin film CISe (and CdTe) devices, but on the other hand the expenses of production of the silicon based solar cells have also reduced. The fundamental advantage of CISe and CdTe is the applicability of such devices in space where usual silicon based devices tend to degrade remarkably. This means that CISe and CdTe should have a great future after the wireless energy transfer over distances in space, that would realize solar energy farms in the space, becomes reality. For having such an important value in earthly applications, a major kind of breakthrough must be accomplished to become competitive with silicon devices. At the moment the market share of thin film solar cells is about 7%. The success in achieving a bigger market share may appear because of lower installation costs. In fact costs for the installation, maintenance and site are in the same order as costs for the material and production. Thin film solar cells can be possibly integrated with various types of building materials, so reducing the prize for the site and installation.

Another type of absorber materials, those have been considered as cheap and suitable for flexible devices, are organic absorbers of conductive polymers, oligomers, organic dyes etc. For example, these materials are expected to provide the basis for the energy needs of the wearable electronics. As a combination with inorganic materials such as CdTe, CISe or Si, these materials provide the type of hybrid devices, which can be studied to broaden the understanding of principles that make a way for the creation of an efficient solar cell.

In this work an attempt is made to introduce a further development of the impedance spectroscopy (IS) method suitable for materials research for the PV applications. As a source of the data and the object of analysis there are used structures of pulsed laser deposited (PLD) and high vacuum evaporated (HVE) $CuIn_3Se_5$ photoabsorbers on ITO substrates with appropriate functional layers.

PLD $CuIn_3Se_5$ layers were prepared and partially characterized by the XRD and UV-VIS spectroscopy in the Department of Chemistry of Saint-Petersburg State University. The morphology and *I-V* investigation was performed in our Lab. For obtaining suitable rectifying contacts for the IS measurements and the hybrid

structure preparation, zinc phtalocyanine (ZnPc) functional layers were deposited by our group by using the HVE method.

The structures based on HVE $CuIn_3Se_5$ layers were prepared in our Lab by using the stoichiometric polycrystalline substrates synthesized in the Saint-Petersburg State University. As-deposited layers of the $CuIn_3Se_5$ were annealed in Ar atmosphere in glove box and studied by the EDS technique for elemental composition, XRD analysis for phase composition, Raman spectroscopy for the surface phase composition and SEM for the investigation of morphology and the thickness of obtained layers.

Three general ideas concerning IS were combined together to form up a calculation method that would possibly in most detail meet the needs of the photoabsorber material research.

1)   Constant phase element (CPE) behavior of the impedance response is accepted as an experimental fact and the equivalent circuit used for the analysis of the IS is constructed purely of CPE elements

2)   The frequency behavior of parameters of circuit elements is assumed in contrast to the ordinary constant parameter approach. This means that the circuit parameter fitting is obtained in the sliding mode of impedance analysis where the frequency range of impedance response is shrank into some minimum (about one decade of frequency) range. This range is then slide over the impedance spectrum to obtain the circuit elements frequency behavior.

3)   The parameters of the CPE obtained are used to extract the resistive and capacitive properties in terms of the physically meaningful dimensions of resistance and capacitance. For this reason a general consideration is discussed according to what any CPE can be converted into two complementary CPE in series or in parallel configuration if the parameters of those complementary CPE can be fixed.

The conversion of the CPE is analyzed in terms of the comparison of the magnitudes of the two complementary CPE. For the most general approach the same idea is applied both for magnitudes and phases of the impedances of these complementary CPE, but this general situation is only highlighted her as the possible option for the further study. This approach of complementary CPE is based on the most trivial assumption according to what any impedance can be represented in terms of the single CPE with appropriate parameters. This means that a single CPE is an equivalent representation of impedance besides of $|Z|$ vs. φ and $Im(Z)$ vs. $Re(Z)$ representation. At the same time a circuit consisting of many CPE with different exponential parameters is a distinguishable network [52].

The results of the conversion are then tested with the help of the values of differential resistance calculated from the experimental *I-V* curves. The match of the values of the differential resistance at low frequency part of the IS spectrum

calculated from the conversion and the values of the differential resistance calculated from experimental I-V curves is the criterion of the falsification for the calculation method proposed here.

The similar test for the results of the capacitance calculations would be possible if coulonometric measurements of Q-V curves would be available. Instead there is used somewhat incorrect option where the high frequency capacitance is used for estimating the thickness of the structure. The thickness obtained using the value of capacitance should match with the experimental thickness reported from the scanning electron microscopy (SEM).

In such a conversion a modula CPE appears together with the pure resistance or capacitance. Such modula CPE are brought together into the modula impedance in terms of the comparison of the parallel resistance and capacitance (RC) impedance. The physical meaning of such a modula impedance is not discussed in this work but possibly this may be attributed to the polycrystalline nature of the structure where the physical processes of charge accumulation and current in interiors of the crystals, at contacts and surfaces of such crystals form up a unique impedance behavior.

The genesis of the proposed method is traceable in the Results and Discussions part of the work.

First, in the case of the analysis of the structure of glass/ITO/PLD $CuIn_3Se_5$/ZnPc, there is used the sliding mode of the IS fitting, but only purely RC circuit is used even if this is clear that such a RC circuit is not very good approach for the analysis.

The second step appears if the structure of newly deposited glass/ITO/HVE $CuIn_3Se_5$/graphite is analyzed with the help of both the admittance spectroscopy (AS) and the IS. In the analysis of IS there is used a circuit of CPE, but the sliding mode of the modeling and the CPE conversion are not used. Instead a qualitative interpretation of the results is made. For the physical parameters calculation a simple AS calculations in the form of the C-V measurement interpretation is used.

Finally the structure of the aged glass/ITO/HVE $CuIn_3Se_5$/graphite is analyzed with all aspects proposed in the description of the method.

At the end of the discussions there is proposed a possible method for calculation of the majority carriers mobility based on the IS measurements.

LIST OF PUBLICATIONS

The thesis is based on the following papers referred to in the text by the Roman numerals:

Paper I. Tverjanovich, A.; Bereznev, S.; Borisov, E.N.; Kim, D.; Kois, J.; **Laes, K**.; Volobujeva, O.; Öpik, A.; Mellikov, E.; Tveryanovich, Yu.S. Polycrystalline $CuIn_3Se_5$ thin film photoabsorber deposited by pulsed laser deposition technique, Proceedings of the Estonian Academy of Sciences. 2009, 58, 1, 24–28.

Paper II. Laes, K.; Bereznev, S.; Tverjanovich, A.; Borisov, E.N.; Varema, T.; Volobujeva, O.; Öpik, A. Shallow defect density determination in $CuIn_3Se_5$ thin film photoabsorber by impedance spectroscopy, Thin Solid Films, 517 (2009) 2286–2290.

Paper III. Laes, K.; Bereznev, S.; Land, R.; Tverjanovich, A.; Volobujeva, O.; Traksmaa, R.; Raadik, T.; Öpik, A. The impedance spectroscopy of $CuIn_3Se_5$ photoabsorber films prepared by high vacuum evaporation technique. Energy Procedia, accepted for publication.

In the appendix of the thesis, copies of these papers have been included.

THE AUTHOR'S CONTRIBUTION TO PUBLICATIONS

The contribution by the author to the papers included in the thesis is as follows:

Paper I Carrying out a minor part of the experimental work, participation in data processing and in the discussion of the results, minor role in writing.

Paper II Carrying out a part of the experimental work, main role in data processing, participation in the discussion of the results, major role in writing.

Paper III Carrying out a main part of the experimental work, main role in data processing, participation in the discussion of the results, major role in writing.

ACKNOWLEDGEMENTS

I would like to express my gratitude to all my colleagues for the contribution to this work. My special thanks belong to the following:

My supervisor senior researcher Dr. Sergei Bereznev together with Prof. Andres Öpik for encouraging me to bring my doctoral studies to the procedure of defense, for useful discussions and continuous support. Also I would like to thank Prof Enn Mellikov for his support and for introducing me with Prof Marc Burgelman of Gent University of Belgium.

Prof. Marc Burgelman from Gent University of Belgium for inviting me to Gent in fall 2007 and for useful discussions there and later via very many emails.

Dr. Andrey Tverjanovich from the University of Saint-Petersburg for the synthesis of the $CuIn_3Se_5$ polycrystals and preparation of the $CuIn_3Se_5$ photoabsorber layers by using the PLD technique.

Dr. Raul Land from the Institute of Electronics, TUT who helped me to measure impedance and to make circuit modeling. I really appreciate his help and critical ideas then discussing ideas about impedance analysis.

I would also thank other people from the Department of Electronics, TUT for their friendly attitude and help in many possible issues concerning the impedance measurements and electronics in broader sense. These people are prof. Mart Min, Dr. Toomas Parve, Prof. Enn Velmre, Dr. Eero Haldre, Dr. Jaan Ojarand, Dr. Paul Annus and Dr. Andres Udal.

There were many instances then I needed some help in mathematics. D.Sc Ülle Kotta from the Institute of Cybernetics, Dr. Mati Väljas, Prof. Eugen Paal and Dr. Alar Leibak from the Institute of Mathematics helped me to have answers about finding analytical solutions in case of systems of nonlinear equations.

There are many people whose I have never met face to face, but still they have helped me really a lot. They are collaborators from the Mathcad Collaboratory who explained me how to use the calculation software of Mathcad. They are J.M. Giraud, Tom Gutman, Fred Kohlhepp, Richard Jackson.

I would also like to thank Prof. Jüri Krustok, MSc Mati Danilson, Dr. Jaan Hiie, Dr. Arvo Mere, MSc Atanas Katerski, MSc Erki Kärber, Dr. Vello Valdna for their friendly attitude and help in connection of this work.

LIST OF SYMBOLS AND ABBREVIATIONS

ac – alternating current

AS – admittance spectroscopy

CISe – copper indium selenide

CIGSe – copper indium gallium selenide

C_p, C_s – different capacitors in parallel

CPE – constant phase element

CPE-C_p, CPE-C_s – different capacitor-like constant phase elements in parallel

CPE-L_s – inductor-like constant phase element in series

CPE-R_p, CPE-R_s – different resistor-like constant phase elements in parallel

dc – direct current

EDS – energy dispersive spectroscopy

HVE – high vacuum evaporation

IS – impedance spectroscopy

ITO – indium tin oxide

L_s – inductor in series

PLD – pulsed laser deposition

R_p – resistor in parallel

R_s – resistor in series

SEM – scanning electron microscopy

XRD – X-ray diffraction spectroscopy

B – parameter of difference of the constant phase element exponential factors, dimensionless

C – Capacitance, Farad

D – discriminant value, dimensionless

E – proportionality parameter, dimensionless

E_g – band gap, eV

ε – dielectric permittivity, F/m

ε_0 – vacuum dielectric permittivity, F/m

ε_s – relative dielectric permittivity, dimensionless

f – frequency, Hz

I – current, Amps

j – imaginary unit

L – thickness of the material segment, m

μ – charge carriers mobility, cm^2/Vs

N_a, N_p, ρ – shallow level defect concentration, cm^{-3}

n, n_1, p, t – exponential parameter of the constant phase element, dimensionless

ω – angular frequency, rad/s

Q, Q_1, Q_2 – parameter of the constant phase element, $[C/(V \cdot s^{(1-p)})]$

q – elementary charge, coulomb

R – resistance, Ohm

S – surface area of the contact, m^2

s – an intermediate parameter, dimensionless

σ – conductivity, S/m

V_{bi} – built in potential, Volt

w – width of the material, m

1. LITERATURE REVIEW, THE AIM OF THE STUDY AND THE THEORY OF THE IMPEDANCE SPECTROSCOPY CALCULATIONS

1.1. CISe MATERIAL AND CHALLENGES

CuInSe$_2$ was synthesized for the first time by the Hahn in 1953 [1, 3]. In 1974, this material was proposed as a photovoltaic material by the group working in Bell Laboratories [1, 2 – 4] with a power conversion efficiency of 12% for a single crystal cell. The first CuInSe$_2$ solar cells were made by evaporating n-type CdS onto p-type single crystals of CuInSe$_2$ [4]. The first thin-film CuInSe$_2$/CdS devices were fabricated by Kazmerski et al using films deposited by evaporation of CuInSe$_2$ powder along with excess Se [2, 5].

In 1980 to 1982 the Boeing Corp boosted the efficiencies of thin film solar cells obtained from a three-source co-evaporation from 5.7% [1, 6] to over 10% [1, 7]. The basic solar cell configuration implemented by Boeing provided the basis for a series of improvements that have lead to the high-efficiency technology of today. The most important improvements include the following:

1) The absorber-layer band gap was increased from 1.02 eV for CuInSe$_2$ to 1.1–1.2 eV by partial substitution of In with Ga, leading to a substantial increase in efficiency [2, 8]

2) The 1-2 μm thick doped (CdZn)S layer was replaced with a thin, ≤50 nm, undoped CdS and a conductive ZnO current-carrying layer [2, 9], leading to the increase of the cell current by increasing the short wavelength response.

3) Ceramic or borosilicate substrates were replaced by soda lime glass that turned out to be beneficial because of the indiffusion of the sodium from the glass [2, 10]

4) Advanced absorber fabrication processes were developed that incorporate band gap gradients that improve the operating voltage and current collection [2, 11].

This result was then surpassed in 1987 by Arco Solar with a long standing record efficiency for a thin film cell of 14.1% [1, 12]. They used the selenisation of stacked metal layers by H$_2$Se. The reproducibility of this achievement was poor and it took ten further years to Arco Solar (later Siemens Solar Industries in USA, now Shell Solar). In 1998 they produced the first commercially available Cu(In, Ga)Se$_2$ solar modules [1].

In that time many enterprises, like Global Solar and ISET in USA, joined the industry concerned about CIGSe. In Germany the Würth Solar begun the

production of CISe modules in year 2000 and they are one of the leading manufacturers today.

Then NREL demonstrated cell efficiency of 18.8% on a 0.5 cm^2 laboratory cell in 1999 [1, 13]. At the same time 14.7% for mini modules with an area of around 20 cm^2 was demonstrated by Siemens Solar [1, 14] and Angstrom Solar Centre in Sweden [1, 15]. The production lines were launched in Japan by Showa.

Almost in ten years the record efficiency has changed about 1.1%. On 24 March 2008, the NREL announced in their website a new record of 19.9% efficiency of the copper indium gallium diselenide thin film solar cell [16].

In contrast to all other solar cell technologies, the research on CIGSe has no backup from other applications of the same material. As a consequence, the body of knowledge on CIGSe is still slight compared with what is known about crystalline Si, which can draw on ample reserves of knowledge from microelectronic research.

The understanding of CISe thin films, as used in photovoltaic devices, is primarily based on studies of its base material, pure $CuInSe_2$ [2, 17-19].

1.2. $CuIn_3Se_5$ AS AN ABSORBER MATERIAL

In earlier studies there was proposed that the ordered defect compound (ODC) on the surfaces of $CuInSe_2$ solar cells may be the reason of the high efficiency [20, 23]. The explanation was that there is an internal p-n junction between $CuInSe_2$ that is of p-type and a certain ODC. This ODC was expected to be the n-type $CuIn_3Se_5$. In papers, published later, this idea has disappeared, and this is only reflected in literature reviews of the papers specially dedicated to the issues of $CuIn_3Se_5$ [1, 24].

Basically this material has been studied as an option for the ternary system of $Cu(InGa)Se_2$. The fact is that while the $Cu(InGa)Se_2$ is far most successful thin film absorber today, it does not have an optimal bandgap which is expected to lie in the range of 1.1 and 1.7 eV [24]. The $CuIn_3Se_5$ has been reported to have band gap values in the range from 1.20 to 1.31 eV [20, 21, 22, 36], which are distinctly different from those of $CuInSe_2$ (0.9–1.04 eV).

Another important property of $CuIn_3Se_5$ is that it is of n-type conductivity [37, 38]. This is an option for the buffer layer issues considering CdS that is recently used in the best thin film solar cells.

Besides the environmental issues of Cd, there is pointed out that there is needed a buffer layer with an higher band gap energy to minimize optical losses in the buffer [39]. A n-type $CuIn_3Se_5$ could offer here a possibility of using buffers of p-

type. Besides inorganic buffer layers also organic semiconductors of p-type can be used. These properties allow the possibility that the absorber of $CuIn_3Se_5$ can be a basis for optional photovoltaic structures not developed yet.

1.3. COMMON DEPOSITION METHODS OF THE CISe COMPOUNDS

Two most common deposition methods are the vacuum co-evaporation method and the selenisation method [1, 24].

The co-evaporation method is the most precisely controllable method and this gives the most efficient mini-modules in the laboratory scale. In this method the elemental sources are used in the deposition and the composition is carefully tuned by controlling the deposition rates from individual elemental sources. At the same time the substrate is heated and different temperature programs are applied. This is a single step process where the material deposition and the film formation is held in one technological step. The up-scaling of this method is difficult and is far most expensive compared with other methods [1, 2, 24].

In selenisation method the stacked layers of Cu, In and Ga are deposited on a suitable substrate and then the selenisation takes place under H_2Se or Se and the thermal process is applied for elemental segregation. This is a two step process where the first is the step where the material is deposited and then the film formation takes place in the second step. In the production scale this method is much more favorable and there is really not much difference in the efficiencies of solar cells if compared with solar cells obtained with the co-evaporation method [1, 24].

Other two-step processes count for electrodeposition [25], thermal or electron beam evaporation [26], screen printing [27] and particle deposition [28, 1, 2]. Such precursor films are then typically reacted in either H_2Se or Se vapor at 400 to 500°C for 30 to 60 min to form the best device quality material. Reaction in H_2Se has the advantage that it can be done at atmospheric pressure and can be precisely controlled, but the gas is highly toxic and requires special precautions for its use [2]. The precursor films can also be reacted in a Se vapor, which might be obtained by thermal evaporation to form the $CuInSe_2$ film [29]. A third reaction approach is rapid thermal processing (RTP) of either elemental layers, including Se [30, 31] or amorphous evaporated Cu-In-Se layers [32].

The primary advantages of two-step processes for $CuInSe_2$ deposition are the ability to utilize more standard and well-established techniques for the metal deposition, reaction and anneal steps and to compensate for long reaction times with a batch processing mode or RTP of Se containing precursors. Composition and uniformity are controlled by the precursor deposition and can be measured

between the two steps. The biggest drawback to these processes is the limited ability to control composition and increase band gap, which may limit device and module performance. Other difficulties that must be overcome include poor adhesion and the use of hydrogen selenide, which is hazardous and costly to handle [2].

The pulsed laser deposition (PLD) is a modern application of lasers in material technology. Immediately after the high-power ruby laser became available it became clear that materials could be vaporized very easily with laser beam and this could be used for deposition of thin films. This idea was demonstrated first by Smith and Turner in 1965 [33]. The laser is used in such a deposition as a source of energy in the form of monochromatic and coherent photons. The PLD is so versatile that with the choice of an appropriate laser, it can be used to grow thin films of any kind of material [34]. Unlike ions or electrons, laser beams are much easier to transport and manipulate. Since laser interaction with gas-phase species is relatively weak, the dynamic range of deposition pressures is the largest compared to virtually any deposition process. The ability of the technique to reproduce the target composition with relative ease under the appropriate conditions is one of the key features. The spatial confinement of the laser-target interaction and the subsequent confined evaporant make this an inherently clean process unlike many other evaporation processes, where the evaporant tends to become in contact with various surfaces inside the chamber, thereby contributing to the contaminants in the film.

One of the major concerns regarding PLD in the early stages has been the ability of scaling up the process to cover large areas. Another concern is the capital cost of the laser [34].

The material deposition and the film formation can be completed in a single step in the vacuum chamber. The film composition can be tuned in some extent by controlling the energy of the laser pulses, but basically the precursor material must be optimized before the deposition.

The thermal evaporation or vacuum evaporation or the high vacuum evaporation (HVE) is one of the oldest techniques for depositing thin films, but it is still widely used in laboratory and industry for depositing metal and metal alloys [35]. It is one of the most common methods of physical-vapor deposition (PVD) together with e-beam evaporation, plasma spray deposition and sputtering [51]. Evaporation occurs when the source is heated above its melting point or till sublimation point in an evacuated chamber. The evaporated atoms then travel at high velocity in straight-line trajectories. The source can be evaporated by resistance heating, by radio frequency heating, or with a focused electron beam. The elemental or stoichiometric precursors can be used. The material deposition and the film formation can be completed in a single step in a vacuum chamber. The advantage of such a method is that virtually any compound which does not degrade

during evaporation can be deposited. On the other hand an appropriate vacuum system is essential for obtaining good results.

1.4. IS MEASUREMENTS AND INTERPRETATIONS

Commonly there are two main approaches for IS data available with the use of variety of devices capable for the measurement of the impedance frequency response.

The first approach is called an impedance spectroscopy and it uses an electrical circuit analysis of the objects under discussion. This approach introduces circuits with many (two or three and more) circuit elements that model the electrical impedance in the frequency range available in the measurement. Parameters of these circuit elements are usually constants that do not depend on frequency. This practice is widely used by many groups and in many areas of the electrical research. One of the most prominent books on this approach is compiled by E. Barsoukov and J. Ross Macdonald [40]. The Non-linear Least Squares Fitting is used as a mathematical method for finding the best match of the parameters and the experimental impedance data.

The second approach is called an admittance spectroscopy. This uses also electrical circuits for modeling the impedance response but here complex circuits are not used. Instead circuits of two or three elements are used. The parameters of these circuits are then calculated for every measurement frequency using the analytical solutions that relate the measured impedance with two parameters of the circuit elements.

More commonly this approach was widely used in earlier practice of impedance measurements when fully automated impedance spectrometers were not common and acquisition of data from extensive ranges of frequency was very tedious, if not impossible.

At the same time the admittance spectroscopy is very useful for semiconductor investigations and many researchers on the field of solar cell research are using the admittance spectroscopy as the tool for predicting majority carriers profiles [41, 42], for studying deep level defects concentrations, deep level defects energy states in the band gap [43–46], surface charge properties and concentrations [46], and majority carriers mobilities [47].

In both cases the parameters fitted to the spectra or calculated from the spectra are then analyzed using suitable physical models. A well adopted approach in the field of the research of the solar cells is that the frequency dependencies of circuit elements like capacitance are analyzed using modeling programs together with

complementary data from other types of measurements. A SCAPS program may be here as an example [48].

The third approach as an option of analyzing impedance data is somewhat less exploited. This approach is based on the concept of the distribution of the relaxation times. In this approach a system is studied as a kind of superposition of processes that give rise to various relaxation patterns and relaxation times. In contrast to the nonlinear leas squares curve fit of equivalent circuit models, there is made no a priori choice of the equivalent circuit. Only after the superposition of processes and relaxation times is resolved, the equivalent circuit can be concluded from such an interpretation. The paper of H. Schichlein et al [49] is here an example describing such an approach.

In this work there is used a method that combines the first approach of complex circuits and the second approach there the circuit elements are dependent on the frequency of the measurement signal. This means that the parameters of the complex circuit are calculated in the "sliding mode". In such a calculation the frequency range is diminished so that impedance results obtained only for one decade or less of frequency are used. This "window" of frequency is then slide over the entire range of frequencies. In every single position of the modeling process, a set of parameters is obtained and a characteristic frequency is calculated as a medium frequency in that range. A suitable fitting algorithm can be used here for finding the parameter set as in the ordinary complex circuit impedance analysis.

This approach tries to unite two apparent circumstances of the impedance phenomena: the parameters frequency dependence and the complexity of the circuit configuration

1.5. ELEMENTS OF THE CIRCUIT OF INTERPRETATION

Physical models, that can be applied to structures studied with the help of IS, can make use of parameters like resistance, capacitance and inductance. There also exist physical models of diffusion which do make use of various Warburg-like resistances [50].

As a generalization for a resistance, capacitance, inductance and semi infinite Warburg, there is a term coined as a constant phase element (CPE) and this leaves resistance, capacitance etc as a special cases.

In the practice of IS modeling there is very frequently observed a CPE behavior [51, 52]. There are also plenty of empirically constructed hypothesizes about the origin of the CPE behavior and this is a topic of controversy [53-56].

In this work an attempt is made there the general CPE behavior is subtracted into parallel or series connection of special CPE (capacitance or resistance) and a certain modula CPE.

It is worth of mentioning the official statement of IUPAC concerning the impedance modeling with equivalent circuits: ''it is definitely wrong to analyze experimental impedance data by just fitting it to an equivalent circuit'' [57].

1.6. CALCULATIONS OF A CAPACITANCE VALUES USING CPE

As it is known the impedance of the CPE is given by a formula

$$Z_{CPE} \equiv \frac{1}{(j \cdot \omega)^p \cdot Q} \qquad (1.6.1)$$

[51], where j is the imaginary unit, ω is the angular frequency [rad/s], p is an unitless parameter what can have values in the range of -1 to 1, Q is a positive parameter with the dimension depending on the value of p [C/(V·s$^{(1-p)}$)].

If $p = 1$, then Q has a dimension of capacitance (C/V·s^0). Also, if $p = 0$, then Q has a dimension of conductance (C/V·s^1). Finally, if $p = -1$, then Q has a dimension of reversed inductance (C/V·s^2).

From the dimensional analysis it concludes that

$$C \left[\frac{C}{V \cdot s^0} \right] \equiv Q \left[\frac{C}{V \cdot s^{(1-p)}} \right] \cdot [s^{(1-p)}] \equiv Q \cdot \left(\frac{1}{f} \right)^{(1-p)} \qquad (1.6.2)$$

$$R \left[\frac{V \cdot s^1}{C} \right] \equiv Q^{-1} \left[\frac{V \cdot s^{(1-p)}}{C} \right] \cdot [s^p] \equiv Q^{-1} \cdot \left(\frac{1}{f} \right)^p \qquad (1.6.3)$$

$$L \left[\frac{V \cdot s^2}{C} \right] \equiv Q^{-1} \left[\frac{V \cdot s^{(1-p)}}{C} \right] \cdot [s^{(1+p)}] \equiv Q^{-1} \cdot \left(\frac{1}{f} \right)^{(1+p)} \qquad (1.6.4)$$

there f is a frequency of the measurement signal (Herz), C is capacitance, R is resistance, L is inductance and the terms in square brackets refer to dimensions of corresponding quantities.

Every CPE has impedance consisting of real and imaginary part which can be found using the formula of Moivre

$$Z_{cpe} \equiv (j \cdot \omega)^{-p} \cdot Q^{-1} \equiv \omega^{-p} \cdot Q^{-1} \left[\cos \left(\frac{\pi}{2} \cdot -p \right) + j \cdot \sin \left(\frac{\pi}{2} \cdot -p \right) \right]$$

$$\equiv \omega^{-p} \cdot Q^{-1} \left[\cos \left(\frac{\pi}{2} \cdot p \right) - j \cdot \sin \left(\frac{\pi}{2} \cdot p \right) \right] \qquad (1.6.5)$$

and thus a single certain CPE can be converted into two arbitrarily chosen CPE in series or in parallel configuration if one equals the real and the imaginary parts of the corresponding configuration with the real and imaginary parts of the initial CPE (Fig. 1.6.1).
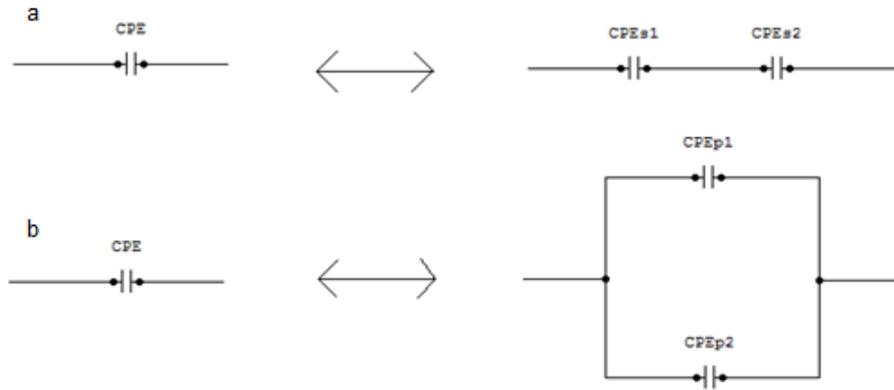
Fig. 1.6.1. Transformation of the CPE impedance or admittance into series (a) or parallel (b) configuration of two CPE-s (This transformation is invariant and reversible if the exponential parameters of the two new CPE-s can be fixed)

In purposes of this study it is important to choose these two CPE so that a capacitance could be calculated. For that reason it is reasonable to choose one of the two CPE´s as a CPE with $p=1$ in order to have a Q with the dimension of capacitance (C/V·s^0) (the exponential term of the second CPE is designated n here and further). The value of the n of the other CPE is not known *a priory* and possibilities of predicting this value must be found out.

In this work only the conversion into the parallel configuration of two CPE´s is considered, but the same principles apply equally to the series configuration of two CPE´s and similar results can be obtained there.

For such a conversion two equations are available that are derived from the equalities of the corresponding real and imaginary parts.

$$\omega^{-p}\cdot Q^{-1}\cdot\cos\left(\frac{\pi}{2}\cdot p\right) = \frac{Q1\cdot\left(\omega^n\cdot\cos\left(\frac{\pi}{2}\cdot n\right)\right)}{\left[Q1\cdot\left(\omega^n\cdot\cos\left(\frac{\pi}{2}\cdot n\right)\right)\right]^2 + \left[Q1\cdot\left(\omega^n\cdot\sin\left(\frac{\pi}{2}\cdot n\right)\right) + \omega\cdot C\right]^2} \quad (1.6.6)$$

and

$$\omega^{-p}\cdot Q^{-1}\cdot\sin\left(\frac{\pi}{2}\cdot p\right) = \frac{Q1\cdot\left(\omega^n\cdot\sin\left(\frac{\pi}{2}\cdot n\right)\right) + \omega\cdot C}{\left[Q1\cdot\left(\omega^n\cdot\cos\left(\frac{\pi}{2}\cdot n\right)\right)\right]^2 + \left[Q1\cdot\left(\omega^n\cdot\sin\left(\frac{\pi}{2}\cdot n\right)\right) + \omega\cdot C\right]^2} \quad (1.6.7).$$

In these equations C is a capacitance, n and Q_1 are the parameters of the second CPE.

These equations can be simplified while combining with each other and using trivial trigonometric identities and solved together to find solutions for C and Q_1. In this work the calculation package of symbolic solver of Mathcad 13 was used to obtain a solution in the symbolic form.

As the value of n is not known and can be in principle change in the range of -1 to +1, C and Q_1 cannot be predicted adequately. To overcome this problem and to give a possible solution to this problem there can be introduced an additional general identity.

For that reason we compare modules of those two new CPE impedances. It is trivial that at every frequency the relationship holds:

$$(E\cdot\omega\cdot C)^2 = Q1^2\cdot\left[\left(\omega^n\cdot\cos\left(\frac{\pi}{2}\cdot n\right)\right)^2 + \left(\omega^n\cdot\sin\left(\frac{\pi}{2}\cdot n\right)\right)^2\right] \qquad (1.6.8)$$

that can further simplified to the form

$$E\cdot\omega\cdot C = Q1\cdot\omega^n \qquad (1.6.8a).$$

This equation contains a proportionality coefficient E what simply states the fact that these two modules are linearly proportional.

Using the Eq. 1.6.8a together with Eqs. 1.6.6 and 1.6.7 a solution can be obtained in symbolic form for C, Q_1 and n.

While introducing the third equation, the fourth parameter E was also introduced and this parameter is also unknown.

But this parameter of E can be studied analytically and evaluated using the symbolic results obtained for C, Q_1 and n.

The solution of this equation system of three equations contains 8 sets of results for C, Q_1 and n.

As an example and a ground for the analysis there is given one of these solutions for n, C and Q_1, what turned out to be most appropriate for further calculations:

$$n = 2\cdot\frac{\text{atan2}\left(P1\cdot\frac{P2}{E}, \frac{P1\cdot P2\cdot s - 1}{E}\right)}{\pi} \qquad (1.6.9),$$

where

$$P1 = \frac{1}{2\cdot\left(1 + s^2\right)} \quad (1.6.9a) \text{ and } P2 = 2\cdot s + 2\cdot\left[(-1) + E^2 + s^2\cdot E^2\right]^{\frac{1}{2}} \quad (1.6.9b).$$

$$Q1 = \frac{-E}{e^{(-2)\cdot p\cdot\ln(\omega)}\cdot s^2 + e^{(-2)\cdot p\cdot\ln(\omega)}}\cdot M\cdot\frac{Q}{(E + 1)\cdot(E - 1)\cdot e^{\ln(\omega)\cdot n}} \qquad (1.6.10)$$

and

$$C = \frac{-1}{e^{(-2)\cdot p\cdot \ln(\omega)}\cdot s^2 + e^{(-2)\cdot p\cdot \ln(\omega)}}\cdot M\cdot \frac{Q}{(E+1)\cdot(E-1)\cdot \omega}$$ (1.6.11),

where

$$M = \left[e^{(-2)\cdot p\cdot \ln(\omega)}\cdot \left(s^2 + 1\right)\cdot \left[s^2\cdot E^2 + s^2 - 2\cdot s\cdot \left(s^2\cdot E^2 + E^2 - 1\right)^{\frac{1}{2}} - 1 + E^2\right]\right]^{\frac{1}{2}}$$ (1.6.12)

and

$$s = \tan\left(\frac{\pi}{2}\cdot p\right)$$ (1.6.13)

Function of atan2(x, y) is a definition of the Mathcad 13 calculation suit for arctan(y/x). Eqs. 1.6.9 to 1.6.13 represent precisely (there are different signs in basic parameter blocks) all 8 solutions in their basic constituents. It is clear that values for n, Q_1 and C can be obtained only then the conditions of discriminants are fulfilled.

The last coefficient of the parameter C, represents an E dependent discriminant that is the same in all solutions and study of this discriminant can reveal the range of E values there Q_1, C and n can have real values. Most obviously this coefficient contains another discriminant (designated as D_1 in Fig. 1.6.2) which must be studied as an equation of

$$s^2\cdot E^2 + E^2 - 1 = 0$$

Taking into account that the coefficient of

$$e^{(-2)\cdot p\cdot \ln(\omega)}\cdot \left(1 + s^2\right)$$

has always a positive value if s is real, the solution of this equation gives that C, can have real values only if

$$E \geq \frac{1}{\left(1 + s^2\right)^{\frac{1}{2}}}, E \leq \frac{-1}{\left(1 + s^2\right)^{\frac{1}{2}}}.$$

Now this coefficient of M (Eq. 1.6.12) can be studied as an equation of D_2 (Fig. 1.6.2)

$$s^2\cdot E^2 + s^2 - 2\cdot s\cdot \left(s^2\cdot E^2 + E^2 - 1\right)^{\frac{1}{2}} - 1 + E^2 = 0$$

The solution of it gives that $M=0$ if $E=\pm1$. The further investigation of this equation reveals that at $E=\pm1$ this function has a global minimums and also at $E=0$ it has a discontinuity point. All these conditions together show that C, is predicted in two ranges

$$-\infty < E \le \frac{-1}{\left(1+s^2\right)^{\frac{1}{2}}} \qquad \infty > E \ge \frac{1}{\left(1+s^2\right)^{\frac{1}{2}}}$$

and
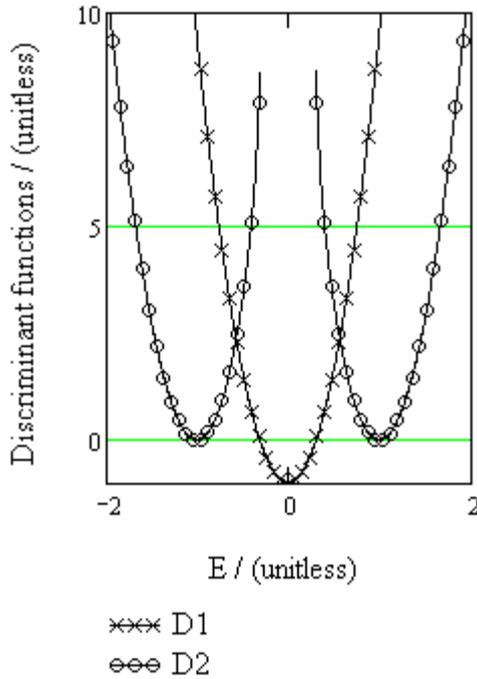
Fig. 1.6.2. Investigation of discriminant functions of C, if $s = \tan\left(\frac{\pi}{2} \cdot 0.8\right)$ (D_1 is the first discriminant function inside the second discriminant function D_2)

The results of the study of discriminants D_1 and D_2, for the situation when $s = \tan\left(\frac{\pi}{2} \cdot 0.8\right)$, are graphically represented on Fig. 1.6.2.

From the Eq. 1.6.9 there is also clear that $E \ne 0$. Also from Eqs. 1.6.11 and 1.6.12 there is clear that $E \ne \pm1$.

Taking into account all these restrictions and also noting that E can have physically only positive values we must conclude that Q_1, C and n can have real values in two ranges of E values, namely

$$\frac{1}{\left(s^2 + 1\right)^{\frac{1}{2}}} \leq E < 1 \qquad (1.6.14a)$$

and

$$1 < E < \infty \qquad (1.6.14b)$$

Obviously the condition 1.6.14a holds then the admittance module of C is greater than the module of the second CPE. Condition of 1.6.14b holds otherwise.

Further study of these 8 solutions show that only one of these equations gives physically reasonable results if values of E are changed according to the result of Eq. 1.6.14a. 4 solutions of all 8 give identical results and pass the test with initial CPE impedance if

$$E = \frac{1}{\left(1 + s^2\right)^{\frac{1}{2}}} \qquad (1.6.14c).$$

In calculations of capacitance only two solutions, give adequate results according to the whole range of Eq. 1.6.14a and one of them is used in further calculations. The decision was made upon how do results of capacitance behave if E approaches 1. In one of these solutions there is no limit for the capacitance value and it tends to increase infinitely while the other capacitance according to the second such a solution has a limiting value that cannot be exceeded. In our data no solution passed the test of comparing the initial impedance with newly calculated CPE values if the E values were chosen greater than 1.

Finally it is possible to solve the initial system of Eqs. 1.6.6, 1.6.7 and 1.6.8a in a special situation then $E=1$. Then there can be obtained a symbolic result consisting only of two solutions for C, Q_1 and n that are rather compact in form:

$$n = 2 \cdot \frac{\mathrm{atan2}\left(2 \cdot \frac{s}{s^2 + 1}, \frac{s^2 - 1}{s^2 + 1}\right)}{\pi} \qquad (1.6.15)$$

$$Q1 = \frac{1}{2 \cdot e^{(-2) \cdot p \cdot \ln(\omega)}} \cdot \left[e^{(-2) \cdot p \cdot \ln(\omega)} \cdot \left(s^2 + 1\right)\right]^{\frac{1}{2}} \cdot \frac{Q}{s \cdot \omega^n} \qquad (1.6.16)$$

$$C = \frac{1}{2 \cdot e^{(-2) \cdot p \cdot \ln(\omega)}} \cdot \left[e^{(-2) \cdot p \cdot \ln(\omega)} \cdot \left(s^2 + 1\right)\right]^{\frac{1}{2}} \cdot \frac{Q}{s \cdot \omega} \qquad (1.6.17)$$

These two solutions have the same expression for n but are opposite in sign for Q_1 and C.

Only one solution, namely the solution given here with Eqs. 1.6.15, 1.6.16 and 1.6.17, succeeds the test of comparison with the impedance of the initial CPE. On the other hand, values obtained with Eqs. 1.6.15, 1.6.16 and 1.6.17 represent limiting values of Eqs. 1.6.9, 1.6.10 and 1.6.11 respecitvely if $E \to 1$.

In the limit there

$$\lim_{E \to \frac{1}{\left(s^2+1\right)^{\frac{1}{2}}}} Q1, C, n$$

Eqs. 1.6.9, 1.6.10, and 1.6.11 transform into formulas

$$n = (-2)\cdot\frac{\text{atan}\left(\frac{1}{s}\right)}{\pi} \qquad (1.6.18),$$

$$Q_1 = Q\cdot\frac{\omega^{p-n}}{s} \qquad (1.6.19),$$

$$C = \left(1 + s^2\right)^{\frac{1}{2}}\cdot\omega^{p-1}\cdot\frac{Q}{s} \qquad (1.6.20)$$

respectively.

Taking into account these, one must conclude that Eq. 1.6.14a and 1.6.14b have a final form of

$$\frac{1}{\left(s^2 + 1\right)^{\frac{1}{2}}} \leq E \leq 1$$

$$(1.6.14\text{d}) \text{ and } 1 \leq E < \infty \quad (1.6.14\text{e}).$$

In case of depletion capacitance calculations and according to the Eq. 1.6.8a it is quite reasonable that E is less or equal than 1 because deviations from pure capacitive behavior are not expected to be too significant and so the admittance module of capacitance should exceed the module of a second CPE which physical origin is not clear here. The finding that test calculations succeed only if E values are chosen using the condition of Eq. 1.6.14d gives a support to the consideration that really the admittance modulus of capacitance is greater (or equal) than the admittance modulus of the second CPE. It must be noted that the forms of 1.6.14d and 1.6.14e are such that these two regions of E can be united into one. Still this is not possible according to the test calculations. This is probably due to the arguments of the atan2(x, y) function (arctan(y/x) function). This term is sensitive

28

respect to value of *s* (Eq. 1.6.13) and because of that can be either positive or negative. This question is unclear and there is only possible to rely on results obtained then testing the data that were obtained when modeling the results of measurements. These test show that there are two regions according to Eq. 1.6.14d and Eq. 1.6.14e that are not useable at least at the same time and in some reason must be separated from each other.

These considerations make it possible to estimate the values of capacitance from the initial CPE impedance which were obtained by fitting procedure and to calculate these capacitance values while using a suitable solution of the equation system consisting of Eqs. 1.6.6, 1.6.7, and 1.6.8a. At the same time it must be taken into account that the coefficient *E* can be possibly any value in the range described by Eq. 1.6.14d.

This means that without additional evidences about the system it is not possible to make precision calculations of capacitance but there is possible to estimate a range of capacitance values that are possible.

1.7. CALCULATIONS OF A RESISTANCE VALUES USING CPE

1.7.1. TRANSFORMATION OF THE RESISTANCE-LIKE CPE INTO THE SERIES CONNECTION OF THE RESISTOR AND THE MODULA CPE

Here the initial CPE is transformed into the series connection of the simple resistance *R* and a modula CPE (Fig. 1.6.1 a). Similarly to the previous chapter a system of corresponding equations together with the additional relationship about comparing magnitudes of the impedances of resistance *R* and modula CPE is arranged:

$$\omega^{-p} \cdot Q^{-1} \cdot \cos\left(\frac{\pi}{2} \cdot p\right) = \frac{R \cdot \left(\omega^n \cdot Q1\right) + \cos\left(\frac{\pi}{2} \cdot n\right)}{\omega^n \cdot Q1} \quad (1.7.1.1),$$

$$\omega^{-p} \cdot Q^{-1} \cdot \sin\left(\frac{\pi}{2} \cdot p\right) = \frac{\sin\left(\frac{\pi}{2} \cdot n\right)}{\omega^n \cdot Q1} \quad (1.7.1.2) \text{ and}$$

$$E \cdot R = \frac{1}{\omega^n \cdot Q1} \quad (1.7.1.3).$$

The symbolic solver of Mathcad 13 gives a result with 16 solutions for the values of *R*, *Q₁* and *n*:

$$n = 2 \cdot \frac{\text{atan2}\left(P1 \cdot \dfrac{P3}{E}, s \cdot \dfrac{1 + P1 \cdot P3}{E} \right)}{\pi} \quad (1.7.1.4),$$

$$Q1 = \frac{1}{e^{(-2) \cdot p \cdot \ln(\omega)} \cdot s^2 + e^{(-2) \cdot p \cdot \ln(\omega)}} \cdot M \cdot \frac{Q}{E \cdot e^{n \cdot \ln(\omega)}} \quad (1.7.1.5) \text{ and}$$

$$R = \frac{e^{(-2) \cdot p \cdot \ln(\omega)} \cdot s^2 + e^{(-2) \cdot p \cdot \ln(\omega)}}{\left[e^{(-2) \cdot p \cdot \ln(\omega)} \cdot \left(s^2 + 1\right) \cdot \left[s^2 \cdot E^2 - s^2 + E^2 + 1 + 2 \cdot \left(s^2 \cdot E^2 + E^2 - s^2\right)^{\frac{1}{2}} \right]^{\frac{1}{2}} \right]} \cdot Q \quad (1.7.1.6),$$

where

$$P3 = (-2) \cdot s^2 + 2 \cdot \left(s^2 \cdot E^2 + E^2 - s^2\right)^{\frac{1}{2}} \quad (1.7.1.4a),$$

$$M = \left[e^{(-2) \cdot p \cdot \ln(\omega)} \cdot \left(s^2 + 1\right) \cdot \left[s^2 \cdot E^2 - s^2 + E^2 + 1 + 2 \cdot \left(s^2 \cdot E^2 + E^2 - s^2\right)^{\frac{1}{2}} \right]^{\frac{1}{2}} \right] \quad (1.7.1.7)$$

and the P1 is defined as earlier.

The study of the inner discriminant in C, shows that C can have real values only if

$$\frac{-1}{\left(s^2 + 1\right)^{\frac{1}{2}}} \cdot s \le E \qquad E \le \frac{1}{\left(s^2 + 1\right)^{\frac{1}{2}}} \cdot s$$

and $\quad (1.7.1.8),$

where s is a negative number (Eq. 1.6.13 with the p negative).

Because E can be only positive, the first of these two equations can be used if s is negative and the second can be used if otherwise. If $E=1$, equations for n, Q_1 and R have a form

$$n = \frac{-\ln\left[\omega^{(-2) \cdot \frac{\text{atan2}\left[\dfrac{-\left(s^2 - 1\right)}{s^2 + 1}, 2 \cdot \dfrac{s}{s^2 + 1} \right]}{\pi}} \right]}{\ln(\omega)} \quad (1.7.1.9),$$

$$Q1 = \cfrac{2}{\left[\cfrac{atan2\left[\cfrac{-\left(s^2-1\right)}{s^2+1}, 2\cdot\cfrac{s}{s^2+1}\right]}{\pi}\right]^2}\cdot\cfrac{Q}{\left[e^{(-2)\cdot p\cdot\ln(\omega)}\cdot s^2 + e^{(-2)\cdot p\cdot\ln(\omega)}\right]^{\frac{1}{2}}}$$

(1.7.1.10)

and

$$R = \frac{1}{2}\cdot\frac{\left[e^{(-2)\cdot p\cdot\ln(\omega)}\cdot s^2 + e^{(-2)\cdot p\cdot\ln(\omega)}\right]^{\frac{1}{2}}}{Q}$$

(1.7.1.11)

respectively.
   If

$$E = \frac{-1}{\left(s^2 + 1\right)^{\frac{1}{2}}}\cdot s$$

(1.7.1.8a),

the solution for the n, Q_1 and R has a form

$$n = 2\cdot\frac{atan2\left[\cfrac{-1}{\left(K\cdot s^2 + K\right)^{\frac{1}{2}}}\cdot K^{\frac{1}{2}}\cdot s, \cfrac{1}{K^{\frac{1}{2}}\cdot\left(\omega^p\right)^2\cdot\left(K\cdot s^2 + K\right)^{\frac{1}{2}}}\right]}{\pi}$$

(1.7.1.12),

$$Q1 = \cfrac{1}{K^{\frac{1}{2}}}\cdot\cfrac{Q}{e^{2\cdot\ln(\omega)\cdot\cfrac{atan2\left[\cfrac{-1}{\left(K\cdot s^2+K\right)^{\frac{1}{2}}\cdot\left(\omega^p\right)^2\cdot K^{\frac{1}{2}}}\cdot s, \cfrac{1}{K^{\frac{1}{2}}\cdot\left(\omega^p\right)^2\cdot\left(K\cdot s^2+K\right)^{\frac{1}{2}}}\right]}{\pi}}}\cdot s$$

(1.7.1.13) and

$$R = \frac{\left(K\cdot s^2 + K\right)^{\frac{1}{2}}}{Q}$$

(1.7.1.14),

where

$$K = e^{(-2)\cdot p\cdot\ln(\omega)}$$

(1.7.1.15).

31

Study of the 8 solutions shows that the special solution in the form of Eq. 1.7.1.4-1.7.1.7 is the only solution that is applicable in the range of

$$\frac{-1}{\left(s^2+1\right)^{\frac{1}{2}}}\cdot s \le E < \infty$$

(1.7.1.8*b*),

while other solutions do not meet the test with initial CPE. Study of these solutions show that if $E \to \infty$ then $R \to 0$ while $Q1 \to Q$ and $n \to p$. There is also another solution available in the range of

$$\frac{-1}{\left(s^2+1\right)^{\frac{1}{2}}}\cdot s \le E \le 1$$

(1.7.1.8*c*)

but values of *n* are very exotic in this case (-2) if $E \ne E_{min}$ there E_{min} is calculated using Eq. 1.7.1.9a. Accordingly it is preferential that Eqs. 1.7.1.4-1.7.1.7 are used in the range given by Eq. 1.7.1.8b or even in range given by Eq. 1.7.1.8c.

1.7.2. TRANSFORMATION OF THE RESISTANCE-LIKE CPE INTO THE PARALLEL CONNECTION OF THE RESISTOR AND THE MODULA CPE

Here the initial CPE is transformed into the parallel connection of the simple resistance *R* and a modula CPE (Fig. 1.6.1 b). Similarly to the previous chapter a system of corresponding equations together with the additional relationship about comparing magnitudes of the admittances of the resistance *R* and the modula CPE is arranged:

$$\omega^{-p}\cdot Q^{-1}\cdot\cos\left(\frac{\pi}{2}\cdot p\right) = \frac{\frac{1}{R}+Q1\cdot\omega^n\cdot\cos\left(\frac{\pi}{2}\cdot n\right)}{\left(\frac{1}{R}+Q1\cdot\omega^n\cdot\cos\left(\frac{\pi}{2}\cdot n\right)\right)^2+\left(Q1\cdot\omega^n\cdot\sin\left(\frac{\pi}{2}\cdot n\right)\right)^2}$$

(1.7.2.1),

$$\omega^{-p}\cdot Q^{-1}\cdot\sin\left(\frac{\pi}{2}\cdot p\right) = \frac{Q1\cdot\omega^n\cdot\sin\left(\frac{\pi}{2}\cdot n\right)}{\left(\frac{1}{R}+Q1\cdot\omega^n\cdot\cos\left(\frac{\pi}{2}\cdot n\right)\right)^2+\left(Q1\cdot\omega^n\cdot\sin\left(\frac{\pi}{2}\cdot n\right)\right)^2}$$

(1.7.2.2) and

$$E\cdot\frac{1}{R} = Q1\cdot\omega^n$$

(1.7.2.3).

A symbolic solver of Mathcad 13 gives a result with 16 solutions for the values of R, Q_1 and n:

$$n = 2 \cdot \frac{\text{atan2}\left(P1 \cdot \dfrac{P3}{E}, s \cdot \dfrac{1 + P1 \cdot P3}{E} \right)}{\pi} \qquad (1.7.2.4),$$

$$Q_1 = \frac{E}{R} \cdot \frac{1}{\omega^n} \qquad (1.7.2.5) \text{ and}$$

$$R = \frac{1}{s^2 + 1} \cdot \frac{\left[\left(s^2 + 1\right) \cdot e^{(-2) \cdot p \cdot \ln(\omega)} \cdot \left[2 \cdot \left(s^2 \cdot E^2 - s^2 + E^2\right)^{\frac{1}{2}} - s^2 + 1 + s^2 \cdot E^2 + E^2 \right] \right]^{\frac{1}{2}}}{Q} \qquad (1.7.2.6).$$

The study of the inner discriminant in R shows that R can have real values only if

$$\frac{-1}{\left(s^2 + 1\right)^{\frac{1}{2}}} \cdot s \leq E \qquad E \leq \frac{1}{\left(s^2 + 1\right)^{\frac{1}{2}}} \cdot s$$

$$\text{and} \qquad (1.7.2.7),$$

where s is a real number.

Because E can be only positive, the first of these two equations can be used if s is negative and the second can be used if otherwise. If $E=1$, equations for n, Q_1 and R have a form

$$n = (-2) \cdot \frac{\text{atan}\left(2 \cdot \dfrac{s}{s^2 - 1} \right)}{\pi} \qquad (1.7.2.8),$$

$$Q_1 = \frac{1}{2} \cdot \left(1 + s^2\right)^{\frac{1}{2}} \cdot \frac{Q}{\left(\dfrac{\omega^{\frac{-\text{atan}\left(2 \cdot \frac{s}{s^2-1} \right)}{\pi}} }{} \right)^2} \cdot \omega^{-p} \qquad (1.7.2.9) \text{ and}$$

$$R = \frac{2}{\omega^p \cdot \left(1 + s^2\right)^{\frac{1}{2}} \cdot Q} \quad (1.7.2.10)$$

respectively.

If

$$E = \frac{1}{\left(s^2 + 1\right)^{\frac{1}{2}}} \cdot s \quad (1.7.2.7),$$

the solution for the n, Q_1 and R has a form

$$n = (-2) \cdot \frac{\text{atan}\left(\frac{1}{s}\right)}{\pi} \quad (1.7.2.11),$$

$$Q_1 = s \cdot \frac{Q \cdot \omega}{\left(e^{\frac{\text{atan}\left(\frac{1}{s}\right)}{\pi}}\right)^2 \cdot e^{-p}} \quad (1.7.2.12) \text{ and}$$

$$R = \frac{1}{\omega^p \cdot \left(1 + s^2\right)^{\frac{1}{2}} \cdot Q} \quad (1.7.2.13),$$

Study of the 8 solutions shows that the special solution in the form of Eq. 1.7.2.4-1.7.2.6 is the only solution that is applicable in the range of

$$\frac{1}{\left(s^2 + 1\right)^{\frac{1}{2}}} \cdot s \le E < \infty \quad (1.7.2.7b),$$

while other solutions do not meet the test with initial CPE. Study of these solutions show that if $E \to \infty$ then $R \to 0$ while $Q1 \to Q$ and $n \to p$.

1.8. CALCULATIONS OF THE SHALLOW LEVEL DEFECTS CONCENTRATIONS

The shallow level defect density calculations are made using two different theoretical approaches. The first is a well known approach derived from the depletion approximation assuming an abrupt space charge edge.

$$N(w) = -\frac{C_d^3}{q \cdot \varepsilon}\left(\frac{dC_d}{dV}\right)^{-1} \qquad (1.8.1),$$

where

$$w = \frac{\varepsilon}{C_d} \qquad (1.8.2).$$

Here $\varepsilon = \varepsilon_s \varepsilon_0$ (ε_s is the dielectric constant of the semiconductor and ε_0 is the vacuum constant), Q in the charge of the single electron, C_d is the differential capacitance per unit area and V is the applied potential. Eq. 1.8.1 and 1.8.2 are the results of the depletion approximation assuming an abrupt space charge edge [41, 42].

The second is a method first published in 2001 by A.F.Yaremchuk and that is called an integral capacitance technique. This method has an advantage because it does not assume constant concentration of the defects; as well it does not assume an abrupt space charge edge.

$$\rho(V) = \frac{1}{q\varepsilon}C_d(V)\int_{-\varphi_b}^{V}C_d(V)dV \qquad (1.8.3),$$

where φ_b is the flat band potential. The coordinate of the profile is calculated according to the Eq. 1.8.2 as in the first method.

1.9. CALCULATION OF THE MOBILITY OF THE MAJORITY CARRIERS

A method of the calculation of mobilities proposed here has generally the same basis as there is described in the paper of J.W. Lee et al [47]. In that paper the structure is modeled simply as a depletion capacitance and the base resistance in series. The resistivity is found using high frequency measurements and this is coupled with the majority carrier densities for finding mobilities.

In the approach proposed here, the method for finding the resistivity is different. The main difference is that here the resistance of the slices of the base with an infinitesimal width is calculated as a coordinate of the structure, whereas in the paper of Lee et al the resistivity is found without an attempt to position these slices

and the resistivity counts for a base region as a whole. Also the resistance of contacts is neglected in their approach.

The estimation of the mobility of majority carriers lies on the well known formula of mobility in case of extrinsic semiconductors

$$\sigma = q \cdot N_p \cdot \mu_p \qquad (1.9.1).$$

Here σ is a conductivity of the base material, q is the elementary charge, N_p is the majority charge carriers concentration and μ_p is the mobility of the majority charge carriers.

For finding values of the mobility, the value of resistivity of the base must be estimated and extracted from the total resistance of the structure. This may be done by analyzing the dc dependence of the resistive circuit element corresponding to the resistance of the base and contacts, and applying the definition of differential resistance for finding the integral resistance of the element:

$$R_i = \frac{1}{I_{dc}} \int_0^{I_{dc}} R_d(I_{dc}) \, dI_{dc} \qquad (1.9.2),$$

where R_i is the integral resistance of the base and contacts, R_d is the differential resistance of the base and contacts, I_{dc} is the direct current.

Because R_i given with Eq. 1.9.2 consists of resistances of contacts and base of the structure, the change in R_i can be used for finding the resistance of the base as the change in resistance reflects the change of the witdh of the base. As a result the Eq. 1.9.2 must be written as

$$\Delta R_i = \frac{1}{I_{dc1}} \int_0^{I_{dc1}} R_d(I_{dc}) dI_{dc} - \frac{1}{I_{dc2}} \int_0^{I_{dc2}} R_d(I_{dc}) \, dI_{dc} \qquad (1.9.2a),$$

The value of ΔR_i is used when together with the Eq. 1.8.2 that has been rearranged to

$$\Delta w = \frac{\varepsilon}{C_d(I_{dc2})} - \frac{\varepsilon}{C_d(I_{dc1})} \qquad (1.8.2a)$$

that gives the change in the width of the base responsible for change of R_i.

As a result the mobility can be calculated from the profile of N_p and ΔR_i either as

$$\mu(V) = \frac{\Delta w_{0,V}}{q \cdot \Delta R_i(I(V)) \cdot S \cdot \dfrac{\displaystyle\int_V^0 N_p(V) \cdot \varepsilon \cdot \frac{S}{C(V)^2} \cdot \frac{d}{dV} C(V) \, dV}{\Delta w_{0,V}}} \qquad (1.9.3)$$

where s is the area of the contact, $\varDelta w_{0,V}$ is the change in the depletion width if the bias is changed from zero to V, or as

$$\mu(V) = \cfrac{L}{q \cdot (\varDelta Ri(I(V)) - \varDelta Ri(I(V - \varDelta V))) \cdot S \cdot \cfrac{\displaystyle\int_V^{V-\varDelta V} Np(V) \cdot \varepsilon \cdot \cfrac{S}{C(V)^2} \cdot \cfrac{d}{dV} C(V)\ dV}{L}} \tag{1.9.4},$$

where L is a suitable length of the material segment (about 20 nm) and $\varDelta V$ is the respective change in bias what can be found as a numerical solution for the equation based on the Eq. 1.8.2a in the form of

$$L(V, \varDelta V) = \varepsilon \cdot S \cdot \left(\frac{1}{C(V - \varDelta V)} - \frac{1}{C(V)} \right) \tag{1.8.2b}.$$

1.10. THE AIM OF THE STUDY

Characterization of electrical properties of semiconducting materials suitable for photoabsorber applications in solar cells relies on implementation of physical models. Such physical models are created and founded on basic concepts of resistivity, inductivity and capacitance among other physical parameters which can be elucidated from different kind of experiments.

For the studies of electrical properties of photoabsorbers, $CuIn_3Se_5$ among them, IS is a promising method that can provide detailed facts about the physical properties of the semiconducting structures.

The main idea of present study is connected with possibility to investigate photoabsorber layers of $CuIn_3Se_5$ prepared by the PLD and HVE techniques with the further purpose to prepare photoabsorber layers and complete solar cells with predictable properties. It should be noted that further development of the IS technique from the point of view of characterization of photoabsorber layers and photovoltaic structures is very important.

A common approach of IS data analysis relies on the circuit analysis using various types of electrical circuit elements [50, 51, 52]. Among these circuit elements are some which physical meaning is unclear although many explanations have been proposed and their use is not highly recommended because of that [51 – 55]. Such is a question about the content and origin of the CPE element and the community is open for possible solutions and analysis of the problem [52].

In this doctoral thesis a major proposition is introduced for analyzing the content of the CPE phenomenon. The general idea of this is represented on the diagram depict on Fig. 1.6.1. and in general form there are proposed parametrical equations by use of what a problem may be possibly analyzed (Appendix A2 in the case of the transformation Fig. 1.6.1b).

A simplified study of the problem with the help of formula available in chapters 1.6 – 1.6.7b is reported in this doctoral thesis together with tests of results obtained.

Analysis of the IS data of the structures based on $CuIn_3Se_5$ photoabsorber showed that simple circuit elements of resistance, capacitance and inductance do not explain experimental findings satisfactory. At the same time the use of CPE elements gave far better results of the modeling, even so that no other elements what were tried by us were able to explain the basic features of the IS curves in question. Because of that the CPE elements were treated as experimental facts and a hypothesis of CPE decomposition into physically meaningful resistances and capacitances is suggested and tested. The main aim of the work is to demonstrate possible validity or invalidity of this method of analysis as well as obtaining basic electrical parameters (majority carriers profile, majority carriers mobility) of the $CuIn_3Se_5$ absorber films with the help of that. In comparison an analysis without CPE elements is used.

2. EXPERIMENTAL

2.1. PLD of $CuIn_3Se_5$

Polycrystalline bulk $CuIn_3Se_5$ samples for the PLD targets were synthesized from 99.999% pure elements in evacuated quartz ampoules in the Department of Chemistry of Saint-Petersburg State University (See Paper I in Appendix A3). Ampoules were inserted in a pipe furnace, heated up to 1100^oC, kept at this temperature for 5 hours and then very slowly cooled down. The synthesized samples were tested using the XRD analysis carried out on DRON-3.0 diffractometer equipped with monochromatic FeK_α source.

The films were deposited by using the PLD technique in the Sankt-Petersburg State University in accordance with the method developed for the $CuInSe_2$ based films. Ablation of the targets was carried out by using XeCl excimer laser. For preventing of decrease of the Se content in the film during the deposition on the heated substrate there was used advanced 3-stages temperature-time regime of deposition: at the first stage the initial $CuIn_3Se_5$ film was deposited at room temperature of substrate, then deposition was stopped and deposited glassy film was heated up to temperature T_1 for crystallization, and finally deposition was continued at relatively lower temperature of substrate T_2. The value of T_2 could be lower than T_1 because in this case vapor condenses on already formed polynanocrystalline $CuIn_3Se_5$ film and therefore nucleation is not limiting stage for crystallization. The appropriate values of T_1 and T_2 were chosen in accordance with results reported in (T_1=320 °C, T_2=160 °C). Both additional annealing processes were performed in vacuum at 400 °C: in situ (immediately after the film deposition, without opening of the vacuum chamber) and after contact with air.

For the XRD measurement the $CuIn_3Se_5$ was PLD deposited onto glass substrates; for investigation of PV properties, the $CuIn_3Se_5$ films were PLD deposited on the glass/ITO substrates. The thicknesses of PLD $CuIn_3Se_5$ photoabsorber layers on glass/ITO substrates were determined by using the SEM technique. The average thickness of the PLD $CuIn_3Se_5$ films was around 300 nm. The cross-section and surface morphology of the PLD $CuIn_3Se_5$ layers were investigated by the SEM technique, using a commercial high-resolution LEO SUPRA 35 microscope equipped with EDS analyzer.

Optical transmission spectra of the films were measured by using spectrophotometer SF-8 (USSR) in the spectral range of 350-2050 nm.

In order to prepare a hybrid structure with rectifying junction the zinc phtalocyanine (ZnPc) was deposited onto the PLD $CuIn_3Se_5$ layer using BOC-EDWARDS AUTO 500 HVE system.

Also, some other materials were used in terms of a junction contact formation with $CuIn_3Se_5$: HVE Ag, Au, Zn, Al and sputtering of i-ZnO/n-ZnO did not give appropriate results in terms of the suitable diode junction for IS measurements.

All electrochemical photovoltaic measurements were performed in standard three-electrode cell in 0.1M H_2SO_4 background solution using AUTOLAB PGSTAT 30 potentiostat/galvanostat. The white light of the halogen lamp with an intensity of 100 mW/cm^2 was used for irradiation. For the I-V and IS measurements AUTOLAB PGSTAT 30 potentiostat/galvanostat was used. Aqueous based graphite suspension (Alfa Aesar) was used for the contacts preparation on the surface of PLD $CuIn_3Se_5$/ZnPc for solid-state I-V and IS measurements.

2.2. CuIn$_3$Se$_5$ DEPOSITED BY HVE

The powder of the stoichiometric polycrystalline precursor of $CuIn_3Se_5$, synthesized from 99.999% pure elements was also evaporated onto glass and glass/ITO substrates using BOC-EDWARDS AUTO 500 HVE system (See Paper III in Appendix A5). For deposition of the film with the thickness around 500 nm, 0.7 g of $CuIn_3Se_5$ polycrystalline substrate was evaporated from the tungsten boat in vacuum of around 10^{-6} mBar onto the glass and glass/ITO substrates fixed onto rotating stainless steel sample-holder heated till the temperature value of 150°C.

As-deposited structures were then annealed on the hot-plate in pure argon atmosphere at 450°C for 1 hour and 500°C for 2 hours (Omni Lab glove box, the oxygen and moisture content is less than 1ppm). All the samples, before and after annealing, were studied by using the HR SEM (Zeiss ULTRA 55 equipped with EDS); XRD spectroscopy (Bruker AXS D5005 difractometer equipped with Cu Kα radiation source (λ=0.154 nm)) and Raman spectroscopy (Horiba's LabRam HR high-resolution spectrometer) for investigation of morphology, identification of phases and stoichiometry.

Electrical properties of the complete glass/ITO/HVE $CuIn_3Se_5$/graphite structures were studied using Autolab PGSTAT 30 potentiostat/galvanostat for obtaining the I-V and C-V characteristics. The conductivity type was determined with the potentio-dynamic thermal probe test. The structure of aged glass/ITO/HVE $CuIn_3Se_5$/graphite was studied also using a Weine-Kerr Precision Impedance Spectrometer with the sampling signal frequency range of 100Hz to 100MHz. For that reason a structure of glass/ITO/HVE $CuIn_3Se_5$/graphite with contacting wires was mold into the solid chip with epoxy glue to obtain stable contacts and to minimize the impedance of the contacting wires.

For the preparation of graphite contacts, adhesive suspension of graphite (Alfa Aesar) was applied. Calibrated xenon lamp was used for the I-V measurements under 100 mW/cm^2 white light conditions.

3. RESULTS AND DISCUSSIONS

3.1. HYBRID STRUCTURE GLASS/ITO/PLD CuIn$_3$Se$_5$/ZnPc
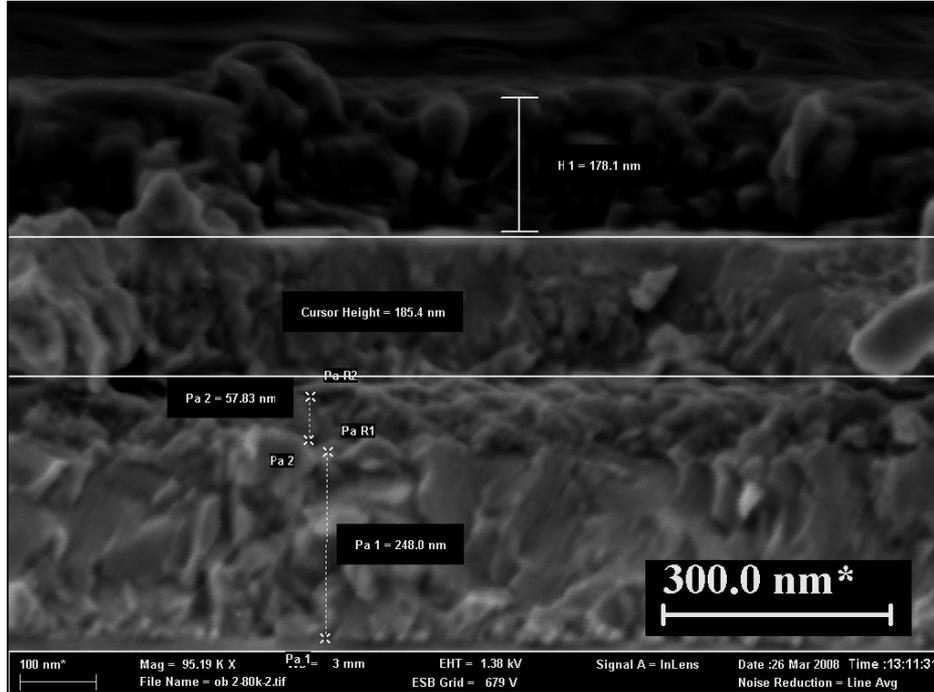
Fig. 3.1.1. SEM micrograph of the glass/ITO/CuIn$_3$Se$_5$/ZnPc

On the Fig. 3.1.1 there is reported the SEM micrograph of the hybrid organic-inorganic structure of glass/ITO/CuIn$_3$Se$_5$/ZnPc. There can be seen four layers. The bottom layer with the thickness around 250 nm is the ITO. Then there are seen two sub-layers of CuIn$_3$Se$_5$ with thicknesses of about 60 nm and 190 nm. These two sub-layers are possibly caused by the temperature program used in the deposition process. In the first step a higher temperature was applied for crystallization and finally the deposition was continued at lower temperature because the crystal growth after the nucleation is initiated, has lower activation energy. The fourth layer is the layer of ZnPc organic semiconductor-photoabsorber of p-type of conductivity with the thickness of about 180 nm. The preparation and investigation of this hybrid structure with organic functional layer is described in Paper II (See Appendix A4).

3.2. IS OF PLD CuIn$_3$Se$_5$

Among many metals deposited by the HVE in our Lab, only Ag contact formed a diode junction with PLD CuIn$_3$Se$_5$ film. Unfortunately this junction was unstable and degraded during *I-V* measurements. On the other hand, a molecular p-type organic ZnPc deposited by HVE method gave a stable reproducible diode junction. This junction did not degrade during *I-V* measurements and that was also appropriate for IS measurements. From the photoconductivity tests in electrochemical cell it was concluded that the PLD CuIn$_3$Se$_5$ is of *n* type (See Paper I in Appendix A3). According to this the junction of p$^+$n is expected to cause the rectifying behavior of the structure (Fig. 3.2.1).
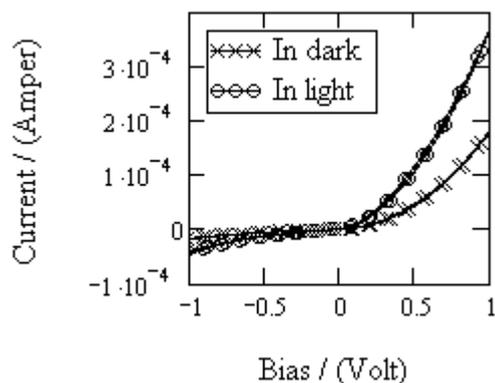
Fig. 3.2.1. *I-V* curves of glass/ITO/PLD-CuIn$_3$Se$_5$/ZnPc in dark and light conditions (the contacting area is 2 mm^2)

The difference of current flowing through the structure at -1 V and 1 V was about factor of ten. In case of the measurements in light this factor was somewhat less (about 8).
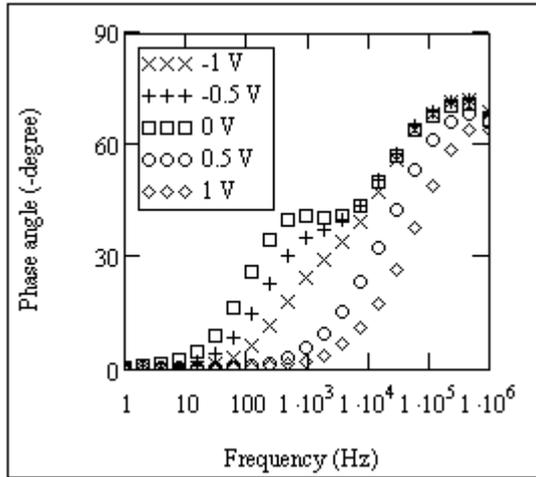
Fig. 3.2.2. Dependence of the impedance phase angle on ac frequency in case of the structure of glass/ITO/PLD-CISe/ZnPc
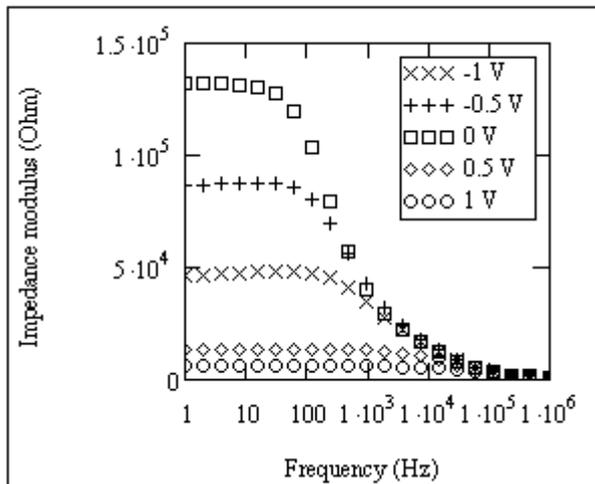
Fig. 3.2.3. Dependence of the impedance modulus on ac frequency in case of the structure of glass/ITO/PLD-CISe/ZnPc

The results of the IS measurements are reported on Fig. 3.2.2 and 3.2.3. The spectra were recorded in the frequency range from 1 Hz to 1 MHz. The shape of the phase angle frequency dependence that has two maxima suggests that a circuit represented on Fig. 3.2.4 applies.
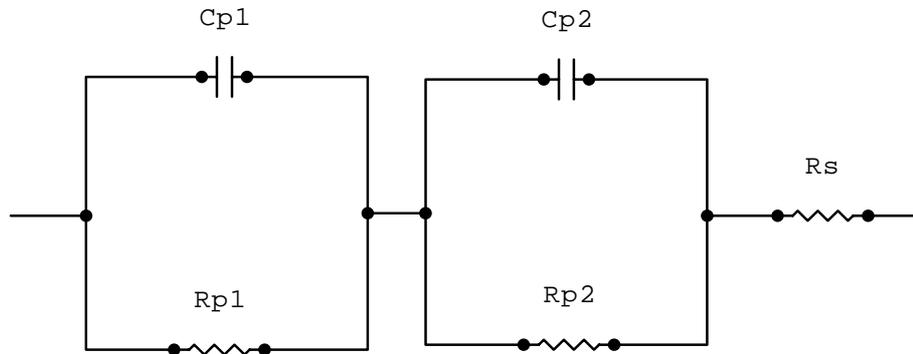
Fig. 3.2.4. The equivalent circuit applied for the analysis of the IS data for glass/ITO/PLD-CISe/ZnPc(C_{p1} and C_{p2} are capacitors while the R_{p1} and R_{p2} are the resistors of the two subcircuits in series connection, R_s is a series resistor)

Two maxima on the phase angle frequency curve are most evident at open circuit voltage conditions. This is an indication that the structure has two time-constants. Another feature of these curves is that at reverse biases and at low frequencies the phase changes sign. This clearly indicates that besides of pure *RC* behavior there is some kind of inductive phenomenon in question. In this case these possible inductive properties are neglected.

From the Fig. 3.2.3 of IS modulus frequency behavior there is seen that the low frequency modulus decreases at forward potentials. The maximum value of the low frequency modulus was observed at -0.2 V. At more reverse biases this value slowly decreases.

An important feature of the low frequency modulus is that at reverse biases the value of modulus decreases a little. These two findings: the change of the sign of the modulus at low frequencies and at reverse biases as well as the decreasing value of the modulus at the same conditions is not common for a pure *RC* circuit.

Still as a first approximation the purely *RC* behaving circuit is used here.

Calculations of the circuit parameters were made on the two frequency basis. Here the impedances measured at two different frequencies were used assuming that the change of the parameters of the circuit elements is negligible. The value of the series resistance was chosen according to the high frequency value of the impedance modulus.
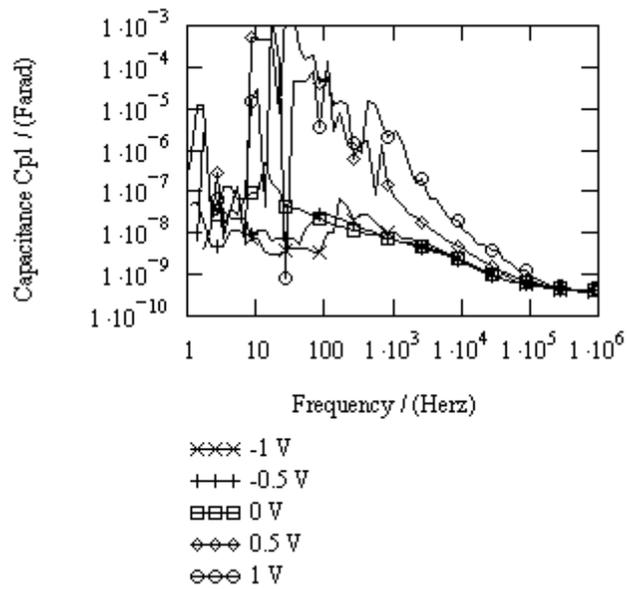
Fig. 3.2.5a. Results of the circuit calculation there impedances of two similar (difference is a half of the decade) frequencies were used for circuit evaluation (C_{PI} vs. frequency)
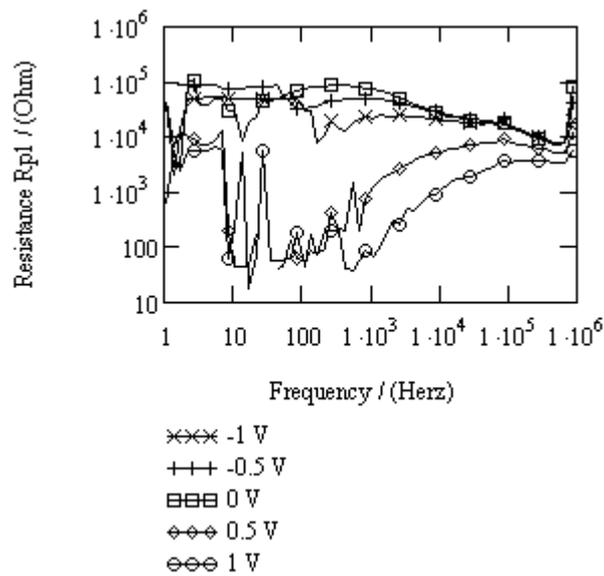
Fig. 3.2.5b. Results of the circuit calculation there impedances of two similar (difference is a half of the decade) frequencies were used for circuit evaluation (R_{PI} vs. frequency)

45
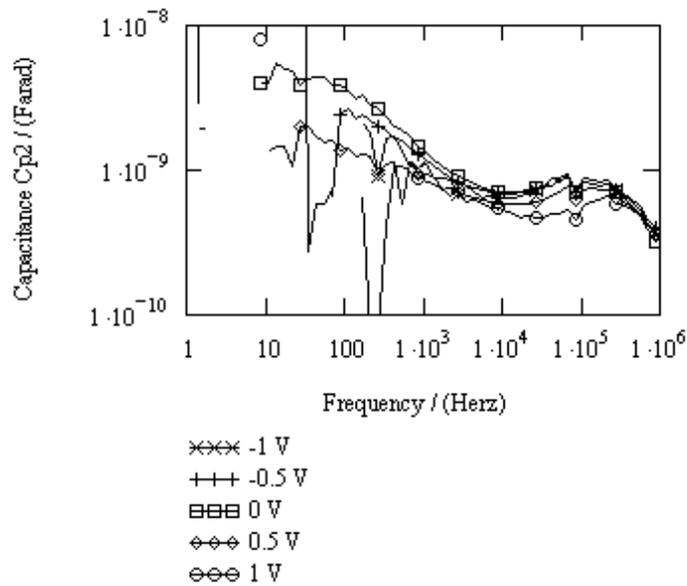
Fig. 3.2.5c. Results of the circuit calculation there impedances of two similar (difference is a half of the decade) frequencies were used for circuit evaluation (C_{P2} vs. frequency)
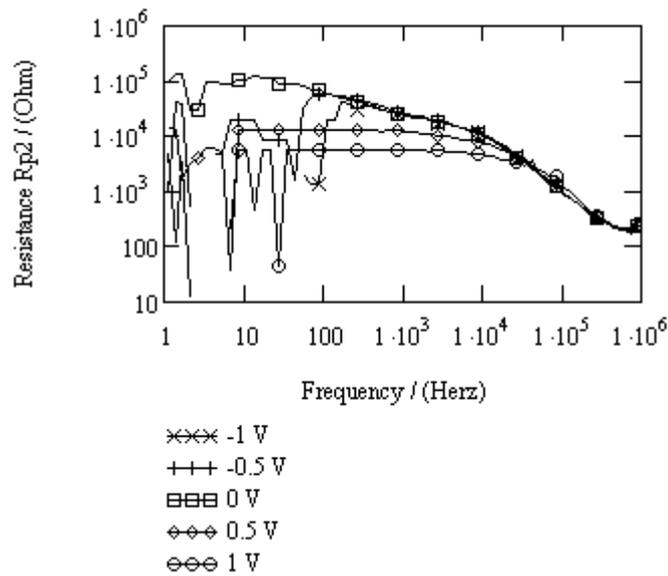
Fig. 3.2.5d. Results of the circuit calculation there impedances of two similar (difference is a half of the decade) frequencies were used for circuit evaluation (R_{P2} vs. frequency)

Results of the circuit calculations using the impedances measured at two similar (difference is a half of the decade) frequencies are reported on the Fig. 3.2.5 a-d.

From these results it becomes evident that two RC blocks in the circuit (Fig. 3.2.4) behave differently. Comparing the results for the C_{PI} and C_{P2} there is more probable that the capacitance of C_{PI} reflects a capacitive behavior of some kind of barrier. At the same time the capacitance of C_{P2} may be considered as a kind of geometrical capacitance because the bias dependence here is not that significant and also the change of capacitance is much weaker.

A common property of all these four results is that at low frequencies the dependencies lose the continuity and a significant noise in results makes the analysis at low frequencies almost impossible.

At the same time it is important to note that the bias distribution can be calculated properly only if the low frequency values of the resistances are available. Here it must be concluded that they are not available at frequencies less than about 1 kHz if the worst curve is taken into account (Fig. 3.2.5b 0.5 V). To overcome this it is clear that if higher frequencies are used, the bias distribution can be calculated approximately.
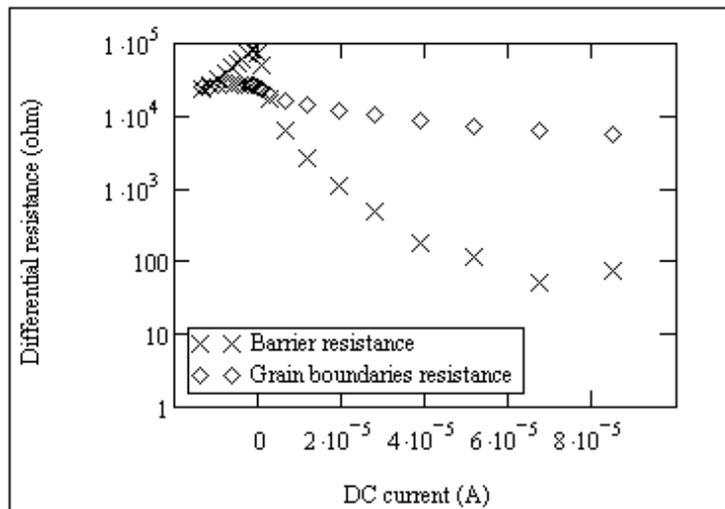
Fig. 3.2.6. A dependency of parallel resistances of R_{PI} and R_{P2} on dc current if the frequency is 1 kHz

On the Fig. 3.2.6 there is reported how parallel differential resistances depend on dc current. As it was impossible to obtain continuous results at lower frequencies of the measurement, the 1 kHz frequency must be treated as a kind of

47

trade-off between low frequency and high frequency. This means that the integration according to the definition of

$$V_i = \int_0^{I_{dc}} R_p(I_{dc})\, dI_{dc} \qquad (3.2.1),$$

where V_i is a bias for V_1 or V_2, can give only approximate results for the bias distribution, because the frequency used for $R_p(Idc)$ is not small (approaching zero).
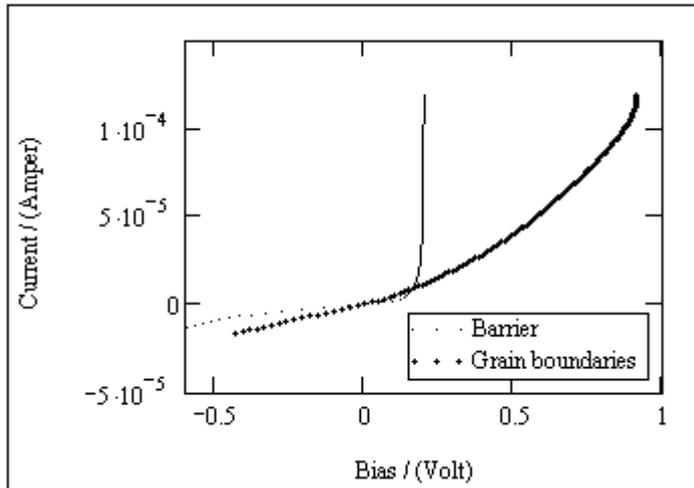
Fig. 3.2.7. A bias distribution calculated according to the Eq. 3.2.1 distinguishing two separate regions in the structure of glass/ITO/PLD-CuIn$_3$Se$_5$/ZnPc

On the Fig. 3.2.7 there are represented results for the bias distribution calculations according to the Eq. 3.2.1. From these results it must be concluded that one of the *RC* blocks describing the structure of glass/ITO/PLD-CuIn$_3$Se$_5$/ZnPc is a possibly an energetic barrier caused by a junction. Another block may be attributed to the bulk that is not linear in the *I-V* response. This nonlinearity may arise because of grain boundaries in this bulk or maybe there is also a weak barrier that is connected in series in the same direction as the main barrier is.

The result for the barrier-like *I-V* curve is used for constructing the *C-V* curve there C_{P1} values are used as the capacitance of the barrier.
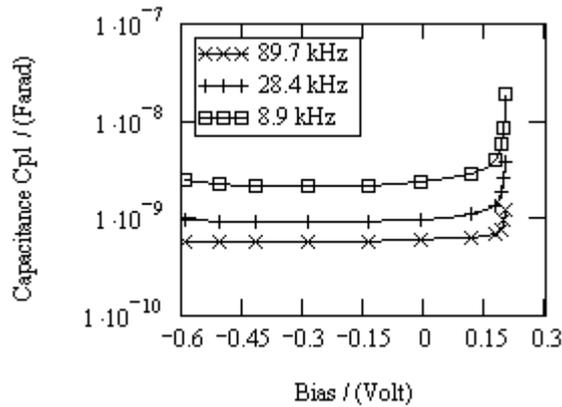
Fig. 3.2.8. *C-V* **curves constructed according to the bias distribution calculations of Eq. 3.2.1**

C-V curves constructed using Eq. 3.2.1 for voltage and C_{PI} values of the *RC* circuit are reported on Fig. 3.2.8. The rapid increase of capacitance at forward biases around 0.2 V is probably caused by depletion behavior of the junction. This can be concluded from Fig. 3.2.5a because there it is seen that at high frequencies (500 kHz and higher) there is no substantial increase in capacitance value. A remarkable increase there would declare that a chemical capacitance and the injection of minority carriers take place.
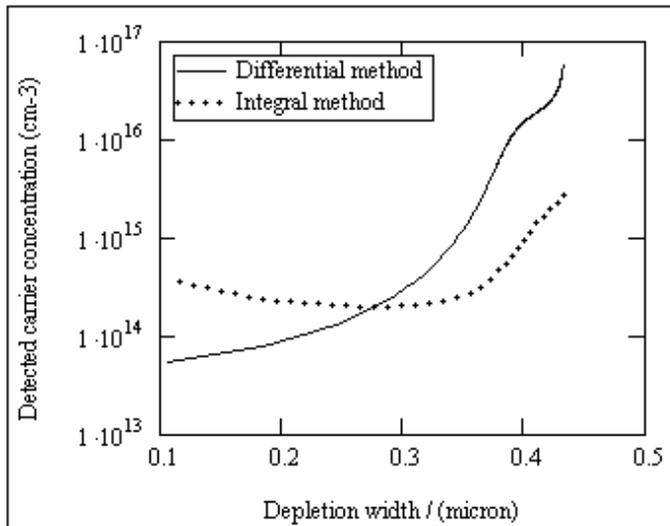
Fig. 3.2.9. Concentration profiles of the shallow level defects in the structure of glass/ITO/PLD-CuIn$_3$Se$_5$/ZnPc calculated using two different methods

49

On the Fig. 3.2.9 there are reported results of the shallow level defect densities obtained at two different calculation methods. The usual method, based on Eq. 1.8.1, gives a profile that manifests a concentration change nearly about three orders of magnitude. At the same time the integral method, based on Eq. 1.8.3, provides a result with values in the range about one order of magnitude.

Here the results were obtained then the *C-V* curves were fit with rational fractions containing a hyperbolic term as a factor. These fitting results give somewhat more even fitting curves than the spline functions (inbuilt fitting functions of different types of Mathcad software) would give. This is the reason why the profile obtained with the differential method has no sharp peaks that is an ordinary observation in such calculations in case of using the Eq. 1.8.1. As a comparison with the differential method such peaks would not appear in case of integral method because it does not contain a corresponding critical term that would create such.

Finally there must be concluded that the shallow defects concentration is in the range of $2 \cdot 10^{14}$ to $2 \cdot 10^{15}$ cm^{-3}.

3.3. SEM, XRD, EDS, RAMAN AND *I-V* INVESTIGATIONS OF HVE CuIn$_3$Se$_5$
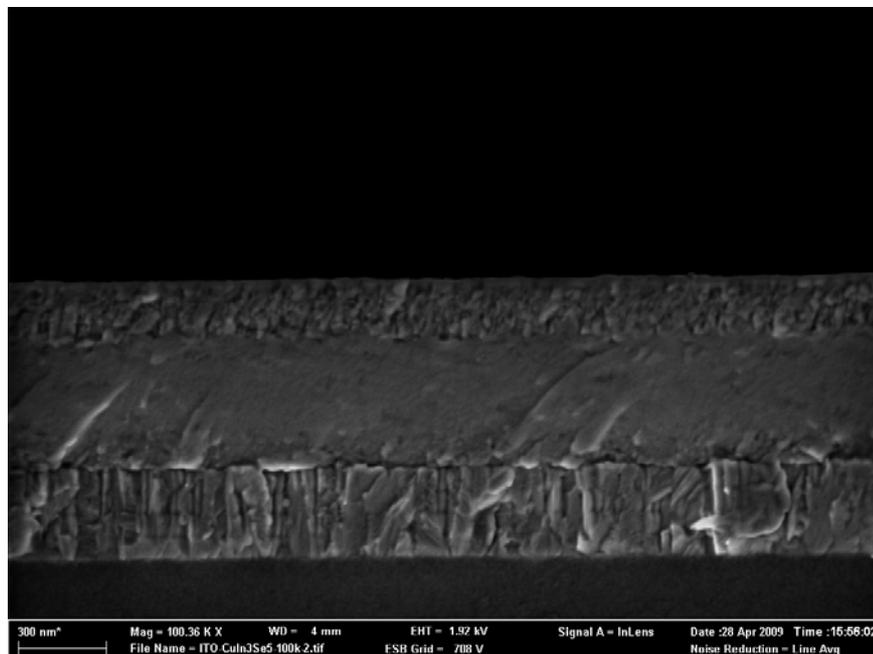
Fig. 3.3.1. Cross-sectional SEM micrograph of glass/ ITO/ HVE CuIn$_3$Se$_5$ as-deposited
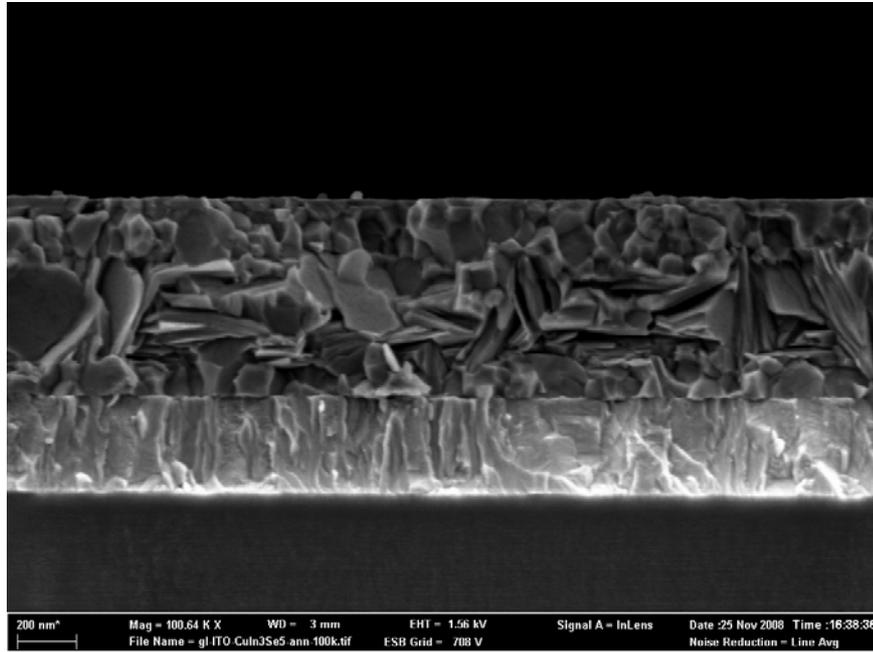
Fig. 3.3.2. SEM micrograph of the ITO/ HVE CuIn$_3$Se$_5$ annealed at 450°C for 1 hour in argon athmosphere
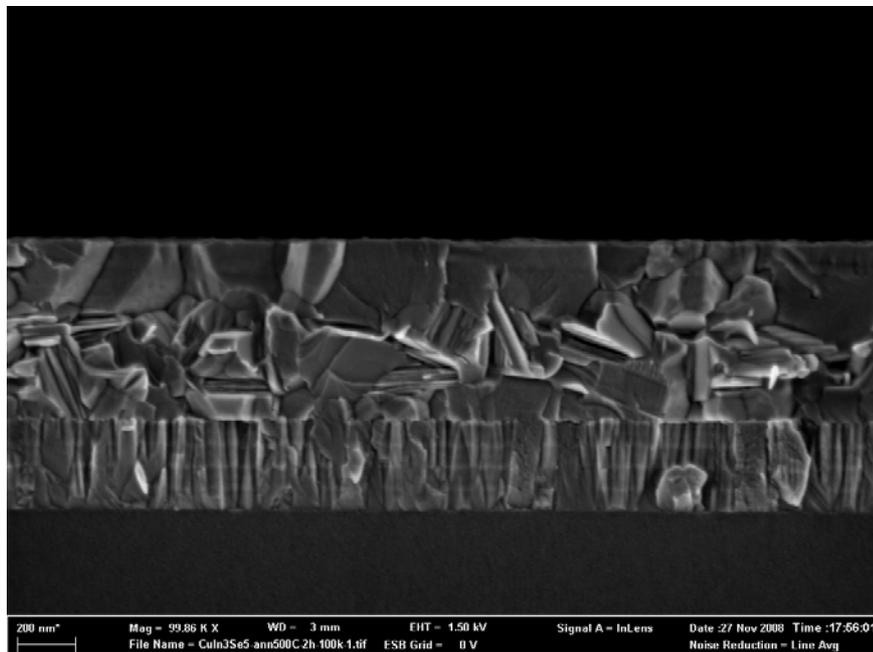
Fig. 3.3.3. SEM micrograph of the ITO/ HVE CuIn$_3$Se$_5$ annealed at 500°C for 2 hour in argon athmosphere

The SEM micrographs of as-deposited and annealed structures of the ITO/ HVE $CuIn_3Se_5$ are represented in the Fig. 3.3.1-3.3.3. It should be noted that the composition of as-deposited films is not uniform in cross-section (Fig. 3.3.1). From the micrograph there is seen that two layers with different morphology are present. According to the electron dispersive spectroscopy (EDS) data, the first layer after ITO corresponds to $CuIn_4Se_5$ composition. The second layer has approximately a composition of $Cu_2In_3Se_5$. In overall composition both layers correspond to the $CuIn_3Se_5$ i.e. to the stoichiometry of the source polycrystal.

After annealing at 450°C during 1 hour in argon atmosphere, the morphology of structures was changed dramatically – the structures demonstrate practically uniform composition of $CuIn_3Se_5$ layers (Fig. 3.3.2). Although there can be distinguished layers of crystals with slightly different morphology, their composition is very similar to each other. Apparently thermal diffusion has averaged the initially different composition of layers and induced crystal growth.

In addition, annealing at 500°C for 2 hour in argon atmosphere (Fig. 3.3.3) gives the further increases of the size of $CuIn_3Se_5$ crystals and improves the morphology of the photoabsorber layer from the point of view the homogeneity of $CuIn_3Se_5$ crystals. The XRD spectrum of the as-deposited glass/$CuIn_3Se_5$ structure shows that even as-deposited film includes already the chalcopyrite structure (with dominating in (112) plane) (Fig. 3.3.4).
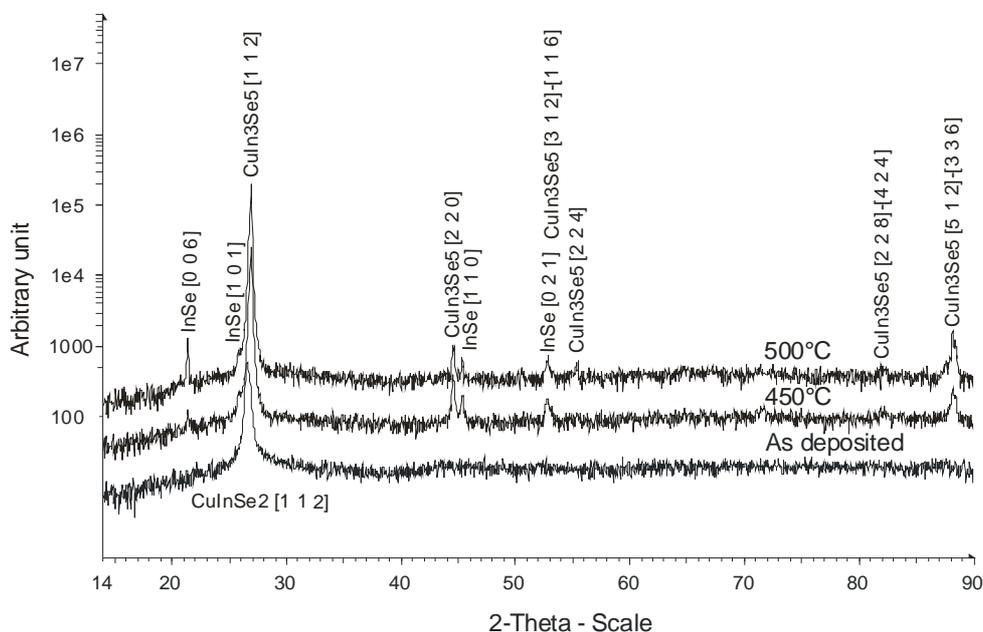
Fig. 3.3.4. XRD spectra of glass/ HVE $CuIn_3Se_5$ structures

52

The XRD spectrum of the as-deposited glass/HVE $CuIn_3Se_5$ structure shows that even an as-deposited film includes highly-oriented chalcopyrite structure (absolute dominating in (112) plane) (Fig. 3.3.4).

For highlighting of the other peaks in the XRD spectrum, the values of intensity are plotted on a logarithmic scale. As the result of the annealing process the dominating phase of $CuIn_3Se_5$ chalcopyrite structure is observed. The spectrum of a structure annealed at 450°C for 1 hour shows almost at the same 2θ value a strong peak that corresponds to the reflection from the plane (112) of $CuIn_3Se_5$. Other peaks can be distinguished corresponding to $CuIn_3Se_5$ chalcopyrite phase. According to the database of ICDD PDF-4+2008 these peaks correspond to the planes of (220), (312), (116), (224), (228), (424), (512), (336). Also weak peaks corresponding to traces of the InSe phase are present. These peaks correspond to the reflections from planes of (006), (101), (110) and (021). In the spectrum of the structure annealed at 500°C for 2 hour the chalcopyrite peaks are stronger, proving that the phase composition has become more crystalline and the crystals of the detected phases are grown bigger.
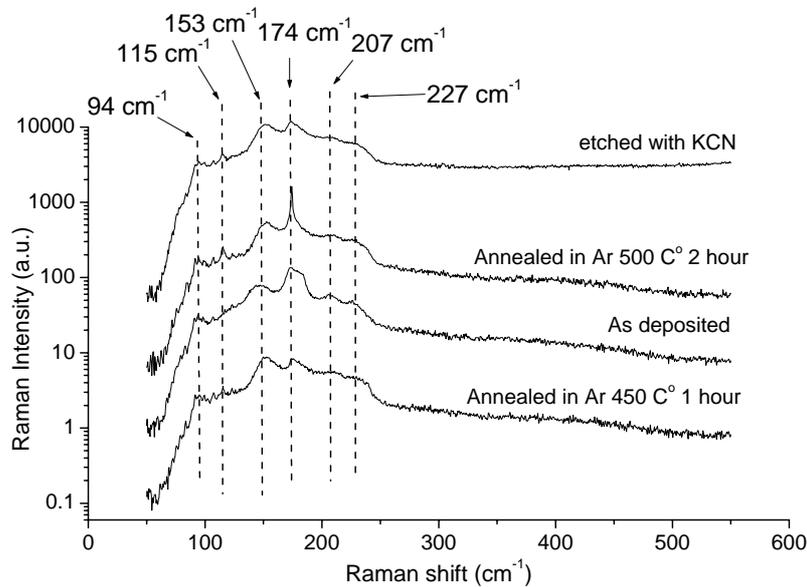
Fig. 3.3.5. Raman spectra of glass/ HVE $CuIn_3Se_5$ structures

The Raman spectra (Fig. 3.3.5) show that different phases are present on the surface of the structure. The main peaks of A1 mode at 153 cm^{-1} and 174 cm^{-1} correspond to the phase of $CuIn_3Se_5$ [58, 59]. Weak peak at 94 cm^{-1} is caused by the CuSe traces. Weak peaks at 115 cm^{-1} and 227 cm^{-1} correspond to InSe traces [60]. It should be noted that the etching of annealed $CuIn_3Se_5$ film in 5% KCN solution during 1 min. decreases an intensity of 94 cm^{-1} peak and therefore confirms the reducing of presence of CuSe phase at the surface of photoabsorber film.

Annealed glass/ITO/$CuIn_3Se_5$ semi-structures were used to prepare complete diode-like structures for the impedance measurements. *I-V* curves for the structures with graphite adhesive contacts are represented in the Fig. 3.3.6.
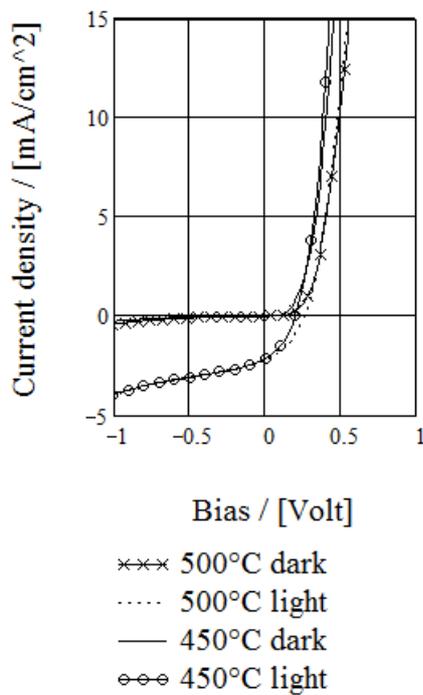
Fig. 3.3.6. *I-V* curves of the glass/ITO/HVE CuIn₃Se₅/graphite structures annealed at 450 and 500 °C

Both structures had a stable diode–like shape of *I-V* curves in the range of applied potential +/-2 V. The structure annealed at 500°C for 2 hour had higher open circuit voltage (V_{oc}) value (270 mV under 100 mW/cm^2 white light irradiation). *C-V* measurements of these structures revealed that the built in voltage for these two different structures is nearly the same with the difference of about 10 mV. These diode-like structures were prepared also with silver adhesive contact but the *I-V* curves in this case did not exhibit photo voltage generation. It should be

54

noted that prepared structures are not considered as complete solar cells but only as the structures appropriate for the characterization of deposited $CuIn_3Se_5$ photo absorber layers by using the impedance technique.
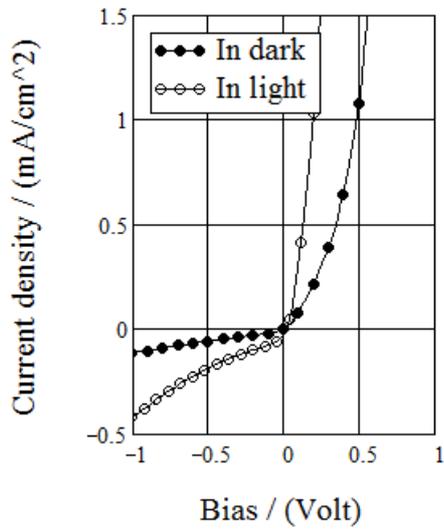
Fig. 3.3.7. *I-V* curves of the aged glass/ITO/HVE $CuIn_3Se_5$/graphite structures annealed at 450°C

After keeping of the structures in air for several months, *I-V* curves showed that the useful properties of these have remarkably deteriorated. On the Fig. 3.3.7 there are presented *I-V* curves of the glass/ITO/HVE $CuIn_3Se_5$/graphite structure annealed at 450°C what has been aged.

V_{oc} together with the I_{sc} of the structure is almost vanished if compared with the freshly prepared structures (Fig. 3.3.6).

3.4. IS OF THE FRESHLY HVE DEPOSITED CuIn$_3$Se$_5$

The results of the measurements of the impedance of the freshly HVE deposited structures are represented on Fig. 3.4.1 and Fig. 3.4.2.
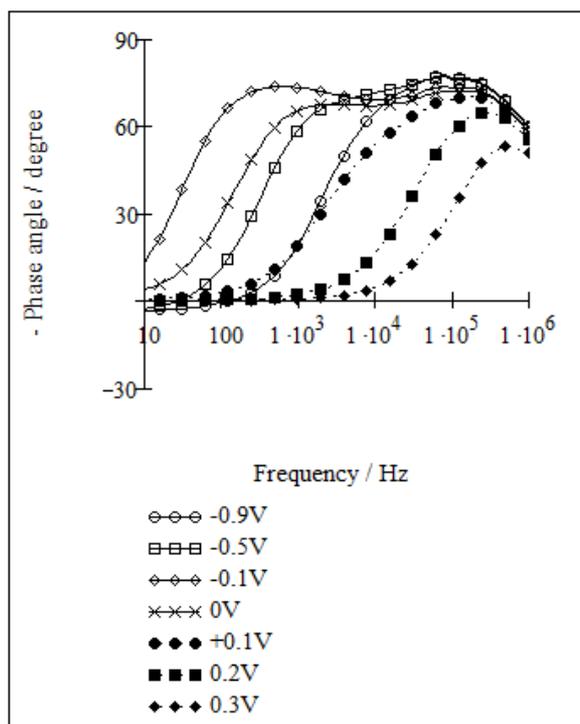
Fig. 3.4.1. Modulus of the impedance vs. frequency dependencies of the glass/ITO/CuIn$_3$Se$_5$ structures annealed at 450°C for 1 hour with following deposition of the graphite dot-contacts, measured at different applied potentials (reverse biases marked with transparent margins, forward with filled)
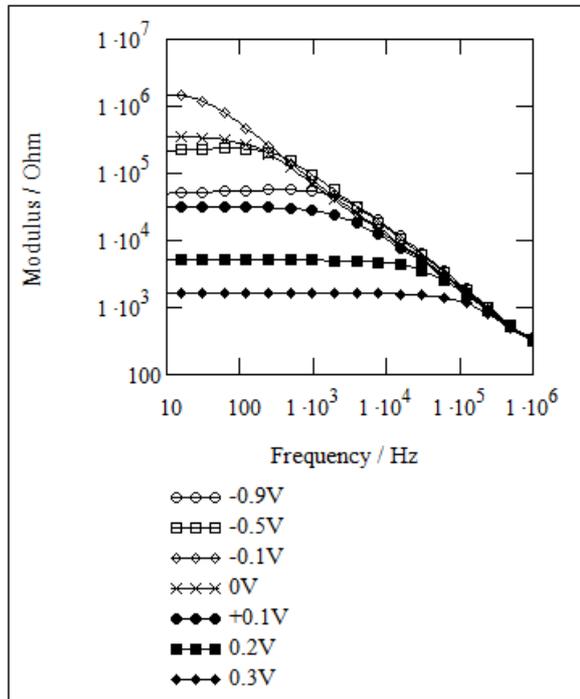
Fig. 3.4.2. The phase of the impedance vs. frequency dependencies of the glass/ITO/CuIn$_3$Se$_5$ structures annealed at 450°C for 1 hour with following deposition of the graphite dot-contacts, measured at different applied potentials (reverse biases marked with transparent margins, forward with filled)

On the Fig. 3.4.1 there is seen that the highest low frequency resistance is measured at -0.1 V. This maximum value decreases rapidly if the forward bias is applied. This is a usual behavior of the junction barrier if the forward potential is applied and the width of the depletion region is decreasing. On the other hand, the decrease of the low frequency resistance in the case of reverse bias is much less. This decrease indicates the existence of a shunt resistance in the barrier. A single plateau of modulus at low frequency indicates that there is one main barrier in the structure. This barrier acts mainly as a (resistance and capacitance) *RC* parallel network. The deviation from the pure *RC* behavior manifests themselves at reverse biases. There can be observed, as a minor effect, that at low frequencies, the modulus slowly decreases if the frequency decreases.

The phase of the impedance vs. frequency plot (Fig. 3.4.2) reveals that there are two maxima in these curves. The maximum appearing at lower frequencies is most pronounced at -0.1 V. At forward potentials this maximum vanishes entirely. This may point that there are two barriers in series and in the same bias direction in the

57

structure. A minor effect is there that at reverse potentials and at low frequencies the sign of the phase changes. This is probably a real effect and is not caused by any problem of the wiring. This was concluded after using special calibration procedures with reference measurements that are necessary for ruling out wiring effects what may affect the results of the measurement. Also the influence of some outer field is not probable because these measurements were conducted inside the grounded Faraday cage as well outside without any change in results.

The modeling of the results of the impedance measurements was made by using the circuit depicted on the Fig. 3.4.3 which turned out to be the best circuit for this task. This circuit was able to model impedance spectra in the frequency range of 10 Hz to 1 MHz at different applied biases in the range of ±1 V. The modeling error was calculated at every experimental frequency as a comparison of the experimental value and the result of the modeling. The maximum error was less than 3%.

As a modeling tool, a self-made fitting program in Labview software was used. The algorithm used for fitting was a Monte Carlo method. The objective function of this particular fitting procedure was the minimization of the cumulative deviation error percentage between the modeling result and the experimental data.
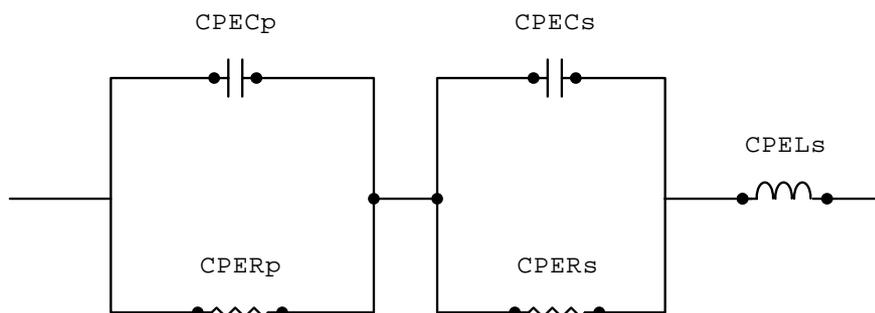
Fig. 3.4.3. Equivalent circuit found to describe the impedance behavior of the glass/ITO/CISe/graphite structure. CPE notation in names of circuit elements of CPECp, CPERp, CPECs, CPERs and CPELs points to the circumstance that these elements are CPE elements resembling either capacitors, resistors or inductors

First, the equivalent circuit principally similar to the circuit reported here on Fig. 3.4.3 was used. Here all elements were chosen as resistors, capacitors and inductors. The modeling result was poor with about 10% of mean error. Then these resistors, capacitors and inductors were replaced by constant phase elements (CPE) (Eq. 1.6.1).

We use modeling with CPE-s here for a qualitative interpretation of the impedance data. No quantitative physical models are applied here because CPE-s only with n values of 1, 0 and -1 can provide useful dimensions for physical modeling and only then the parameter of Q can be used without any further considerations and interpretation. We must simply state that CPE behavior found here was an experimental fact that was the best option for a formal mathematical description of our system.

The results obtained are reported on Figs. 3.4.4-3.4.6. If n of the CPE is close to 1, it is referred here as a capacitor-like CPE (CPE-C). Similarly, if the n of the CPE is close to 0, it is referred here as a resistor-like CPE (CPE-R). If n of the CPE is close to -1 or -0.5, it is referred here as an inductor-like CPE (CPE-L).
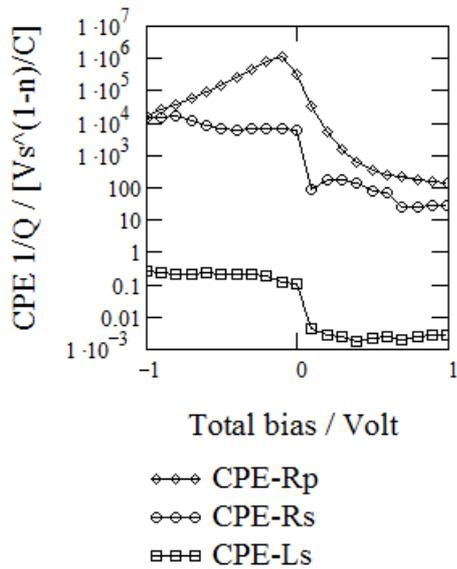
Fig. 3.4.4. Dependence of the 1/Q of the CPE-Rp and CPE-Rs vs. total bias applied on structure of glass/ITO/CuIn$_3$Se$_5$ annealed at 450°C for 1 hour with following deposition of the graphite dot-contacts (1/Q is the parameter of CPE element with the dimension of V·s$^{(1-n)}$/C)

On Fig. 3.4.4 there are reported the results for the values of 1/Q of CPE-Rp and CPE-Rs. There must be noted that the bias dependence refers to the total bias and not to the partial bias applied to the element under discussion. The true distribution of the bias between the three blocks of the circuit (Fig. 3.4.3), namely CPE-Rp parallel CPE-Cp, CPE-Rs parallel CPE-Cs and CPE-Ls there is not known. Also there must be stressed that the dimension of these values are every time different and do not have a dimension of Ohm (V·s/C).
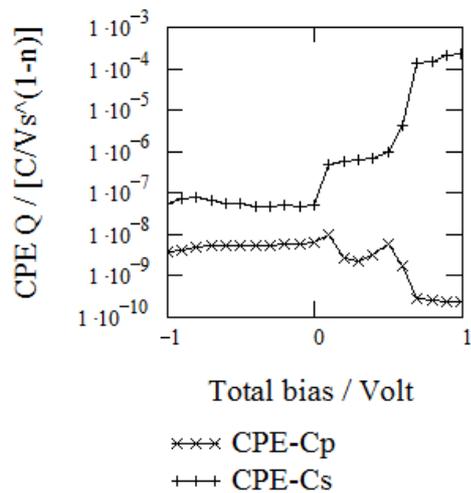
Fig. 3.4.5. Dependence of the Q of the CPE-Cp and CPE-Cs on total bias applied on structure of glass/ITO/CuIn$_3$Se$_5$ annealed at 450°C for 1 hour with following deposition of the graphite dot-contacts

General comments for the Fig. 3.4.5 are similar as those to the Fig. 3.4.4 earlier.
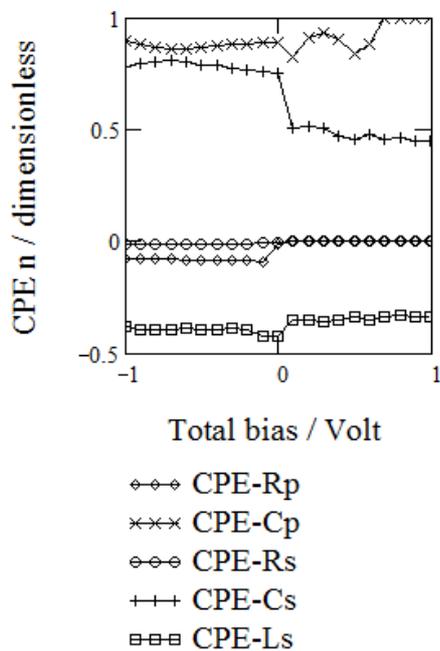
Fig. 3.4.6. Dependence of the n of the CPE-s on total bias applied on structure of glass/ITO/CuIn$_3$Se$_5$ structures annealed at 450°C for 1 hour with following deposition of the graphite dot-contacts

60

For the reference of the dimensions of values reported on Fig. 3.4.4 and Fig. 3.4.5, the Fig. 3.4.6 gives an account how does the exponential parameter n of CPE change with total bias applied to the structure.

The conceptual situation reported on Fig. 3.4.4 and Fig. 3.4.5, is very special and simple conclusions about the shape of the curves are therefore highly speculative.

The soundest conclusions can be made of the CPE-Rp and CPE-Rs at bias values higher than zero volts. From the Fig. 3.4.6, there is seen that n values corresponding to the CPE-Rp and CPE-Rs at these potentials, are *effectively* zero ($n \approx 4 \cdot 10^{-3}$). This means that Q values of that CPE-s have *effectively* the dimension of Siemens.

Based on this, there can be concluded, that the behavior of the $1/Q$ value of the CPE-Rp describes the situation then an energetic barrier is forwardly biased and the resistance of this barrier is quickly decreasing. The conclusion made on the basis of the behavior of the $1/Q$ value of the CPE-Rs is more speculative. This may be the evidence that a minority charge carriers injection into the base area of the structure takes place and the resistivity is decreasing there because of an increase of free charge carriers' concentration.

The behavior of the capacitance like CPE-s is reported on Fig. 3.4.5. From the Fig. 3.4.6 there is reported that at forward biases the value of n of the CPE-Cs is almost 0.5. This means that the Q value of CPE-Cs has *effectively* a dimension of Warburg semi-infinite linear diffusion resistance [50]. The increase of these values is about three orders of magnitude. Such profound increase is usually characteristic to the minority carriers accumulation process there a diffusion capacitance or a chemical capacitance appears in the base of the structure [61]. Again this must be stressed, that this value does not have a dimension of capacitance. On the other hand the value of the Q of the CPE-Cp decreases at forward potentials. If the part of the circuit consisting of CPE-Rp parallel CPE-Cp is a manifestation of the depletion layer, this decrease may be another indication of the minority carriers' accumulation also in the barrier region of the structure [62].

The analysis of the reverse side of the bias is even more unclear because only the value of n of the CPE-Rs can be considered effectively zero ($n \approx -1 \cdot 10^{-2}$). The value of Q of CPE-Rs increases at most reverse biases. The magnitude of this value is also in the range of $1 \cdot 10^{4}$, that is not a usual value for base resistance in such structures (usually about 100 Ohm). This may be interpreted as weak barrier behavior at the contact between graphite and $CuIn_3Se_5$ layers. This must be remembered that the bias attributed to the CPE-Rs element is not the true bias, but the total bias applied to the entire structure. This means that the shape of this and also other curves is distorted in respect of the bias axis. In case of CPE-Cs and CPE-Rs this is expected to be the most prominent. The behavior of CPE-Rp and

CPE-Cp at reverse biases is possibly a manifestation of the depletion layer. The decrease of the $1/Q$ value of the CPE-Rp at reverse biases is possibly due to the decreasing shunt-resistance of the barrier. CPE-Cs values at reverse biases possibly reflect the geometrical capacitance of the base region because the Q values of CPE-Cs are greater than Q values of CPE-Cp by one order of magnitude.

The interpretation of the behavior of the CPE-Ls is the most speculative task. We only give a comment here that the influence of this element in the circuit (Fig. 3.4.3) on the impedance phase is remarkable only at frequencies higher than 200 kHz. This was concluded from the influence analysis of the circuit elements (not reported here).

An interesting observation is that the values of n of CPE-Rp and CPE-Rs change the sign at zero applied voltage. At all reverse biases the values of n are negative, at forward potentials n becomes positive. As the direction of the externally applied electrical field changes there the direction, this may be the cause.

Capacitance data, when the impedance is represented as a parallel capacitance and parallel resistance, is reported on Fig. 3.4.7. The contact area of the structure is 2 mm^2. High frequency values of the real part of the impedance were used as estimation for the serial resistance in these calculations.
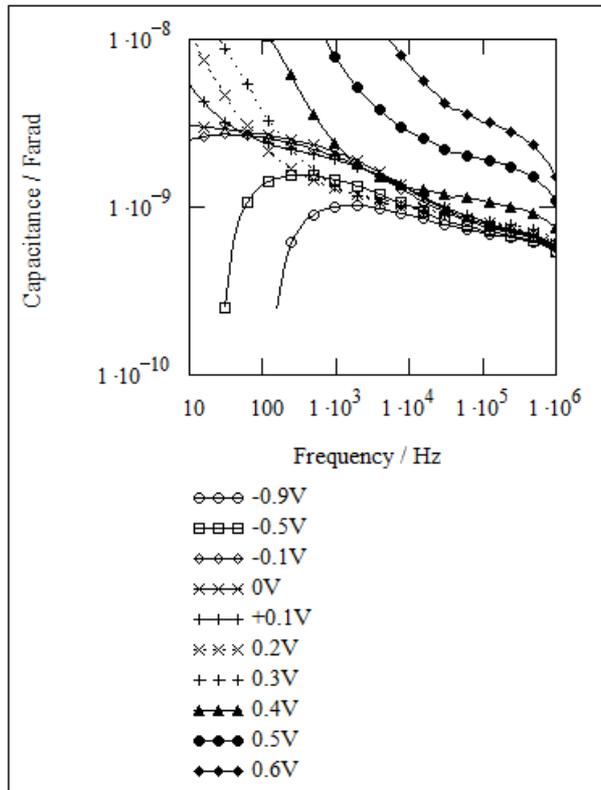
Fig. 3.4.7. Parallel differential capacitance vs. frequency dependencies of the glass/ITO/CuIn₃Se₅/graphite structures annealed at 450°C for 1 hour, measured at different applied potentials (reverse biases marked with transparent margins, forward with crosses and filled margins)

The capacitance decay with increasing frequency is characteristic to the broad distribution of deep levels possibly in midgap [63]. An exception to this behavior here are seen at most high reverse biases. Here at low frequencies (less than about 1 kHz), the capacitance changes the sign. This is possibly due to inductive properties of the structure as pointed out before. This phenomenon is also reflected in the negative value of the n of the CPE-Rp and CPE-Rs at reverse potentials (see Fig. 3.4.6). At forward potentials and already at high frequencies the capacitance starts to increase very rapidly. This is a characteristic behavior of the diffusion capacitance. This phenomenon was also found in the results of the modeling of the impedance (see Fig. 3.4.5).

The estimation of the barrier height and the shallow level defect concentration was made by linearization of the Mott-Schottky curves according to the formula of the simple depletion capacitance formula of the Schottky barrier [64]

63

$$C = \left| \frac{\partial Q_{sc}}{\partial V} \right| = A \sqrt{\frac{q \varepsilon_0 \varepsilon_s N_A}{2(V_{bi} - V)}} \qquad (3.4.1).$$

Here A is the contact area, Q_{sc} is the charge of the space charge of the depletion layer, V is the voltage drop in depletion layer, q is an elementary charge, ε_0 is the dielectric constant of the vacuum, ε_s is the dielectric constant of the material (ε_s=13.6 was used [65]), N_A is the acceptor density and V_{bi} is the built-in potential.
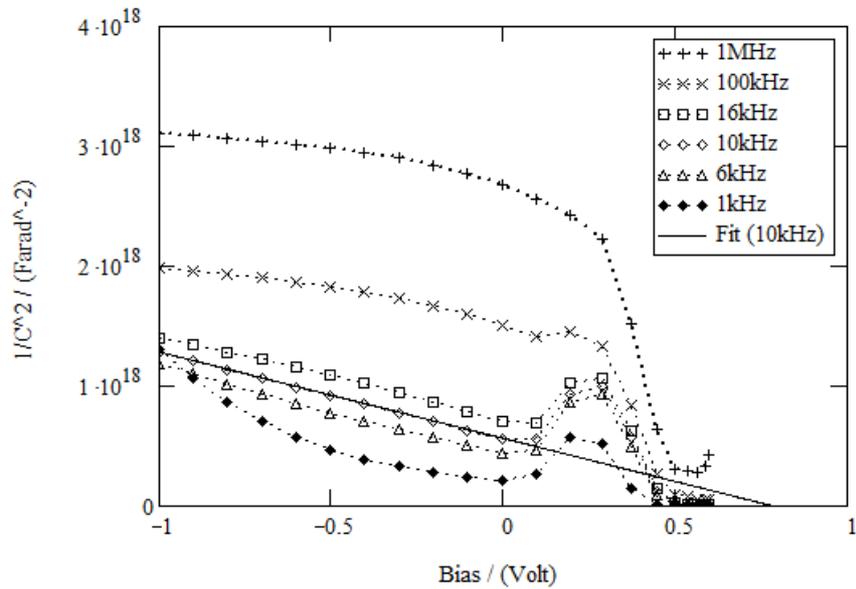
Fig. 3.4.8. *Mott-Schottky* curves of the glass/ITO/CuIn$_3$Se$_5$ annealed at 450°C for 1 hour

From the Fig. 3.4.8 this is evident that estimated values of barrier height and the concentration is dependent on the measurement frequency. Most obviously there is a linear region at reverse potentials around 10 kHz frequency. An estimation (solid line on Fig. 3.4.8) of the built-in potential there gives a value of 780 mV. The estimation for the shallow defects concentration gives a value of $3.6 \cdot 10^{16}$ cm^{-3}. An estimation of built-in potential at 6 kHz and 16 kHz gives values of 600 mV and 1 V respectively. It is expected that at high frequencies the deep lewel freez-out occures and higher frequencies than 10 kHz would be more appropriate for the estimation of the concentration. On the other hand the frequency of 10 kHz turns out to be most suitable for applying the Mott-Schottky linearization as reported on Fig. 3.4.8.

As the Mott-Schottky plots are not linear at higher frequencies, the carrier concentration profiles are calculated according to the well known Eq. 1.8.1 of the abrupt edge approximation [41].

The depletion width is calculated according to the Eq. 1.8.2. The calculations of the shallow level defect concentrations profiles (Fig. 3.4.9) were made at same measurement frequencies as reported on the Mott-Schottky plot (Fig. 3.4.8).
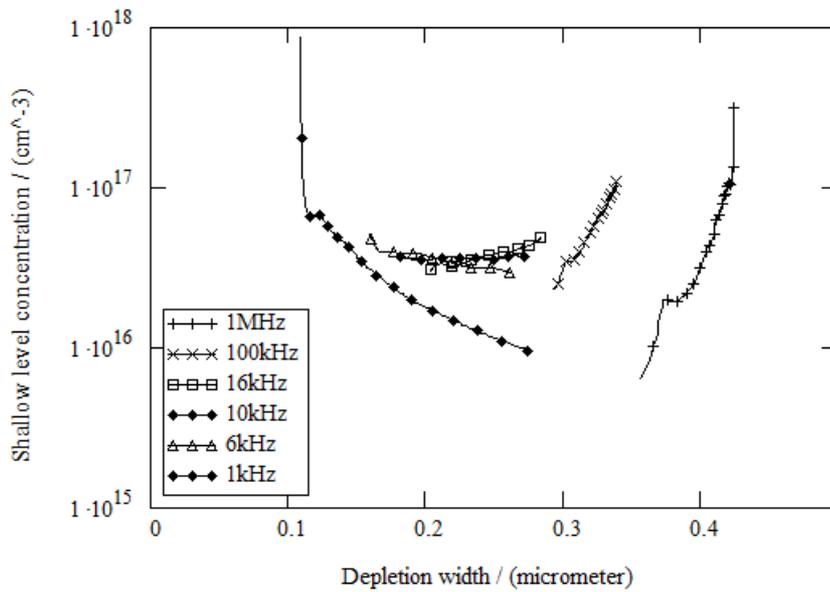
Fig. 3.4.9. Free charge carriers profiles for the glass/ITO/CuIn$_3$Se$_5$ annealed at 450°C for 1 hour, calculated at different measurement frequencies

Results show that measurements at different frequencies affect the coordinate calculations in great extent. This means that these profiles can be used only for estimating a kind of mean concentration. Integration of these curves over the coordinate reveals somewhat surprising fact that the mean concentration increases monotonously as the measurement frequency increases (Fig. 3.4.10). So the average concentration calculated at 1 kHz is $2.8 \cdot 10^{16}$ cm^{-3} whereas the concentration calculated at 1 MHz is $6.0 \cdot 10^{16}$ cm^{-3}.
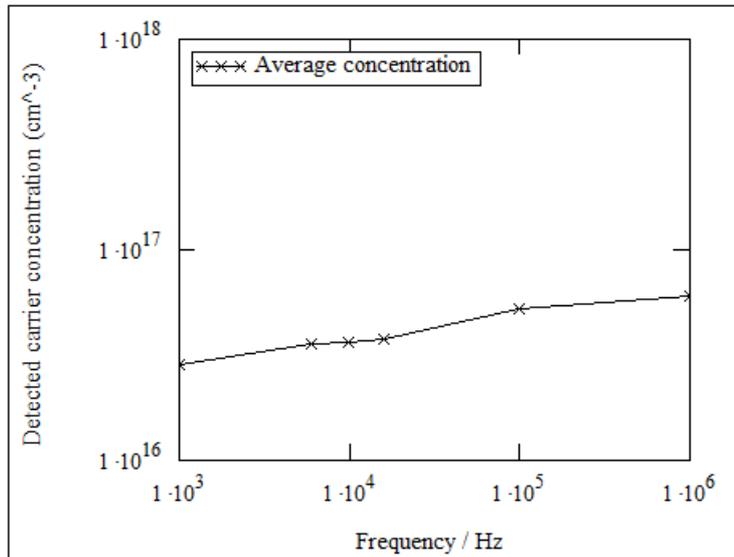
Fig. 3.4.10. Free charge carriers averaged concentrations for the glass/ITO/CuIn$_3$Se$_5$ annealed at 450°C for 1 hour, calculated at different measurement frequencies

3.5. IS OF THE AGED HVE CuIn$_3$Se$_5$

3.5.1. RESULTS OF THE IS MEASUREMENTS

I-V curves of such structure, what show up major deteriorations in electrical properties essential for solar cells are presented in Fig. 3.3.7. Structures of the aged glass/ITO/CISe/graphite were also studied with the IS.
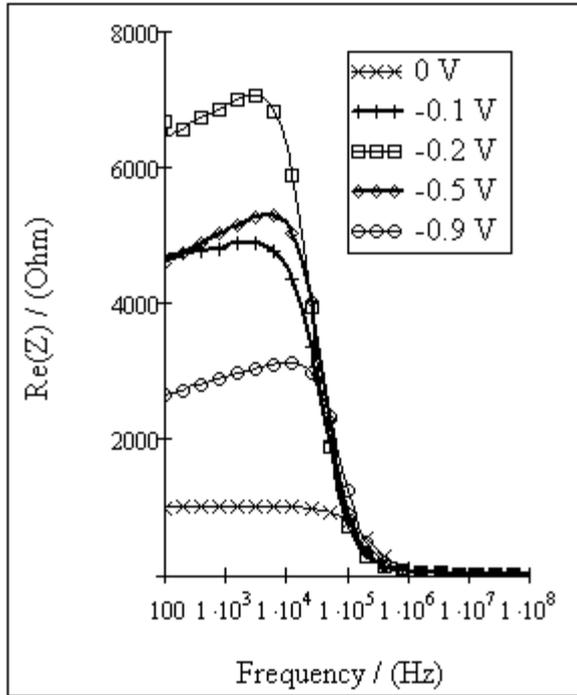
Fig. 3.5.1.1. Structure of glass/ITO/CISe/graphite impedance real part dependence on measuring signal frequency at zero and reverse biases

On the Fig. 3.5.1.1 there are represented results of the glass/ITO/CISe/graphite structure measurements for the real part of the impedance. Frequency used in the measurements is in the range of 100 Hz to 100 MHz. The amplitude of the modulation signal was used 30 mV. At low frequency range of 100 Hz to about 50 kHz there are seen the resistive behavior there the real part value approaches or follows a tilted plateau like trend and the value at a certain voltage is almost constant. An important feature of this plateau is that the resistance gradually decreases as the frequency decreases.

In the middle frequency range of about 50 kHz to 1 MHz there is seen the capacitance like shunting behavior there the resistance decreases as the frequency increases. At certain point about 1 MHz the slope of the decreasing resistance changes and finally the values of the high frequency resistance obtain very close values so that measurements at different biases can be distinguished only in a smaller scale.

This trend is common for all biases in the range of 0 to -1 V that was under investigation. Curves measured at different biases are most prominently different in the low frequency range there the low frequency tilted plateau appears. The value of the low frequency resistance is lowest at 0 V. The resistance increases first as

67

the reverse bias increases in the range of 0 to about -0.2 V and then the resistance decreases again. This behavior is common for the depletion behavior at small reverse biases. If the reverse bias increases further the shunting behavior appears that violates the pure depletion behavior.
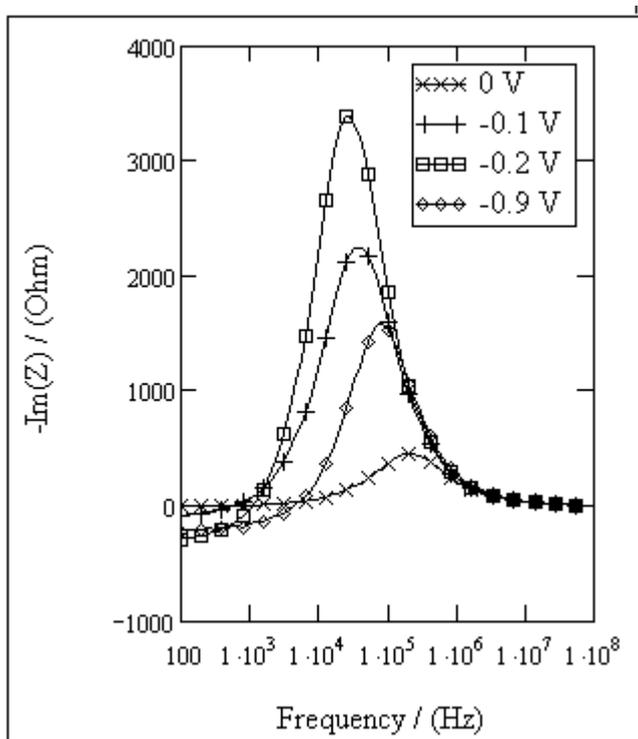
Fig. 3.5.1.2. Structure of glass/ITO/CISe/graphite impedance imaginary part dependence on measuring signal frequency at zero and reverse biases

On the Fig. 3.5.1.2 there are represented results of the glass/ITO/CISe/graphite structure measurements for the imaginary part of the impedance. From these results it is possible to distinguish three frequency regions of distinct behavior. At low frequency range of 100 Hz to 2 kHz the resistance approaches to a limiting value that lies possibly at frequencies lower than 100 Hz. In the range about 2 kHz to 1 MHz there is a region for the maximum values of the resistance that can be described as a switching region there the resistance is first caused by the purely resistive element at low frequency and then by capacitive element at medium frequencies. As a fact the capacitive resistance disappears at very high frequencies. An important feature of these curves is that at low frequency and at all reverse biases under consideration, the imaginary value of the impedance changes a sign. This is clearly characteristic to some kind of inductive phenomenon in this electrical behavior. Only at 0 bias and at forward biases this phenomenon does not

68

appear in such an extent that could result in the change of the sign. The position of the impedance imaginary part maximum value depends clearly on the applied reverse voltage. The value of the maximum resistance frequency decreases as the value of the maximum resistance increases.
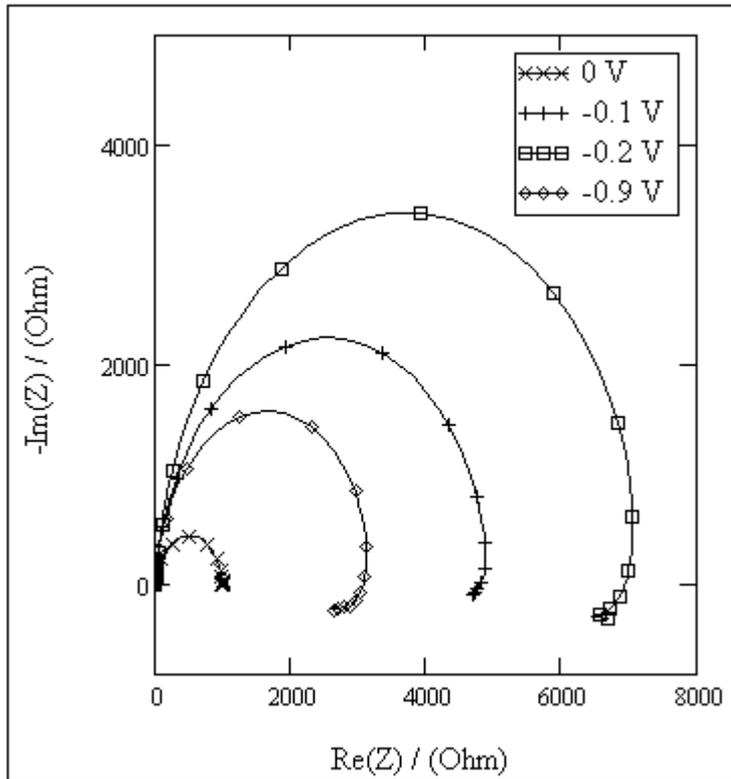
Fig. 3.5.1.3. Structure of glass/ITO/CISe/graphite Nyqvist plots at zero and reverse biases

On Fig. 3.5.1.3 there are represented the Nyqvist plot of the glass/ITO/CISe/graphite structure which comprehends the data given in Figs. 3.5.1.2 and 3.5.1.3. Nyqvist plots show that impedance arcs are somewhat deformed and thus the structure must deviate from the ideal *RC* behavior. Also is the low frequency part of the Nyqvist plot summarizing the two important features revealing on the impedance real part and impedance imaginary part plots. Namely this is that the imaginary part changes the sign and at the same time the real part decreases as the frequency decreases.

The arcs diameter grows as the reverse bias increases up to -0.2 V and then gradually decreases as the shunting current through the depletion barrier grows higher.
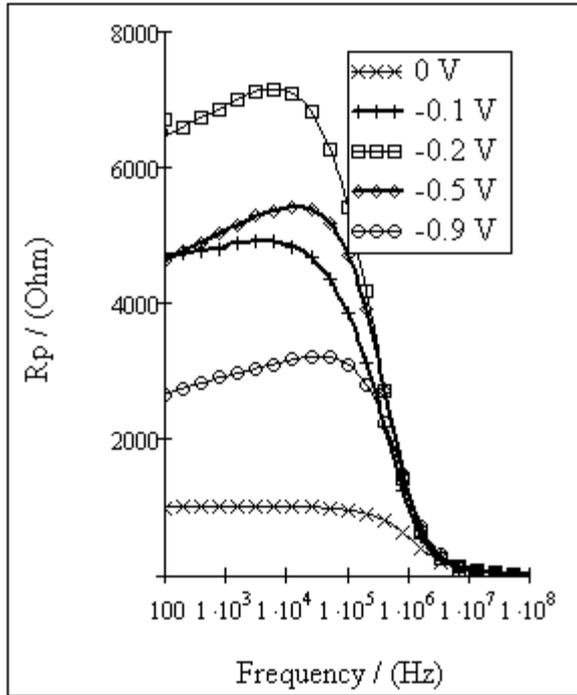
Fig. 3.5.1.4. Structure of glass/ITO/CISe/graphite parallel resistance vs. frequency plots at zero and reverse biases

On Fig. 3.5.1.4 and Fig. 3.5.1.5 there are represented impedance results in a simple parallel RC circuit form. The results for parallel resistance R_p are very similar to the impedance real part representation. Representation in a linear scale stress the feature of decreasing value of the parallel resistance as the frequency decreases at low frequencies. This feature almost disappears at zero bias.
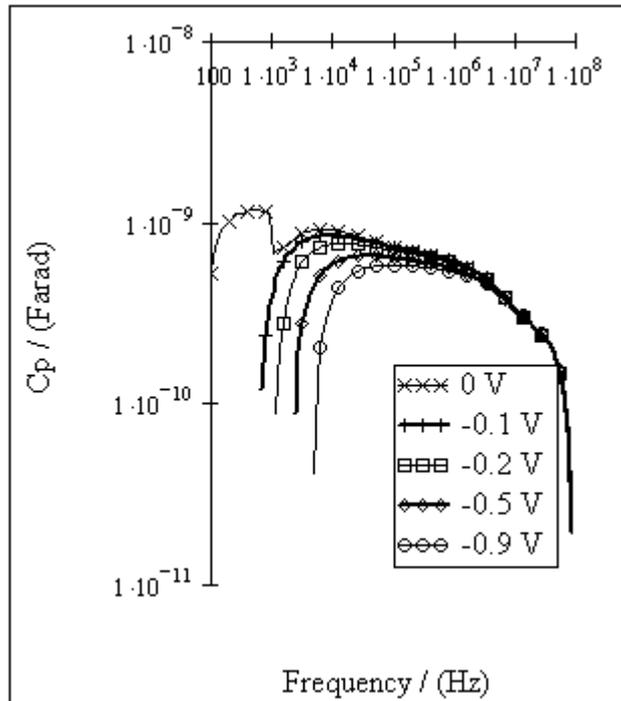
Fig. 3.5.1.5. Structure of glass/ITO/CISe/graphite parallel capacitance vs. frequency plots at zero and reverse biases

On parallel capacitance plots these specific features, found on imaginary part frequency behavior, namely the change of the sign at low frequency, are also present and manifest themselves as a negative capacitance behavior at low frequencies.

3.5.2. THE MODELING OF THE IS RESULTS

The modeling of the impedance response was held in Labview program using Monte Carlo simulation method. The modeling was held in three steps.

First the basic modeling circuit was chosen to model the entire frequency range with an acceptable deviation from the experimental data. The best models exhibited a deviation from the experimental data in the range of the 10%. As a result two circuits with almost the same accuracy were found to describe the data.
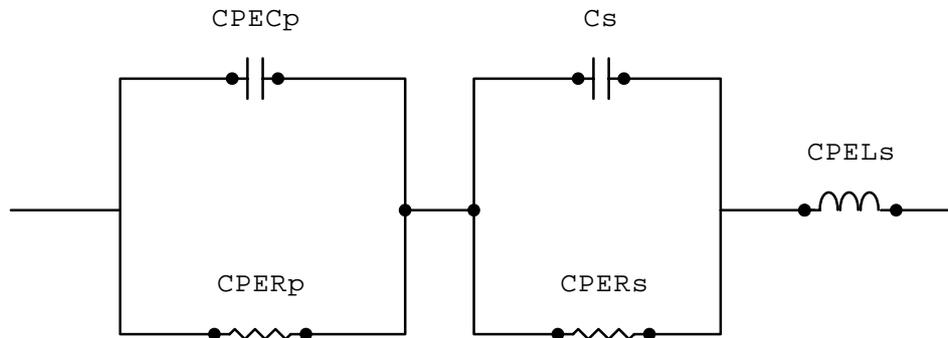
Fig. 3.5.2.1. Equivalent circuit found to describe the impedance behavior of the glass/ITO/CISe/graphite structure (CPE notation in names of circuit elementsof CPE C_p, CPE R_p, CPE R_s and CPE L_s points to the circumstance that these elements are CPE elements resembling either capacitors, resistors or inductors)

On Fig. 3.5.2.1 there is represented a circuit which resembles a two parallel *RC* connections in series with an inductive element. As a difference there are CPE used instead of capacitance and resistance in one of these blocks (marked as CPE Cp for a capacitive element and CPE R_p for a resistive element). In the second block there was also used a CPE element for a resistive element, but the element in parallel (*Cs*) was used as an ideal capacitance. Additionally there is a CPE with strongly inductive properties but not an ideal inductance.
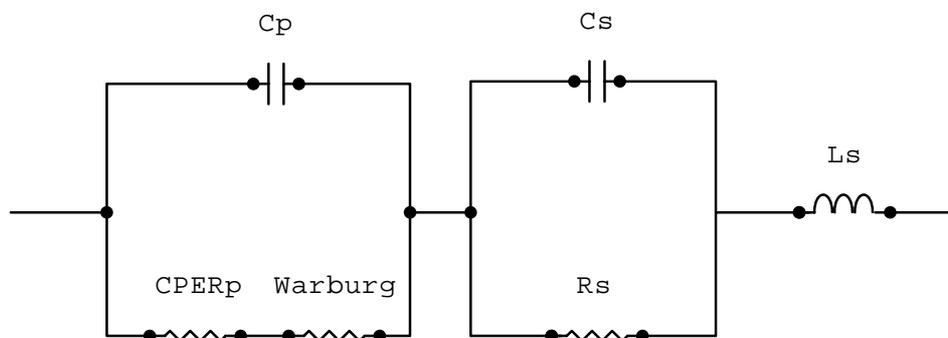
Fig. 3.5.2.2. Equivalent circuit found to describe the impedance behavior of the glass/ITO/CISe/graphite structure (CPE notation in the name of circuit element CPE R_s points to the circumstance that this element is a CPE element resembling a resistor, Warburg is the CPE element with n=0.5)

Another circuit describing the overall impedance behavior with a single set of parameters is represented on Fig. 3.5.2.2. In that circuit the former CPE connection

is replaced by a Randles-like circuit configuration [50] there a simple resistor in series with the Warburg element (an ordinary Randles configuration) is replaced by a resistor-like CPE. All other elements are ideal inductance, ideal capacitance and ideal resistance. It was found that this network describes the system well mathematically. Because of direct current considerations the equivalent circuit represented on Fig. 3.5.2.1 is preferred in this work and all the calculations are based on the modeling results of that circuit.

The preference rises because of the direct current impedance limit which has a finite value. If a circuit containing a Warburg element is used, the direct current limit has an infinite value in case of fixed parameters.

In the second step of the modeling, the frequency range used for finding a parameter values was shrank to a one decade of a frequency or even less. The value of the inductive parameter was kept constant but other parameters were found in a sliding mode of modeling. As a result the parameters were obtained as frequency dependent circuit element parameters.

In the third modeling step, the values of CPE elements parameters Q and p were used to model the CPE response in terms of physically meaningful capacitances and resistors.
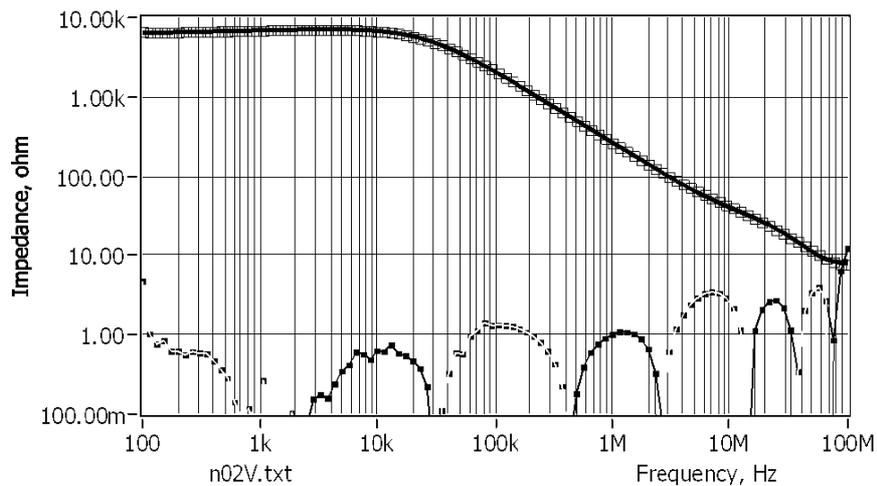
Fig. 3.5.2.3. Modeling of the impedance amplitude response of the glass/ITO/CISe/graphite structure: -0.2 V (square dots correspond to the experimental result, solid line corresponds to the fit, line with the smoother filled dots report the error percentage)
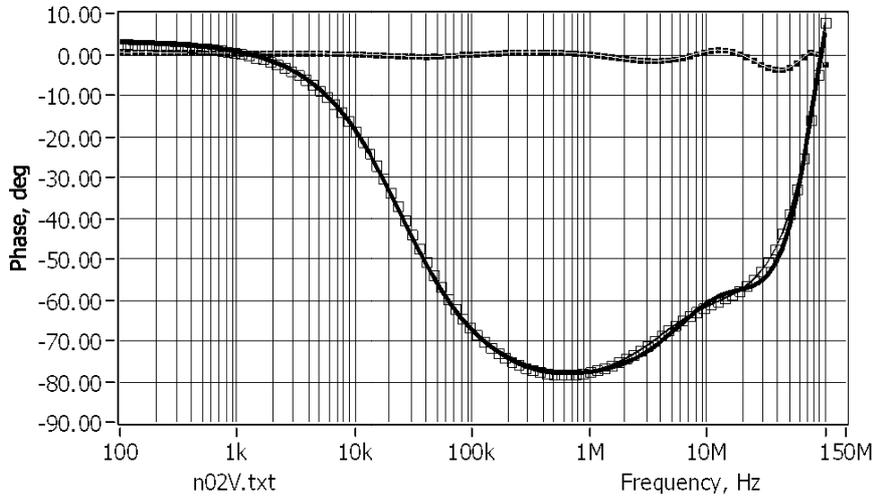
Fig. 3.5.2.4. Modeling of the impedance phase response of the glass/ITO/CISe/graphite structure: -0.2 V (empty square dots correspond to the experimental results, solid line corresponds to the fit, line with the smoother filled dots reports the error percentage)

On the Fig. 3.5.2.3 and 3.5.2.4 there is represented an example of the modeling with the circuit exhibited on the Fig. 3.5.2.1. The best fit is obtained at low frequencies there the error is in the range of 8% in the case of impedance modulus and about 1% in the case of impedance phase. At higher frequencies (100 kHz and higher) the modeling error increases up to 12% in case of impedance modulus and up to about 2% in case of impedance phase. The most obvious disagreement in these modeling results is seen in the impedance phase behavior at frequencies around 10 MHz. This phase knee there can be described approximately with a *RC* parallel connection according to the circuit on Fig. 3.5.2.1 and 3.5.2.2.

Table 3.5.2.1. Numerical results of the modeling using the circuit depicted on Fig. 3.5.2.1 (In the Table 3.5.2.1 the results of the modeling are represented in columns for every applied bias value. Dimensions are not shown (look for dimensions in Eqs. 1.6.2 – 1.6.4 in Literature Review for Rp_Q, Cp_Q, Rs_Q, Cs_Q, Ls_Q. Remaining Rp_n, Cp_n, Rs_n, Cs_n and Ls_n are dimensionless.))

Bias	0 V	'-0,1 V	'-0,2 V	'-0,3 V	'-0,4 V	'-0,5 V	'-0,6 V	'-0,7 V	'-0,8 V	'-0,9 V	'-1 V
Rp_n	9,56E-99	-1,11E-02	-3,19E-02	-3,77E-02	-3,83E-02	-4,07E-02	-4,07E-02	-4,30E-02	-4,65E-02	-4,91E-02	-4,76E-02
Rp_Q	9,93E-04	2,26E-04	1,90E-04	2,19E-04	2,44E-04	2,81E-04	3,20E-04	3,77E-04	4,43E-04	5,30E-04	6,02E-04
Cp_n	9,17E-01	9,19E-01	9,21E-01	9,14E-01	9,29E-01	9,29E-01	9,29E-01	9,34E-01	9,32E-01	9,25E-01	9,22E-01
Cp_Q	2,33E-09	2,19E-09	2,07E-09	2,20E-09	1,74E-09	1,70E-09	1,67E-09	1,54E-09	1,56E-09	1,73E-09	1,78E-09
Rs_n	-4,11E-02	-4,23E-02	-4,64E-02	-4,37E-02	-4,27E-02	-4,24E-02	-4,27E-02	-4,39E-02	-4,36E-02	-4,26E-02	-4,10E-02
Rs_Q	1,22E-01	1,25E-01	1,43E-01	1,50E-01	1,17E-01	1,22E-01	1,30E-01	1,29E-01	1,32E-01	1,70E-01	1,72E-01
Cs_n	9,77E-01	9,90E-01	9,91E-01	9,76E-01	9,36E-01	9,33E-01	9,60E-01	9,28E-01	9,35E-01	9,79E-01	1,01E+00
Cs_Q	7,56E-10	5,54E-10	5,68E-10	7,65E-10	1,57E-09	1,67E-09	1,01E-09	1,90E-09	1,60E-09	7,34E-10	4,30E-10
Ls_n	-5,29E-01	-5,41E-01	-5,36E-01	-5,60E-01	-5,65E-01	-5,64E-01	-5,64E-01	-5,60E-01	-5,75E-01	-5,69E-01	-5,73E-01
Ls_Q	4,24E+03	5,23E+03	4,79E+03	7,98E+03	8,67E+03	8,57E+03	8,43E+03	8,03E+03	1,06E+04	9,32E+03	1,00E+04

74

In the Table 3.5.2.1 the first two rows there are represented results for the values of resistor-like CPE Q and n values. Small n values indicate that this element only slightly deviates from the ideal resistor behavior but its parameter Q still does not have a correct dimension needed for resistor: C/s·V. Also the values of n are negative that indicates that this resistor-like CPE is affected by some kind of inductive-like phenomenon in the structure. These negative values are responsible for the ability to model the low frequency behavior of the impedance modulus as well as the impedance real part. The negative n in that place causes these quanta to decrease with decreasing frequency.

At the same time, the trend of Q, then the bias is getting more reverse, also mirrors the behavior of the real part (Fig. 3.5.1.1) and Rp (Fig. 3.5.1.4). At -0.2 V there is a minimum that corresponds to the maximums in the Rp frequency plot and real part results because Q value describes roughly a resistor-like phenomenon if the reverse value of the number is taken.

The third and the fourth row do represent the capacitor-like CPE n and Q respectively. Here again, the value of n deviates from 1 in remarkable amount and this indicates that CPE cannot considered as a pure capacitive element, but with some deviations which are pointing to some kind of resistive or diffusive phenomena in this electrical situation. The dimension of Q is not appropriate for making use as a capacitance and the process behind it is not clear and thus must be considered as a special question.

Values of the CPE-Rs n in the fifth row are negative that also points to some kind of inductive-like phenomenon in that element. The trend of the values is not that clear, but in general the values tend to decrease as the reverse bias increases.

Values of CPE-Q in the sixth row do increase as the reverse bias increases. This may point to the process there the base area of the structure becomes thinner with the increasing reverse bias. This is an expected behavior connected with the broadening of the depletion region.

The value of n in the seventh row was kept constant because otherwise in some bias conditions it tended to have values slightly more than 1. These are anomalous values because n should have values only in the range of -1 to 1.

Cs values in the eight row have a minimum at -0.4 V. From this behavior this is not absolutely clear if this mirrors the behavior of an opposite barrier in the structure caused maybe by a second surface or is this simply a geometric capacitance of the base part of the structure.

Two last rows describe the results for the inductance like CPE. The most remarkable there are the values of n of the corresponding CPE. The range of -0.5 to -0.6 somehow indicates that maybe there exists some physical phenomenon that is an analog of Warburg elements describing different type of processes of diffusion but in that is connected with inductive phenomena.
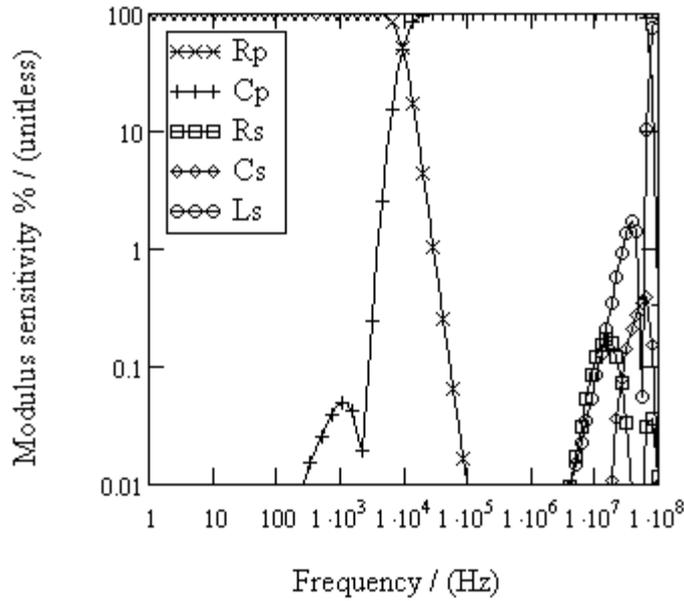
Fig. 3.5.2.5. Sensitivity analysis of the impedance modulus according to the formula of the circuit represented on the Fig. 3.5.2.1 (reverse bias -0.3 V as an example)
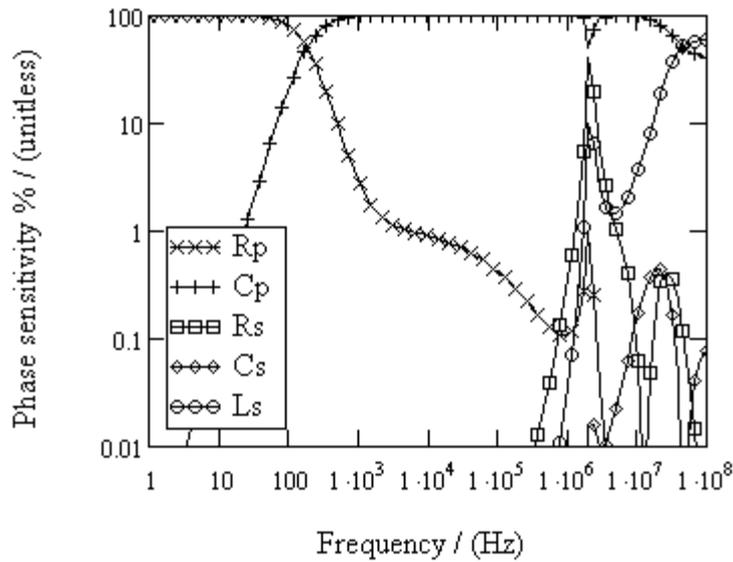
Fig. 3.5.2.6. Sensitivity analysis of the impedance phase according to the formula of the circuit represented on the Fig. 3.5.2.1 (reverse bias -0.3 V as an example)

On the Fig. 3.5.2.5 and Fig. 3.5.2.6 there are represented results for the sensitivity of the modulus and the phase if the change of the parameter values is 1%. For calculations there were used a well known error analysis algorithm that makes use of the partial derivatives of the variables in consideration and the estimations of the corresponding errors:

$$\Delta Z^2 = \left(\frac{\partial f(x_1, x_2, \ldots)}{\partial x_1}\right)^2 \Delta x_1 + \left(\frac{\partial f(x_1, x_2, \ldots)}{\partial x_2}\right)^2 \Delta x_2 + \cdots \qquad (3.5.2.1)$$

there ΔZ^2 is a square of a total error estimation, $f(x_1, x_2, \ldots)$ is a formula in consideration and Δx is the individual error estimation of the parameter.

In these calculations of sensitivity estimation, the value of the "error" was taken 1% in case of every single parameter and the sensitivity was calculated as the percentage change due to the parameter in consideration making up a part of the total change. The influence of CPE Q and n values were summed together in one number to have a better overview of a single CPE element as such.

Plots on the Figs. 3.5.2.5 and 3.5.2.6 were calculated using the parameter fit values obtained for the -0.3 V bias conditions. The overall behavior, except of CPERs, is similar at all bias conditions.

The element of CPE-Rp is most influential to the impedance modulus at low frequencies up to about 10 kHz. The influence on the impedance phase starts to decrease at lower frequencies so that at 1 kHz the influence of it is in the range of 1 %. The influence of the CPE-Cs starts to increase quickly at the frequencies of 5 kHz while affecting the modulus and of 100 Hz while affecting the phase of the impedance. Other elements become influential at frequencies higher than 1 MHz while considering the impedance phase and higher than 10 MHz while considering the impedance modulus.
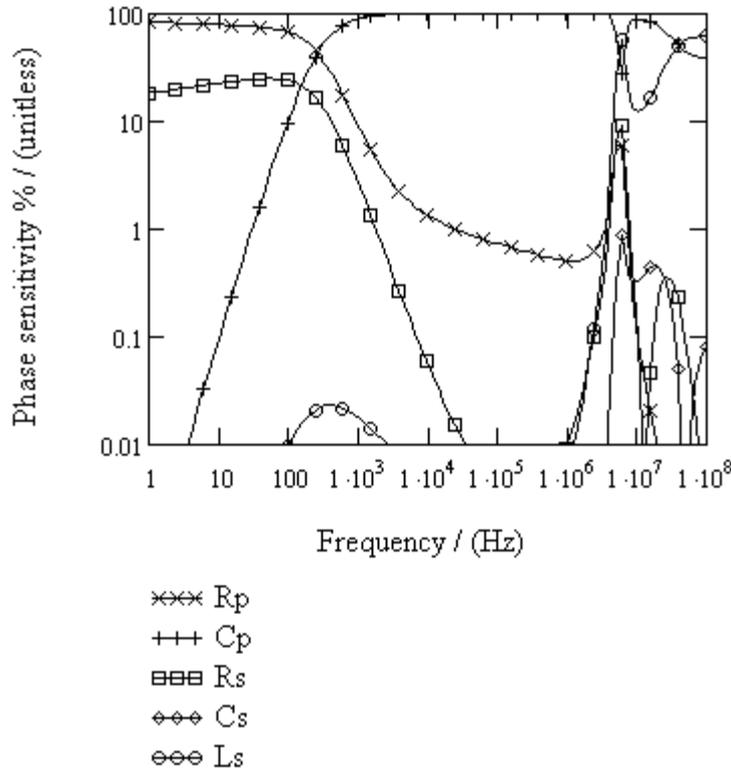
Fig. 3.5.2.6a. Sensitivity analysis of the impedance phase according to the formula of the circuit represented on the Fig. 3.5.2.1 (forward bias 0.1 V)

At 0 V and at higher biases the CPE-Rs start to have a more significant influence at low frequency range (Fig. 3.5.2.6a). From the corresponding plot describing the influences of separate elements, it turns out that about 80% of the phase is built up of CPE-Rs at frequencies 10 Hz and less if there is an open circuit condition of 0 V. This influence decreases at forward biases. For example at the bias of 0.1 V this value has rapidly decreased to 20%. This finding is used then estimating the mobility of majority carriers by using the impedance measured at forward bias.

3.5.3. CALCULATIONS OF A DEPLETION LAYER CAPACITANCE VALUES USING CPE

Results of the modeling with the sliding mode where the modeling range was restricted in one decade of frequency are represented in the Appendix A1. Q and n values of corresponding CPE elements do not have an independent physical meaning and therefore this must be a specially considered question.
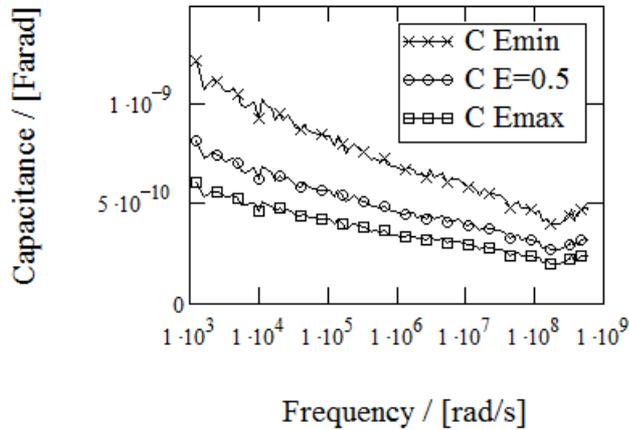
Fig. 3.5.3.1. Capacitance calculated according to two limiting conditions of E (E_{min} and E_{max}) and at E=0.5 (curve of E_{max} corresponds to the situation, then E=1, curve of E_{min} is then Eq. 1.6.14c is used, reverse bias -0.2 V)

On the Fig. 3.5.3.1 there is represented a typical result of calculations there an initial CPE obtained from the modeling (Appendix A1) is converted into capacitance and another CPE (a modula CPE) using Eq. 1.6.11 and Eq. 1.6.12.

These two results differ about factor of two depending on the value of the proportionality factor E. Values of capacitance obtained then E is chosen in between of E_{min} (Eq. 1.6.14c) and E_{max} (E=1)situate inside the range specified by these two limiting values of capacitance. Values of E>1 turned out to be inapplicable and do not have physically reasonable parameter values if Eq. 1.6.11 and Eq. 1.6.12 are used.
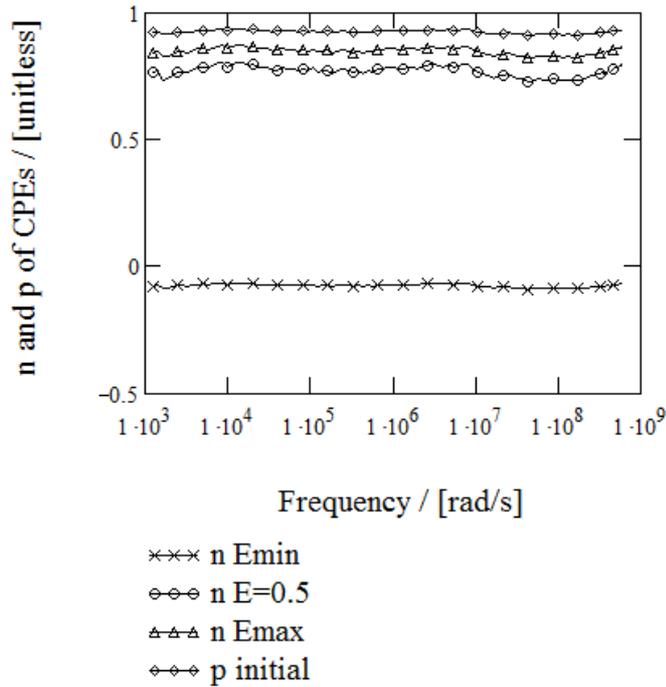
Fig. 3.5.3.2. Exponential parameters (*n*) of CPE calculated according to two limiting conditions, with *E*=0.5 and compared with the curve of initial CPE exponential parameter (*p*) (curve of E_{max} corresponds to the situation, then *E*=1, curve of E_{min} is then Eq. 1.6.14c is used, reverse bias -0.2 V)

On the Fig. 3.5.3.2 there are represented limiting values for the exponential parameter of modula CPE (*n*) calculated according to the Eq. 1.6.9 and compared with that of initial CPE (*p*). Values of *n* are always less than the initial *p*, but at the same time the possible range is about half of the entire range of *n* values physically reasonable (-1 to 1). Also it is remarkable that the *n* values corresponding to E_{min} (Eq. 1.6.14c) are slightly negative. Again, values of *n*, if *E* is chosen between limiting values (here *E*=0.5), are situating in between of these limiting values.
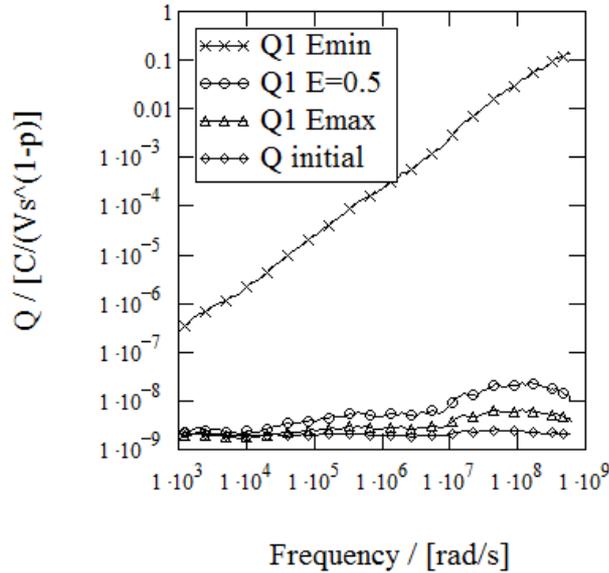
Fig. 3.5.3.3. Q_1 **of CPE calculated according to two limiting conditions and compared with the Q_1 values of the condition with an arbitrary $E=0.5$ and with the curve of Q of initial CPE (curve of E_{max} corresponds to the situation, then $E=1$, curve of E_{min} is then Eq. 1.6.14c is used, reverse bias -0.2 V)**

On the Fig. 3.5.3.3 there are represented results for the calculation of Q_1 for the modula CPE according to the Eq. 1.6.10 and Eq. 1.6.12 in case of limiting values of E (E=1 and using Eq. 1.6.14c), $E=0.5$ and these are also compared with the values of Q of initial CPE. There can be seen that the less is E the more the Q_1 depends on frequency. Because these results are not needed independently as means for the calculation of material physical parameters, these are not discussed here.

3.5.4. CALCULATIONS OF A DEPLETION LAYER RESISTANCE AND SERIES RESISTANCE VALUES USING CPE

In this work the initial CPE obtained from the modeling (with p values close to zero and slightly negative) is converted into a series resistance and a series modula CPE (a comparison with the conversion into parallel resistance and parallel modula CPE is given later) using Eq. 1.7.1.4 to Eq. 1.7.1.7 as general equations with any value of E (proportionality factor). This configuration is chosen because of dc consideration. At dc conditions such an initial CPE should have a finite value that corresponds to the resistance (in this case depletion region parallel resistance). If a modula CPE was chosen in parallel, its dc impedance was zero, so shunting the resistor and giving a zero resistance at dc situation.
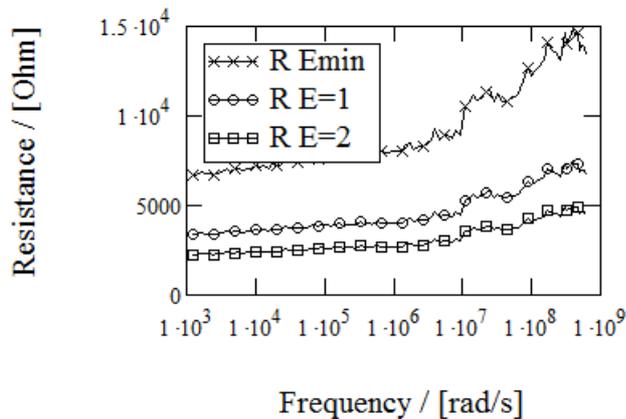
Fig. 3.5.4.1. Resistance calculated at different values of *E* for converting a resistive-like CPE into resistance and modula CPE (curve of $E_{\min}$ corresponds to the situation, and then *E* is calculated according to Eq. 1.7.1.8a, reverse bias -0.2 V)

On the Fig. 3.5.4.1 there is shown how the resistance value calculated generally from Eq. 1.7.1.6 and Eq. 1.7.1.7 depends on the value of *E* that is the proportion between the modulus of resistance and the modulus of the modula CPE. If *E* increases the resistance decreases monotonically. As a test situation for choosing an appropriate value of *E* there will be used a comparison with the applied bias at the structure under consideration.
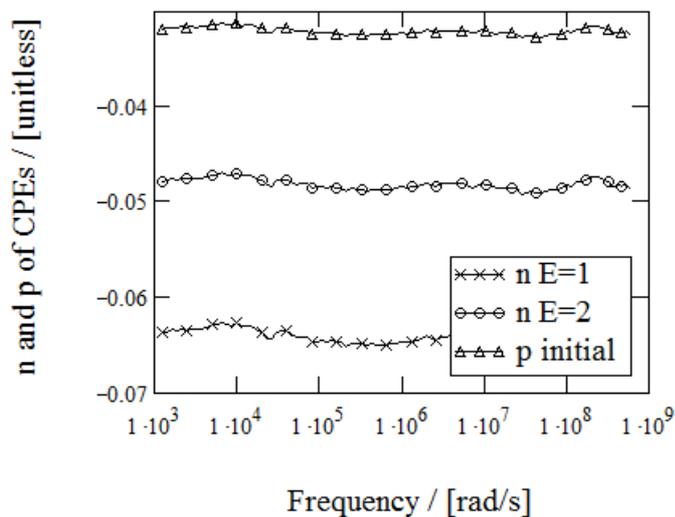
Fig. 3.5.4.2. Exponential parameters (n) of the modula CPE calculated according different values of *E* and compared with the curve of initial CPE exponential parameter (p) (reverse bias -0.2 V)

On the Fig. 3.5.4.2 there are represented results for calculation of the values of the exponential parameters of n for the modula CPE according to the Eq. 1.7.1.4 if the E values are changed. E_{min} result (Eq. 1.7.1.8a) is not shown because it masks other results in scale as it has values slightly less than -1. If E increases the value of n approaches that of initial p.
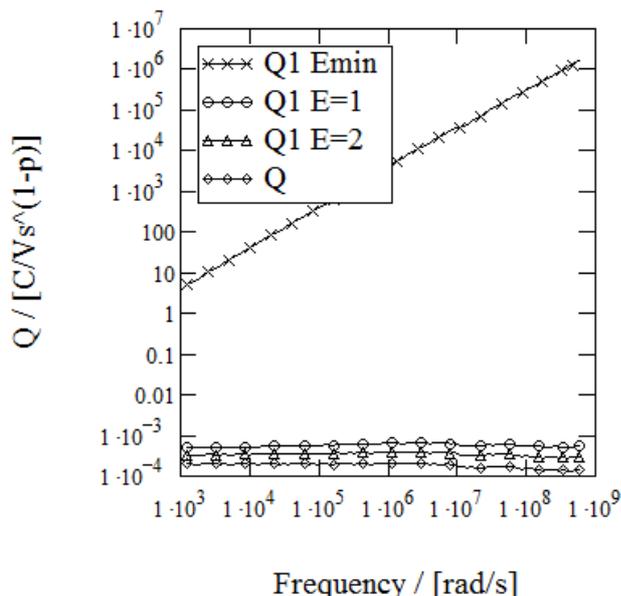
Fig. 3.5.4.3. Q_1 of modula CPE calculated in case of different values of proportionality factor E (curve of E_{min} corresponds to the situation, then E is calculated according to Eq. 1.7.1.8a, reverse bias -0.2 V)

On Fig. 3.5.4.3 there are represented results of the calculation of Q_1 of the modula CPE according to the Eq. 1.7.1.5 and Eq. 1.7.1.7. If E_{min} (Eq. 1.7.1.8a) is used for calculations, the Q_1 is strongly frequency dependent. This dependence decreases as higher values of E are used. Finally if an infinite value of E is used the Q_1 approaches the value of Q of initial CPE.

3.5.5. EVALUATION OF PROPORTIONALITY FACTOR E FOR A RESISTANCE-LIKE CPE

An evaluation of the proportionality factor E could be obtained then the resistances calculated using Eq. 1.7.1.6 and 1.7.1.7 or Eq.1.7.1.14 and Eq. 1.7.1.15 are compared with the differential resistance obtained from the *I-V* curve of the structure. On the Fig. 3.5.2.5 and Fig. 3.5.2.6 of parameter influence evaluation there can be concluded that the dominant circuit element at low frequencies (10

kHz and lower in case of impedance modulus and 100 Hz and lower in case of impedance phase) and at reverse biases is the parallel resistance-like CPE.

This means that the differential resistances calculated from that CPE must give same values that can be obtained from the *I-V* curve.
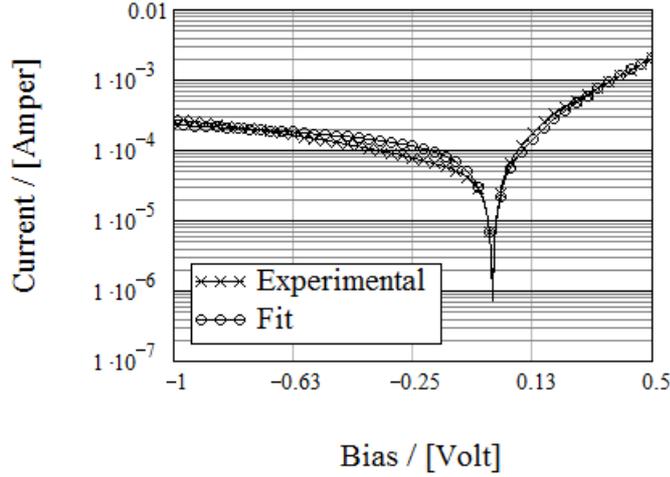
Fig. 3.5.5.1. *I-V* curve of the structure of glass/ITO/CuIn$_3$Se$_5$/graphite measured in dark conditions (contact area 2 mm^2)

The *I-V* curve represented on Fig. 3.5.5.1 was fitted with the equation of the "real" solar cell in dark conditions using the equation of

$$J(V) = J_0 \left(e^{\frac{q(V - R_{ser}J)}{nkT}} - 1 \right) + \frac{V - R_{ser}J}{R_{sh}} \qquad (3.5.5.1),$$

where Q is the elementary charge, *J(V)* is the current density at the applied voltage V, J_0 is the dark current density, R_{ser} is the serial resistance of the junction, R_{sh} is the shunt resistance of the junction barrier, n is the ideality factor, k is the Boltzman coefficient and T is the temperature.

The results show that the estimation for the ideality factor is n=5.47, for the dark current J_0=86 μA, series resistance R_s=36 Ohm and shunt resistance R_p=6.8 kOhm.

At reverse side of the *I-V* curve the differential resistance was calculated numerically from the experimental data for the comparison with the resistance-like CPE Q value and resistance values obtained from Eq. 1.7.1.6 and Eq. 1.7.1.7.
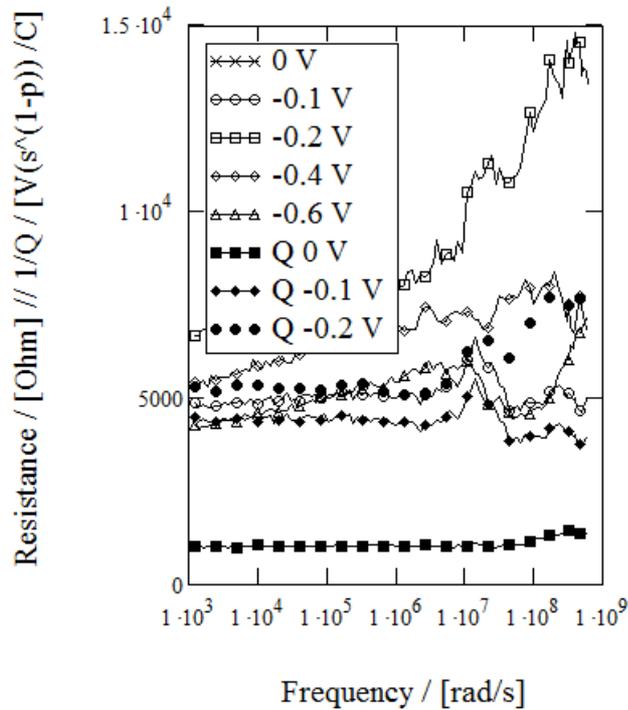
Fig. 3.5.5.2. *Q* values of the resistance-like CPE compared with resistance calculated according to Eq. 1.7.1.6 and Eq. 1.7.1.7 (with E_{min}) at different reverse bias conditions

According to the influence analysis (Figs. 3.5.2.5, 3.5.2.6) trusted values of *Q* can be obtained at low frequencies up to 10 kHz (about 10^5 rad/s). Resistance values calculated according to Eq. 1.7.1.6 and Eq. 1.7.1.7 decrease as the frequency decreases.

This is probably a sign of inapplicability of CPE analysis under consideration and maybe somewhat different transformation of the resistance-like CPE is needed. This phenomenon can be briefly analyzed using the definition of the differential resistance:

$$R = \frac{dV}{dI} = \frac{dV \cdot s}{dQ} \qquad (3.5.5.1)$$

where *dV* is an infinitesimal change of the voltage, *dI* is an infinitesimal change of the current, *dQ* is an infinitesimal change of a charge and *s* is a period of the change.

As *s* increases then the frequency decreases, and also *dQ* increases, the *R* should remain the same. If there is a decrease in the value of *R*, then it may be only then the *dQ* increases more than the s does. If more charge flows through the structure and causes a bigger *dI* when the period increases, this may be due to some relaxation processes that consume more charge at low frequencies so that the

85

change in potential must be build up on a bigger amount of charge and current. On the other hand this increase of the *dQ* would not be expected to be an increase of the charge storage that is a capacitive phenomenon.

For comparison with *R* calculated from *I-V* curve the most low frequency values of *R* and *Q* of resistance like CPE are used.
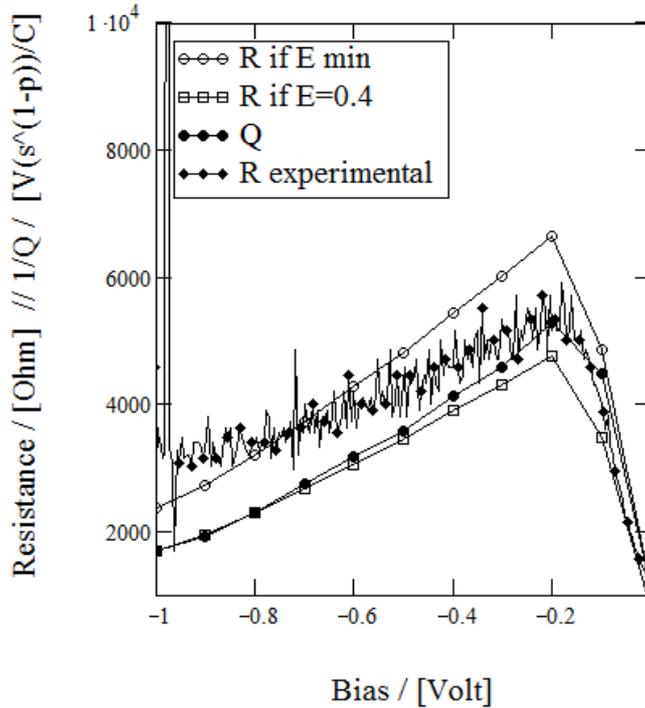
Fig. 3.5.5.3. Comparison of *I-V* measurement (reverse bias) based differential resistance with the resistance predicted from Eq. 1.7.1.6 and Eq. 1.7.1.7, and the *Q* of the resistance-like CPE (measurement frequency 200 Hz)

From the Fig. 3.5.5.3 there can be given an estimation of factor *E*. As there is not any plateau seen on Fig. 3.5.5.2 it is not possible to expect that the frequency used in the calculations (200 Hz) is appropriate for making a comparison with an *I-V* curve based differential resistance. There can be concluded that the minimum possible value of *E* must be used if this concept is valid. If the resistance curve calculated in the case of E_{min} had higher values at all potentials in comparison with the *I-V* curve based differential resistance, there would have been more support to the calculations under discussion.

Finally there must be concluded from this figure that E_{min} value is a most probable estimation for the calculation of *R* values if any. The reason why this test tends to fail may be that the frequency used is too high on one hand and the scan rate of the measurement of the *I-V* curve was too low (5 mV/s). If the frequency of

86

the measuring signal and the scan rate would have been somewhat more comparable in terms of the mean rate of the potential change the conclusion about the test result was to be more adecvate.
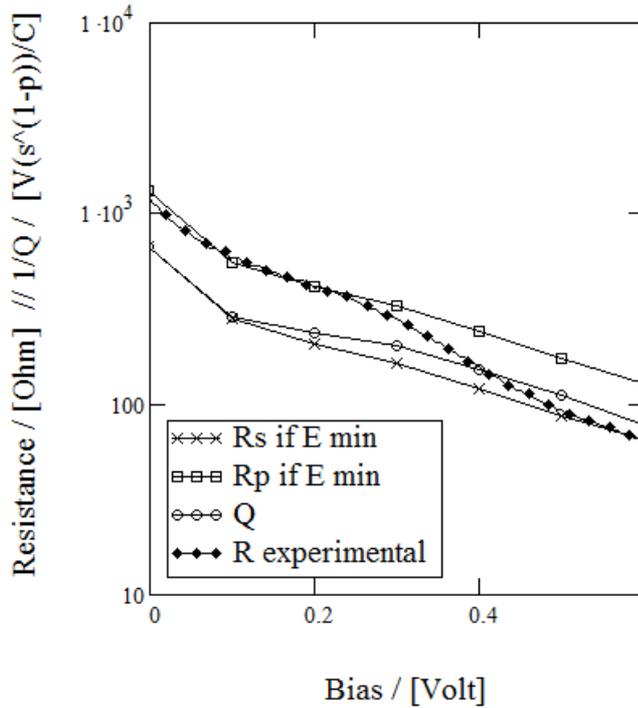
Fig. 3.5.5.4. Comparison of *I-V* measurement (forward bias) based differential resistance with the resistance predicted from Eq. 1.7.2.10 and the *Q* of the resistance-like CPE (measurement frequency 200 Hz)

More promising results of the calculated resistance values can be obtained then the forward bias is applied to the junction. Here it can be seen that at low forward biases the resistance values calculated according to the Eq. 1.7.2.10 (transform corresponding to the Fig. 1.6.1 b) match well with the experimental value of the differential capacitance, calculated from the *I-V* curve. At higher biases around 0.3 V this mach disappears, but then the resistances calculated according to the Eq. 1.7.1.6 and Eq. 1.7.1.7 (transform corresponding to the Fig. 1.6.1 a) seem to match with the experimental differential capacitance.

This must be noted here that the voltage drop caused by the series resistance is not taken into account here. This may point to the possibility that really the match of the resistances calculated according to the Eq. 1.7.1.6 and Eq. 1.7.1.7 is a coincidence but the applicability range of the Eq. 1.7.2.10 is even wider.

3.5.6. COMPARISON OF THE PARALLEL CAPACITANCE – PARALLEL RESISTANCE IMPEDANCE RESPONSE WITH THE IMPEDANCE RESPONSE OF THE MODULA CPE´S

There is a question about that do the modula CPE, that are calculated according to the method proposed here, really does mean. It is hardly possible to find physical meaning to the parameter of Q of modula CPE as this is reported on Fig. 3.5.2.5 and Fig. 3.5.2.6. To find out about this question, this is possible to merge two modula CPE-s into the on modula impedance. This is possible if both initial circuit elements (CPE-Rp and CPE-Cp) are converted into the ideal element and the modula element in parallel (Fig. 1.6.1 b). In this case, both modula elements appear to be connected in parallel and their impedance response can be merged into single impedance.

Schematically this is represented on the Fig. 3.5.6.1.
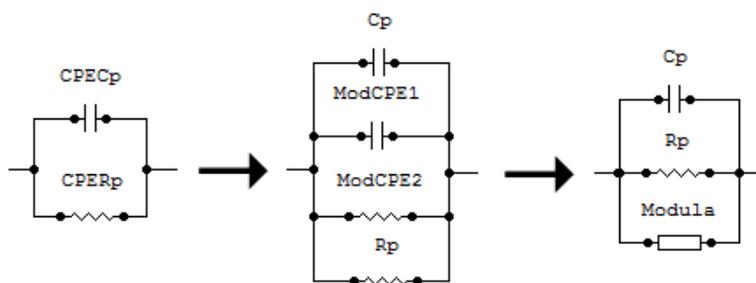
Fig. 3.5.6.1. Conversion of the experimentally found parallel connection of CPE-Cp and CPE-Rp into the parallel connection of capacitance, resistance and modula impedance
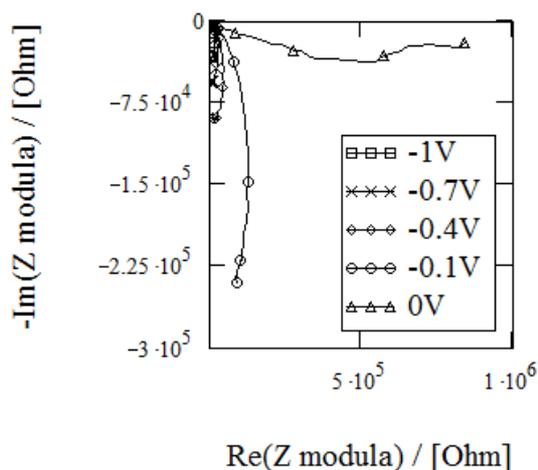
Fig. 3.5.6.2. Nyqvist plots of the modula impedance calculated according to the transformation schematically reported on Fig. 3.5.6.1
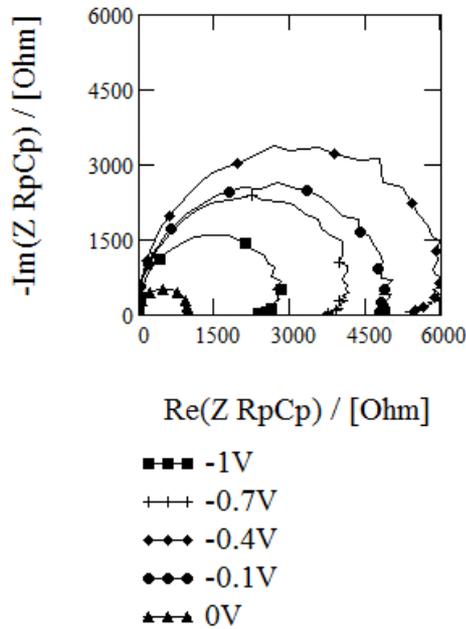
Fig. 3.5.6.3. Nyqvist plots of the impedance of the resistance and capacitance in parallel calculated according to the transformation schematically reported on Fig. 3.5.6.1

On the Fig. 3.5.6.2 there are reported Nyqvist plots of the modula impedance. The conclusion that can be made upon these curves is that the influence of the modula impedance becomes more significant at higher reverse biases. More investigation is needed to find out the origin of such phenomenon.

On the Fig. 3.5.6.3 there are reported the results of the Nyqvist plots of the parallel connection of the resistance and capacitance that are calculated according to the flow diagram of Fig. 3.5.6.1. Here is apparent that the values of the imaginary part do not change the sign as there was observed in the experimental data (Fig. 3.5.1.3). At the same time at low frequencies there is a bending caused by the decrease of the resistance values at low frequencies. This phenomenon was already reported on

Fig. 3.5.4.1 and Fig. 3.5.5.2. This phenomenon is also of unknown origin and possibly points to the fact that some other kind of conversion is appropriate for subtracting the modula impedance and the resistance (as well as the capacitance).
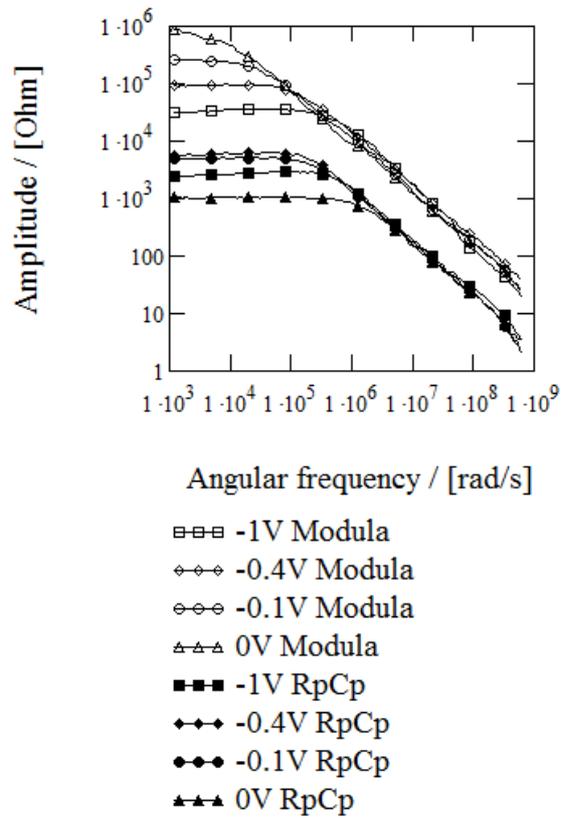
Fig. 3.5.6.4. Comparison of amplitudes of the impedance of the connection there the resistance and the capacitance are in parallel, and that of the modula impedance. (responses corresponding to the same bias are marked with similar margins: empty margins for modula impedance, filled for the impedance of the parallel resistance and capacitance)
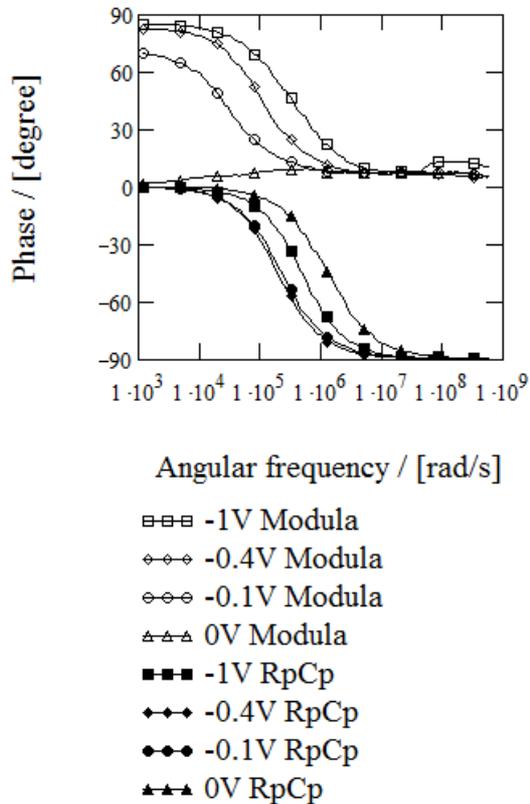
Fig. 3.5.6.5. Comparison of phases of the impedance of the connection where the resistance and the capacitance are in parallel, and that of the modula impedance. (responses corresponding to the same bias are marked with similar margins: empty margins for modula phase, filled for the phase of the parallel resistance and capacitance)

Most clearly can the modula impedance and the impedance of the parallel resistance and capacitance compared if the Bode plots of magnitude (Fig. 3.5.6.4) and phase (Fig. 3.5.6.5) are used. In both plots there is seen that curves of the compared circuit elements are very similar. This may be an indication that these transforms are only formal and do not reflect real processes in the studied structure. Exceptions in both magnitude and phase in this sense are the curves corresponding to the -0.1 V and 0 V.

There is seen that the character of compared curves becomes different and behavior of these is independent of each other. This may be a supporting observation that in this range the calculations proposed may reflect some real processes that are subtracted adequately.

91

This is evident that the question of subtraction of the certain CPE into resistance or capacitance and modula impedance must be studied further with greater effort.

For doing this there are proposed basic formulas for further investigation in Appendix A2.

3.5.7. PREDICTION OF THE SEMICONDUCTOR TYPE AND CALCULATION OF CHARGE CARRIERS PROFILES

For predicting a barrier in the structure of glass/ITO/CuIn$_3$Se$_5$/graphite, the conductivity type of the CuIn$_3$Se$_5$ film was predicted with the potentiodynamic termoprobe test and the polarity of the diode of glass/ITO/CuIn$_3$Se$_5$/graphite was found out. The test with termoprobe revealed that the conductivity of this material is of p-type. Study of the polarity showed that if the positive electrode was connected to the graphite, the diode opens when the positive bias is applied. From the simple band diagram analysis these two observations give a ground to the conclusion that there is a junction between ITO and CuIn$_3$Se$_5$. As the ITO is of metallic like contact an n$^+$p type or a Schottky-type of junction is expected to be present.
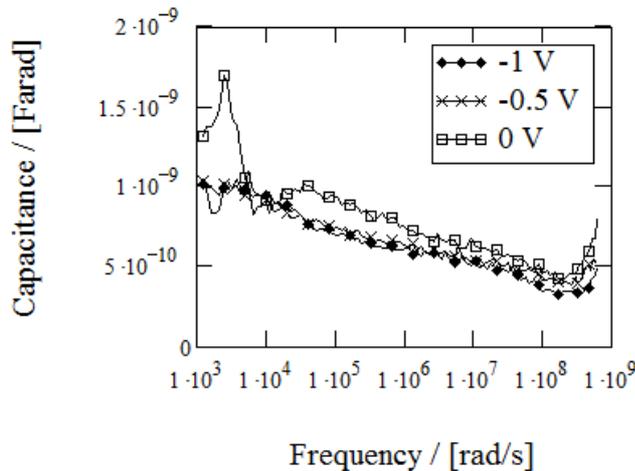
Fig. 3.5.7.1. Frequency dependences of the depletion layer capacitance at different reverse biases

On Fig. 3.5.7.1 there are represented results of the depletion capacitance calculations according to the Eq. 1.6.20. According to the calculations of the parameter influence, the frequency range where the capacitance has a significant influence is from 10^3 rad/s to 10^8 rad/s. So the feature of increasing capacitance at frequencies higher than 10^8 rad/s is not sound. In this range of frequencies the capacitance changes about 2 to 3 times. This is obviously a common feature for

92

deep level ionization that is dependent on the frequency as the time of relaxation depends on the deep level energy value and becomes longer as the energy level is deeper. In these curves there is not probably any range of frequency there the capacitance has a constant value. This obviously adds difficulty to the choice of the frequency suitable for calculations of charge carrier's profiles. In this work the frequencies around 10 Mrad/s were used. In this range the frequency dependence is weaker and it may be assumed that the response is caused already only by shallow level defects that cause the prevailing majority carriers concentrations.
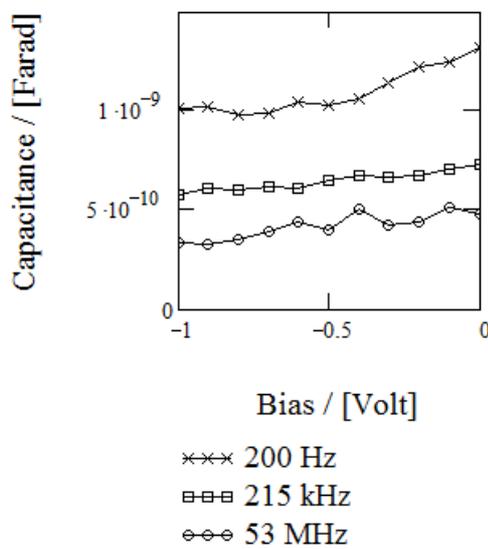
Fig. 3.5.7.2. *C-V* **curves of the glass/ITO/CuIn$_3$Se$_5$/graphite structure measured at reverse biases and at different frequencies of the ac signal**

On Fig. 3.5.7.2 there are represented the results of *C-V* measurements according to the calculations with Eq. 1.6.20. At higher frequencies the capacitance values decrease showing that a smaller amount of the charge is extracted during one cycle of the excitation signal. The change of capacitance value reflects the deep level defects concentration values that can be roughly estimated comparing density profiles calculated for different frequencies. The slow decrease of capacitance values as the reverse bias increases is a common feature of depletion layer that expands at these biases.
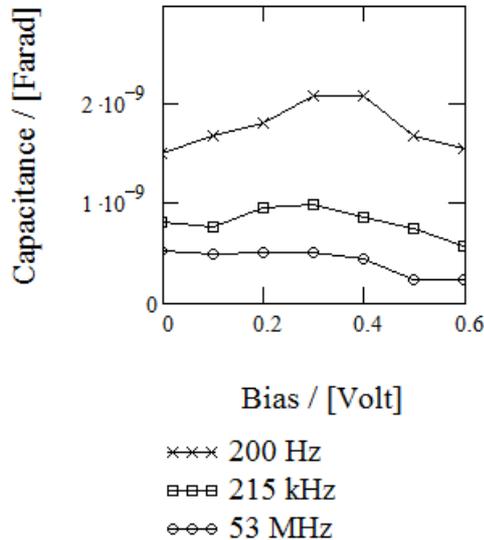
Fig. 3.5.7.2a. *C-V* **curves of the glass/ITO/CuIn$_3$Se$_5$/graphite structure measured at forward biases and at different frequencies of the ac signal**

On Fig. 3.5.7.2a there are represented *C-V* curves that are calculated for forward biases. Majority carriers profiling is usually realized using the data of the reverse side. This is because usually this method is applied in the case of thicker structures. These structures have thicknesses 1 μm and more. And the profiling depth is big enough to examine the material in quite detail. On the other hand, at forward potentials, the minority carrier's injection occurs that starts to affect the depletion layer and finally forms up an accumulation layer that phenomena are beyond the simple depletion layer model that is the basis of calculations here.

Still at lower forward potentials the injection is not observed. On the graph there is seen that there is a maximum of the capacitance. If there was an injection the chemical capacitance would have appeared and the corresponding increase of the capacitance value of the order or two was present.

C-V curves obtained at frequencies about 1 to 10 MHz were chosen for the calculation of shallow level defects concentrations as a profile of the material depth. For that reason the appropriate data (Fig. 3.5.7.2 as an example) was smoothed with a suitable algorithm provided by the Mathcad 13 built in functions. The Gaussian kernel with a bandwidth b (here about 0.25 V) (algorithm denoted as ksmooth which uses the Nadaraya-Watson kernel regression) was found to be most suitable because this allowed monotonously decreasing capacitance values. This is needed to avoid mess in the coordinate calculations because equal values of capacitances at different voltages give the same material depth values but different values of concentrations.

The smoothed data was then approximated with cubic spline functions to obtain a data fit suitable for differentiation.
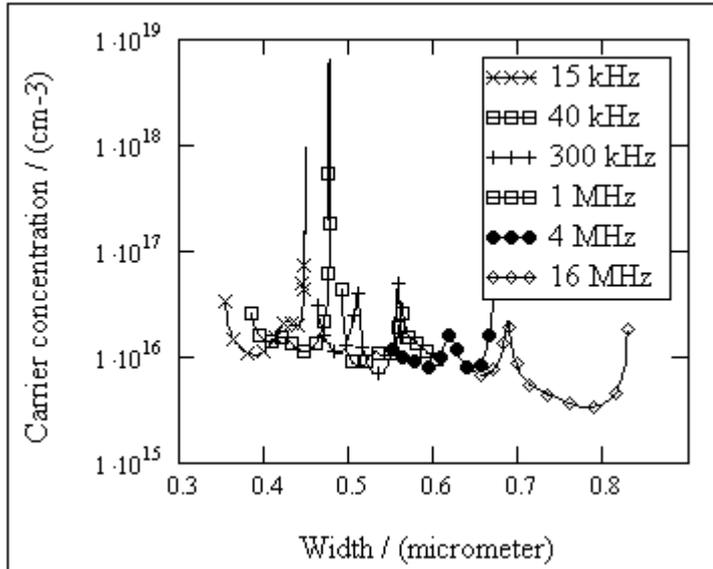
Fig. 3.5.7.3. Carrier concentration profiles of the glass/ITO/CuIn$_3$Se$_5$/graphite structure calculated at reverse biases and at different frequencies of the ac signal

Fig. 3.5.7.3 reports the results for the charge carrier profile calculations where the initial point of the depth coordinate is expected to situate on the interface of the ITO and CuIn$_3$Se$_5$ according to the predictions of the conductivity type and the polarity of the structure. As the measured *C-V* curves are frequency dependent (Fig. 3.5.7.2) it is expected that the results of the profiling calculations are frequency dependent as well. Most evident is that the calculated position of the depletion edge does largely depend on measurement frequency. Still this is caused by the ionizations inside the depletion region and not only at the edge of the depletion layer. The values of concentration also decrease as the frequency increases, pointing that the deep level states do not respond at higher frequencies. Roughly it can be concluded that the concentration of deeper levels are of the same order as the shallow level concentrations predicted more likely at the edge of the depletion layer. On the other hand this is opposite to the results which were found in the case of the newly HVE deposited CuIn$_3$Se$_5$ film (Fig. 3.4.10) where there was observed increase of the carrier concentration if the measurement frequency increased. These earlier calculations used then a simple RC parallel circuit results for the capacitance calculations instead of circuit consisting of general CPE elements. Still this comparison is not quite correct because the objects are physically different.

95
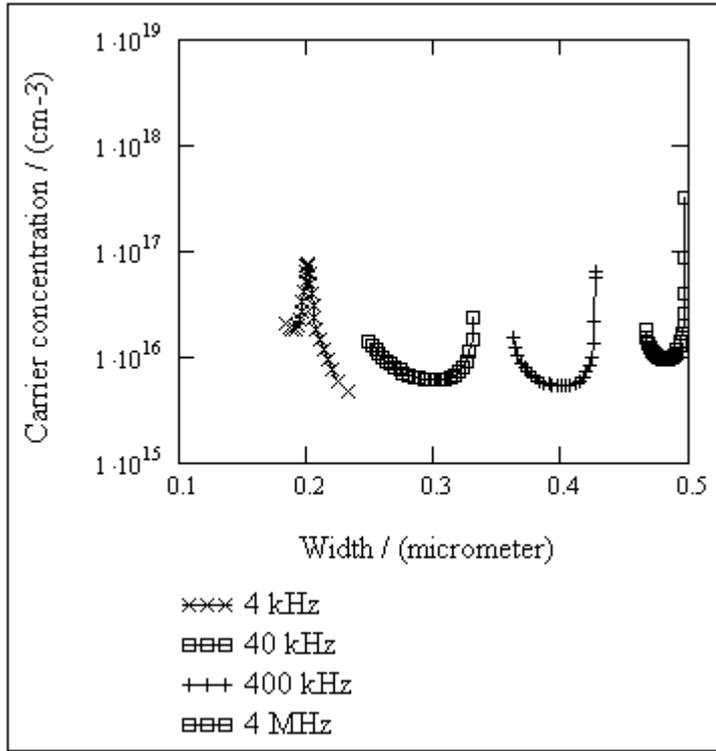
Fig. 3.5.7.3a. Carrier concentration profiles of the glass/ITO/CuIn₃Se₅/graphite structure calculated at forward biases and at different frequencies of the ac signal

On the Fig. 3.5.7.3a there are reported results of the carrier profiles calculated at forward biases. Here the order of the concentration value is the same as reported on Fig. 3.5.7.3. As the forward potential range is significantly smaller (0.3 V) than at the reverse potential range (1 V), there is also a smaller profiling range available. As at reverse potentials, sharp changes in concentration values may not be real and are caused by the properties of calculation method. Also the smoothing conditions influence the shape of the profile a lot.

Unfortunately there is no other sound criterion for choosing an appropriate measurement frequency than the SEM micrograph (Fig. 3.3.2) of the cross-section of the same structure under discussion. From there it is possible to estimate the largest physically possible value for the depletion layer width and to use this as the restriction for the highest possible value that can be calculated while using Eq. 1.8.2.

The value of the maximum width obtained from Fig. 3.3.2 corresponds to the maximum value calculated using Eq. 1.8.2 if the frequency is 4 MHz and the reverse bias is -1 V. This is not possible to predict exactly the right frequency to be used for the calculations because in these measurements the highest reverse bias

96

was chosen -1 V. This is possible that capacitance decreases slightly even further if the voltage becomes less than -1 V.

The sharp peaks on the Fig. 3.5.7.3 are obviously artifacts caused by the specific form of the Eq. 1.8.1 that has a derivative of differential capacitance in denominator. This means that an average value of concentration can be estimated and no particular information about the distribution of the shallow defects inside the material. On the Fig. 3.5.7.3, the results obtained for frequency of 4 MHz are designated with filled circles. An average concentration of shallow defects is $1\cdot10^{16}$ cm^{-3}.

3.5.8. ESTIMATION OF THE MOBILITY OF MAJORITY CARRIERS
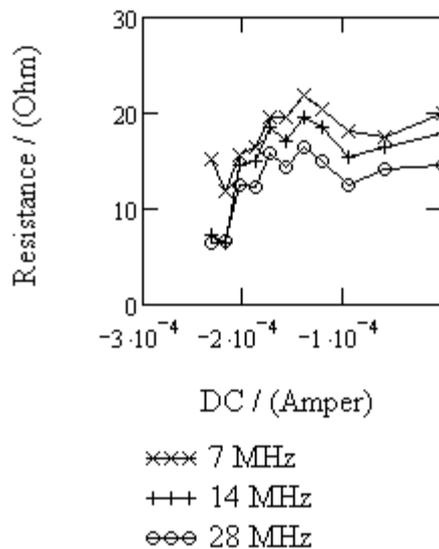
Fig. 3.5.8.1. Differential series resistance dependences on reverse dc at different frequencies

On Fig. 3.5.8.1 there are reported serial resistance dependences on reverse dc calculated from the equivalent circuit parameter CPE-Rs using Eq. 1.7.1.14 and Eq. 1.7.1.15. From there it is seen that the resistance value decreases as the reverse current increases. This is an expected behavior that would be observed if the base area of the structure is decreasing while the depletion region expands. On the other hand the accuracy cannot be expected to be high. Comparing these values with the data on Fig. 3.5.2.5 it turns out that the influence percentage of the series resistance value in this range is about 0.1% of the impedance modulus value. The influence in

97

phase is somewhat more significant – about 1 to 10%. At the same time the error percentage of the impedance measurement device used is 0.5%.

These data were smoothed similarly as in the case of *C-V* data and then integrated according to Eq. 1.9.2 and 1.9.2a using spline functions of Mathcad13.

Depletion width / [micrometer]

⨯⨯⨯ Eq 41
◇◇◇ Eq 41a
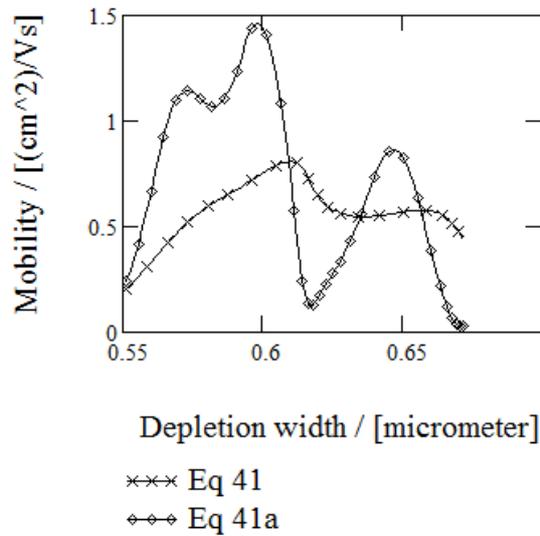
Fig. 3.5.8.2. Estimation of the mobility of holes in the structure of glass/ITO/HVE CuIn₃Se₅ according to the measurements at reverse bias

On the Fig. 3.5.8.2 there are reported results for the calculation of mobility of holes according to the Eq. 1.9.3 and 1.9.4. Estimation of ΔR for the materials base gives a value of a resistivity about 30 Ohm·m.

As the results shown here depend largely on smoothing parameters, the frequencies used for calculation of both the carrier concentration profiles and the series resistances, as well as the error range of the measurement device is probably exceeded, this means that these values may be highly speculative and mostly only estimating. This may be that the base region is too small for achieving more reliable results.
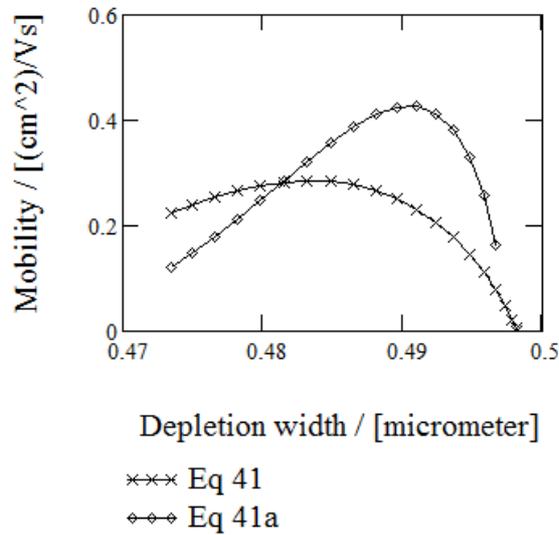
Fig. 3.5.8.2a. Estimation of the mobility of holes in the structure of glass/ITO/CuIn$_3$Se$_5$ according to the measurements at forward bias

On Fig. 3.5.8.2a there are represented results of the mobility calculations according to the data measured at forward biases. According to the parameter influence analysis the series resistance is most influential in the frequency range about 100 Hz to 1 kHz. At the same time the accuracy of predicting the resistivity value, is lower than in the case of the reverse conditions.

Still quite similar value of the mobility can be obtained, but this must be treated as an estimation, and not a precise profile of mobility. The approximate precision is about 1 cm^2/Vs.

CONCLUSIONS

1)   It was found, that used PLD and HVE techniques are appropriate for the $CuIn_3Se_5$ photoabsorber deposition. The PLD deposited and annealed layers demonstrate dense polycrystalline structure of chalcopyrite with an average grains size of 50-200 nm, exhibit photosensitivity and n-type of conductivity. $CuIn_3Se_5$ layers prepared by HVE technique from a polycrystalline stoichiometric precursor had a non-uniform composition in the cross-section. After annealing in argon homogenous polycrystalline chalcopyrite $CuIn_3Se_5$ layers with the crystal sizes of 200 nm were formed. The annealed HVE layers exhibit photosensitivity and p-type of conductivity.

2)   Diode structures based on $CuIn_3Se_5$ photoabsorber layers were prepared for the IS measurements: organic photoabsorber ZnPc gives stable diode contact layer to PLD $CuIn_3Se_5$ layers and photosensitive diode structures glass/ITO/ HVE $CuIn_3Se_5$ can be prepared using the graphite ohmic contacts.

3)   Method of the IS modeling for the structures based on polycrystalline films of $CuIn_3Se_5$ was developed and consists of three steps:

    i)   Determination of appropriate equivalent circuit for the entire measurement frequency range.

    ii)   Shrinking of the modeling range of frequencies to the minimum value and using the sliding modeling mode so that all parameters of the circuit are found as functions of the measurement frequency.

    iii)   The conversion of CPE parameters into the ideal resistive, capacitive and inductive parameters using the idea that any CPE can be transformed into parallel or series configuration of complementary CPE.

4)   It was shown that structures of glass/ITO/PLD $CuIn_3Se_5$/ZnPc/graphite can be considered as two barrier networks consisting of two parallel RC connections in series, where R and C are ideal resistance and ideal capacitance. Structures of glass/ITO/HVE $CuIn_3Se_5$/graphite could be considered as similar networks, where ordinary resistive, capacitive and inductive elements are replaced with resistive-like, capacitance-like and inductive-like constant phase elements. Equivalent circuits consisting of general CPE elements were found mathematically more appropriate for the description of impedance behavior of the structures based on $CuIn_3Se_5$ layers.

5)   The best match of the calculated and experimental values of the differential resistance was observed at small forward potentials in the range of 0 to 0.3 V. Also the match at small reverse potentials (0 to -0.1 V) is satisfactory.

6)   As a result of this doctoral thesis modeling method of IS data was developed. The method provides several advantages and allows:

    i)   reduction of the modeling error in the whole frequency region

    ii)   as a result of the analysis of CPE elements to make available the real physical capacitive and resistive parameters

    iii)   observation of frequency behavior of all network parameters

iv) elimination of the so-called negative capacitance problem usual for polycrystalline structures at zero and reverse bias voltages at lower frequency values of the ac signal.

7) Our results show that the concentration of the shallow level defects in the layers of deposited $CuIn_3Se_5$ depends on the deposition method. PLD samples have a majority charge carriers concentration in the range of 1×10^{14}–1×10^{15}cm^{-3}. Freshly deposited HVE samples have a majority charge carriers concentration in the range of 1×10^{16}–1×10^{17}cm^{-3}. Aged HVE deposited samples have a majority charge carriers concentration in the range of 1×10^{16}–2×10^{16}cm^{-3}. The mobility of the charge carriers of the aged HVE deposited samples was determined to be approximately 0.5 cm^2/Vs.

8) It was shown that proposed method of IS measurement and following modeling can be applied to determination of main electro-physical parameters of deposited $CuIn_3Se_5$ layers. This gives a possibility of using this technique for preparing of photo-absorber layers with predictable properties appropriate for the solar cell applications. On the other hand, further investigation is needed for the development of the analysis of the CPE content. This allows improving the basis for the determination of parameters of prepared structures.

ABSTRACT

In this doctoral thesis the preparation of $CuIn_3Se_5$ photoabsorber layers by using the pulsed laser deposition (PLD) and high vacuum evaporation (HVE) techniques was studied and the electrical properties of prepared layers were investigated with the method of impedance spectroscopy (IS).

As the first type of samples the glass/ITO/PLD $CuIn_3Se_5$ structures prepared in the State University of Saint-Petersburg, Russia, were investigated and used to obtain the hybrid diode structures with the zinc phtalocyanine (ZnPc) deposited by the HVE method in our Lab forming an hybrid structure of glass/ITO/PLD $CuIn_3Se_5$/ZnPc. As the second type of samples the structures of the glass/ITO/$CuIn_3Se_5$ were deposited by the HVE method in our Lab. After the HVE deposition of $CuIn_3Se_5$ the structures were annealed in argon atmosphere and graphite adhesive suspension was applied for preparation of the electric contacts. Both materials of $CuIn_3Se_5$ obtained by the PLD and HVE techniques were studied with the Raman spectroscopy, XRD and EDS for determination of the elemental and phase composition.

SEM micrographs and the results of EDS analysis showed that the films obtained by the PLD method demonstrate the uniform morphology and elemental composition of the $CuIn_3Se_5$ in cross section. The as-deposited films prepared by HVE consisted of two main layers with different elemental composition, which

averaged during the annealing process and formed a single layer of the $CuIn_3Se_5$ stoichiometry. $CuIn_3Se_5$ films obtained by PLD and HVE had different morphology and type of conductivity. Films deposited by the PLD method and annealed in vacuum exhibited n-type of conductivity while the films deposited by the HVE method and annealed in argon exhibited p-type of conductivity. *I-V* measurements showed that both types of $CuIn_3Se_5$ films are photosensitive under white light illumination. XRD and Raman spectroscopy showed that both methods of deposition give layers of the material consisting mainly of the $CuIn_3Se_5$ chalcopyrite phase. Results of the study show that used methods of deposition are appropriate for the preparation of $CuIn_3Se_5$ photoabsorber layers depending on the preference of the type of conductivity.

For the analysis of IS measurements the method of electrical circuit analysis was used that was complemented with additional aspects. Besides the modeling of the entire frequency range with a single set of circuit parameters, the circuit modeling was accomplished in the sliding mode where the narrow range of frequency (about 1 decade of frequencies) was used to find parameters of the circuit, allowing the finding of the dependences of parameters on frequency. Constant phase elements (CPE) were used as circuit elements. For the analysis of the content of the CPE elements of the modeling circuit there were proposed additional equations in this doctoral thesis that enabled the analysis of the problem with the use of methods of mathematical analysis and allowed the test of the results with the data obtained by the experimental *I-V* measurements. It was shown that while applying special conditions to the parameters that can be concluded from the mathematical analysis, there can be observed a good match between calculations and experiment. The analysis proposed in the thesis is a simplified case. For the analysis of the general situation the appropriate equations were reported in the Appendix.

IS calculations of the majority carriers' concentrations showed that the concentration depends on the preparation method of the samples. PLD samples had a concentration in the range of $1 \times 10^{14} – 1 \times 10^{15} cm^{-3}$. Freshly HVE deposited samples had a concentration in the range of $1 \times 10^{16} – 1 \times 10^{17} cm^{-3}$. Aged HVE deposited samples, held in the laboratory ambient during six months, had a concentration in the range of $1 \times 10^{16} – 2 \times 10^{16} cm^{-3}$. The mobility of the majority charge carriers of the aged HVE deposited samples was approximately 0.5 cm^2/Vs. It was found that the proposed method of IS calculations can be applied to determine also other electro-physical parameters of $CuIn_3Se_5$ photoabsorber layers that are important for the solar cell applications.

KOKKUVÕTE

Hübriidsete CuIn$_3$Se$_5$ fotoabsorberstruktuuride valmistamine ja impedantsispektroskoopia

Doktoritöö käigus valmistati, kasutades laserablatsiooni ja vaakumaurustamine meetodeid, CuIn$_3$Se$_5$ fotoabsorberkilesid, uuriti nende struktuurseid omadusi ning määrati neist kiledest valmistatud erinevate hübriidsete dioodstruktuuride elektrilisi omadusi, kasutades impedantsispektroskoopiat (IS).

Esimest tüüpi objektidena uuriti Venemaa Peterburi Riiklikus Ülikoolis laserablatsiooni meetodil sadestatud CuIn$_3$Se$_5$ kilesid, millele oli loodud vaakumaurustuse meetodil tsinkftaaltsüaniinist (ZnPc) kontakt, mille tulemusel saadi dioodstruktuur hübriidne klaas/ITO/CuIn$_3$Se$_5$/ZnPc. Teist tüüpi objektides kasutati CuIn$_3$Se$_5$ kilede valmistamiseks vaakumaurustamist. Materjal sadestati klaas/ITO alusele ja lõõmutati argoonis, mille tulemusel saadi struktuur klaas/ITO/CuIn$_3$Se$_5$. Elektriliste kontaktidena kasutati grafiitpastat. Nii laserablatsiooni meetodil kui ka vaakumaurustamise meetodil saadud kilesid uuriti materjalide stöhhiomeetria ja faasiliste omaduste määramiseks SEM, Ramanspektromeetria, röntgendifraktsioonanalüüsi ja elektronide emissioonienergiate dispersiooni spektroskoopia (EEDS) meetoditel.

SEM mikrofotode ja EEDS elementanalüüsi näitas, et vaakumaurustamisel tekib kahekihiline erineva morfoloogia ja elementide stöhhiomeetrilise koostisega kilestruktuur, mis lõõmutamise tulemusel ühtlustub nii struktuurilt kui ka elementkoostiselt. Laserablatsiooni meetodil saadud kilede uurimisel leiti, et need on sadestamisjärgselt ristlõikes ühesuguse stöhhiomeetrilise koostise ja morfoloogiaga. Laserablatsiooni meetodil ja vaakumaurustamise meetodil saadud CuIn$_3$Se$_5$ kilede juhtivustüüp ja pinnamorfoloogia olid erinevad. Laserablatsiooni meetodil saadud kiled olid elektronjuhtivusega, ja vaakumaurustamise meetodil saadud kiled olid aukjuhtivusega. *IV* mõõtmiste abil selgitati, et mõlemal meetodil saadud kiled olid valgustundlikud ning neis tekib valguse mõjul märgatav fotojuhtivus. Röntgendifraktsioonanalüüsi ja Ramanspektroskoopia andmetel oli mõlemal meetodil sadestatud kiledes domineeriv CuIn$_3$Se$_5$ faas. Tulemused näitasid, et mõlemad töös kasutatud sadestusmeetodid sobivad CuIn$_3$Se$_5$ absorberkilede valmistamiseks sõltuvalt eelistusest juhtivustüübile.

IS tulemuste analüüsimisel kasutati tavapäraseid modelleerimismeetodeid (IS andmete modelleerimine elektriliste aseskeemidega), mida täiendati, kasutades modelleerimisel kitsast (u üks sagedusdekaad) ja nihkuvat sagedusvahemikku. Elektrilise aseskeemi elementidena kasutati konstantse faasinihke elemente, mida analüüsiti parameetriliste võrrandite abil mahtuvuse ja takistuse leidmiseks. Konstantse faasinihke elementide sisu analüüsimiseks esitati selles doktoritöös täiendavad võrrandid, mis võimaldavad probleemi analüüsida matemaatilise analüüsi meetodite abil ning saadud tulemusi testida *IV* mõõtmistel saadud

eksperimentaalsete andmete alusel. Näidati, et parameetriliste võrrandite matemaatilisest analüüsist järelduvate eritingimuste rakendamisel saadakse eksperimendiga kokkulangevaid tulemusi. Töös esitati analüüs lihtsustatud kujul. Probleemi kitsendusteta käsitlemiseks vajalikud võrrandid on esitatud töö lisas.

IS tulemustel põhinevate arvutuste kohaselt sõltub saadud kilede enamuslaengukandjate kontsentratsioon kilede valmistamismeetodist. Laserablatsiooni meetodil saadud kilede korral oli enamuslaengukandjate kontsentratsioon vahemikus 1×10^{14}–1×10^{15}cm^{-3}. Vaakumaurustamise meetodil valmistatud värsketes struktuurides oli enamuslaengukandjate kontsentratsioon vahemikus 1×10^{16}–1×10^{17}cm^{-3}. Struktuurides, mida hoiti kuue kuu vältel avatud laboritingimustes oli enamuslaengukandjate kontsentratsioon vahemikus 1×10^{16}–2×10^{16}cm^{-3}. Samade kilede korral arvutati liikuvus u 0,5 cm^2/Vs. Leiti, et töös esitatud täiendatud metoodika impedantsiandmete analüüsimiseks võimaldab leida ka teisi materjalide elektrofüüsikalisi omadusi, mis on määravad päikeseelementide jaoks sobilike materjalide väljatöötamisel.

REFERENCES

1. Mary D. Archer, Robert Hill, (editors), U. Rau, H.W. Schock (authors) Clean electricity from photovoltaics: Cu(In,Ga)Se$_2$ solar cells, Imperial College Press, 2001.

2. A. Luque, S. Hegedus (editors) W.N. Shafarman, L. Stolt (authors) Handbook of photovoltaic science and engineering: Cu(InGa)Se$_2$ Solar cells, John Wiley & Sons, England 2003.

3. H. Hahn, G. Frank, W. Klingler, A. Meyer, G. Störger, Über einige ternäre Chalkogenide mit Chalkopyritstruktur, Z. Anorg. u. Allg. Chemie 271, 153-170, (1953).

4. S. Wagner, J.L. Shay, P. Migliorato, H. M. Kasper, CuInSe$_2$/CdS heterojunction photovoltaic detectors, Appl. Phys. Lett. 25, 434-435, (1974).

5. L. Kazmerski, F. White, G. Morgan, Appl. Phys. Lett. 29, 268, 269 (1976).

6. R. A. Mickelsen, W.S. Chen High photocurrent polycristalline thin-film CdS/CuInSe$_2$ solar cell, Appl. Phys. Lett. 36, 371-373, (1980).

7. R. A. Mickelsen, W.S. Chen Polycrystalline thin-film CuInSe$_2$ solar cells, Conf. Record 16th. IEEE Photovoltaic Specialists Conf., San Diego, IEEE Press, Piscataway, 781-785, (1982).

8. W. Chen et al., Proc. 19th IEEE Photovoltaic Specialist Conf., 1445–1447 (1987)

9. R. Potter, Sol. Cells 16, 521–527 (1986).

10. J. Hedström et al., Proc 23rd IEEEPhotovoltaic Specialist Conf., 364–371 (1993)

11. A. Gabor et al., Sol. Energy Mater. Sol. Cells 4, 247–260 (1996).

12. K. C. Mitchell, J. Ermer, D. Pier, Single and tandem junction CuInSe$_2$ cell and module technology, Conf. Record 20th. IEEE Photovoltaic Specialists Conf., Las Vegas, IEEE Press, Piscataway, 1384-1389, (1988).

13. M. A. Contreras, B. Egaas, K. Ramanathan, J. Hiltner,A. Swartzlander, F. Hasoon, R. Noufi, Towards 20% efficiency in Cu(In,Ga)Se$_2$ polycristalline solar cells, Prog. Photovoltaic Res. Appl. 7, 311-316, (1999).

14. F. Karg Development and manufacturing of CIS thin film modules, Tech. Digest 11th. Int. Sci. Eng. Conf., Tokyo University of Agriculture and Technology, Tokyo, 627-630 (1999).

15. J. Kessler, M. Bodegard, J. Hedström, L. Stolt, Baseline Cu(In,Ga)Se$_2$ device production: control and significance, Tech. Digest 11th. Int. Sci. Eng. Conf., Tokyo University of Agriculture and Technology, Tokyo, 631-632 (1999).

16. http://www.nrel.gov/news/press/2008/574.html; I. Repins, M. A. Contreras, B. Egaas, C. DeHart, J. Scharf, C. L. Perkins, B. To, R. Noufi, 19.9%-efficient ZnO/CdS/CuInGaSe$_2$ Solar Cell with 81.2% Fill Factor, Prog. Photovolt: Res. Appl. 2008; 16:235−239

17. T. Coutts, J. Meakin (editors), L. Kazmerski, S. Wagner (authors) Current topics in Photovoltaics: Cu-ternary Chalcopyrite Solar Cells, 41-109, Academic Press, London (1985).

18. D. Haneman, Crit. Rev. Solid state Mater. Sci. 14, 377-413 (1988).

19. A. Rockett, R. Birkmire, J. Appl. Phys. 70, R81 – R97 (1991).

20. D. Schmid, M. Ruckh, F. Grunwald, H.W. Schock, Chalcopyrite/defekt chalcoppyrite heterojunctions on the basis of CuInSe$_2$, J. Appl. Phys. 73 (6), 2902-2909, (1992).

21. G. Marin, S.M. Wasim, C. Rincon, G. Sanchez Perez, Ch. Power, A.E. Mora, J. Appl. Phys. 83 (1998) 3364–3366.

22. C. Rincon, S.M. Wasim, G. Marin, A. Rincon, P. Bocaranda, C. Torres, G. Bacquet, G. Sanchez Perez, Mater. Lett. 41 (1999) 222–228.

23. H.Z. Xiao, L.-Chung Yang, A. Rockett, Structural, optical, and electrical properties of epitaxial chalcopyrite CuIn$_3$Se$_5$ films, J. Appl. Phys. 76 (3), 1503-1510, (1994).

24. A. Goetzberger, C. Hebling, H.W. Schock, Photovoltaic materials, history, status and Outlook, Materials Science and Engineering R 40 1–46 (2003).

25. V. Kapur, B. Basol, E. Tseng, Sol. Cells 21, 65–70 (1987).

26. B. Basol, V. Kapur, IEEE Trans. Electron Devices 37, 418–421 (1990).

27. F. Garcia, M. Tomar, Jpn. J. Appl. Phys. 22S, 535–540 (1983).

28. D. Schulz et al., Proc. 27th IEEE Photovoltaic Specialists Conf., 483–486 (1997).

29. J. Kessler, H. Dittrich, F. Grunwald, H. Schock, Proc. 10th Euro. Conf. Photovoltaic Solar Energy Conversion, 879–882 (1991).

30. H. Oumous et al., Proc. 9th Euro.Conf. Photovoltaic Solar Energy Conversion, 153–156 (1992).

31. F. Karg et al., Proc. 23rd IEEE Photovoltaic Specialists Conf., 441–446 (1993)

32. G. Mooney et al., Appl. Phys. Lett. 58, 2678–2680 (1991).

33. H. M. Smith, A. F. Turner, Vacuum deposited thin films using ruby laser, Appl. Opt. 4, 147-148.

34. D. B. Chrisey, G. K. Hubler, Pulsed Laser Deposition of Thin Films, John Wiley & Sons, Inc 1994.

35. K. K. Schuergraf, Handbook of thin-film deposition processes and techniques: Principles, Methods, Equipment and Applications, Noyes Publications, 1988.

36. P. Malar, S.Kasiviswanathan, Characterization of stepwise flash evaporated $CuIn_3Se_5$ films, Solar Energy Materials & Solar Cells 85 521-533 (2005).

37. C. Ricon, S.M. Wasim, G. Marin, A. Ricon, P. Pocaranda, C. Torres, G. Bacquet, G. Sanchez Perez, Optical characterization of bulk $CuIn_3Se_5$, Material Letters 41 (1999) 222-228.

38. R. Marquez, C. Rincon, Defects physics of the ordered defect compound $CuIn_3Se_5$, Solar Energy Materials & Solar Cells 71 (2002) 19-26.

39. K. Orgassa, U. Rau, Q. Nguyen, H.W. Schock, J. H. Werner, Role of the CdS Buffer Layer as an Active Optical Element in $Cu(In,Ga)Se_2$ Thin-Film Solar Cells, Prog. Photovolt: Res. Appl. 2002; 10:457–463.

40. E. Barsoukov and J.R. Macdonald (Eds.) Impedance spectroscopy Wiley-Interscience, Chichester, 2005.

41. A.F. Yaremchuk, New interpretation of C-V measurements for determining the concentration profile in a semiconductor, Appl. Phys. A 73, 503-509 (2001).

42. A.F. Yaremchuk, A contribution to the theory of the C-V technique for the evaluation of carrier-concentration profiles in semiconductors, Appl. Phys. A 80, 881-883 (2005).

43. K.P. Homewood, R.P. Benyon, Frequency-resolved capacitance spectroscopy – a new approach to measuring deep levels in semiconductors, J. Phys. E: Instrum. 21 (1988) 1022-1024.

44. M. Burgelman, P. Nollet, Admittance spectroscopy of thin film solar cells, Solid State Ionics 176 (2005) 2171-2175.

45. T. Walter, R. Herberholz, C. Müller, H.W. Schock, Determination of defect distributions from admittance measurements and application to Cu(In,Ga)Se2 based heterojunctions, J. Appl. Phys. 80 (8) (1996) 4411-4420.

46. R. Herberholz, M. Igalson, H.W. Schock, Distinction between bulk and interface states in CuInSe2/CdS/ZnO by space charge spectroscopy, J. Appl. Phys. 83 (1) 318-325 (1998).

47. J.W. Lee, J.D. Cohen, W.N. Shafarman, The determination of carrier mobilities in CIGS photovoltaic devices using high-frequency admittance measurements, Thin Solid Films 480-481 (2005) 336-340.

48. M. Burgelman, M. Topic (Eds.) Proceedings of NUMOS, International Workshop on Numerical Modelling of Thin Film Solar Cells, Gent, Belgium 2007.

49. H. Schichlein, A.C. Müller, M. Voigts, A. Krügel, E. Ivers-Tiffee, Deconvolution of electrochemical impedance spectra for the identification of electrode reaction mechanisms in solid oxide fuel cells, J. Appl. Electrochem. 32: 875-882, (2002).

50. J.-P. Diard, B. Le Gorrec, C. Montella, Handbook Of Electrochemical Impedance Spectroscopy: Diffusion impedances, Hosted by Bio-Logic @ www.bio-logic.info, March 12, 2008

51. J.-P. Diard, B. Le Gorrec, C. Montella, Handbook Of Electrochemical Impedance Spectroscopy: Electrical circuits containing CPE-s, Hosted by Bio-Logic @ www.bio-logic.info, September 6, 2007.

52. F. Berthier, J. -P. Diard, R. Michel, Distinguishability of equivalent circuits containing CPEs: Part I. Theoretical part, J. of Electroanal. Chem. 510, Issues 1-2, 7 September 2001, Pages 1-11.

53. P. Zoltowski, On the electrical capacitance of interfaces exhibiting constant phase element behaviour, J. Electroanal. Chem. 443 (1998), p. 149-154.

54. A. Sadkowski, On the ideal polarisability of electrodes displaying cpe-type capacitance dispersion, J. Electroanal. Chem. 481 (2000), p. 222-226

55. G. Láng and K.E. Heusler Comments on the ideal polarisability of electrodes displaying cpe-type capacitance dispersion, J. Electroanal. Chem. 481 (2000), p. 227-229

56. P. Ekdunge, K. Jüttner, G. Kreysa, T. Kessler, M. Ebert and W.J. Lorenz Electrochemical Impedance Study on the Kinetics of Hydrogen Evolution at Amorphous Metals in Alkaline Solution, J. Electrochem. Soc. 138 (1991), p. 2660-2668

57. M. Sluyters-Rehbach. Pure Appl. Chem. 66 (1994), p. 11831

58. J.H. Ely, T.R Ohno, T.E. Furtak, A.J. Nelson Thin Solid Films 371 2000. 36-39

59. G. Morell, R.S.Katiyar, S.Z. Weisz, T.Walter, H. Schock, I.Balberg Appl. Phys. Lett. 69 (7), 1996,987-989.

60. O.A. Balitskii, V.P. Savchyn, V.O. Yukhymchuk Semicond. Sci. Technol. 17 (2002) L1–L4

61. I. Mora-Sero, Y. Luo, G. Garcia-Belmonte, J. Bisquert, D. Munoz, C. Voz, J. Puigdollers, R. Alcubilla, Solar Energy Materials & Solar Cells 92 (2008) 505–509.

62. G. Garcia-Belmonte, A. Munar, E. M. Barea, J. Bisquert, I. Ugarte, R. Pacios, Organic Electronics 9 (2008) 847–851.

63. M. Burgelman, P. Nollet, Solid State Ionics 176 (2005) 2171-2175.

64. S.M. Sze, Semiconductor devices: Physics and Technology, New York (N.Y.):Wiley, c2002, 2nd ed.

65. A.M. Fernandez, P.J. Sebastian, R.N. Bhattacharya, R. Noufi, M.Contreras, A.M. Hermann, Semicon. Sci. Technol., 1996, 11, 964-967.

APPENDIX A1

IS DATA MODELING RESULTS OF THE AGED GLASS/ITO/HVE CUIN$_3$SE$_5$/GRAPHITE STRUCTURE
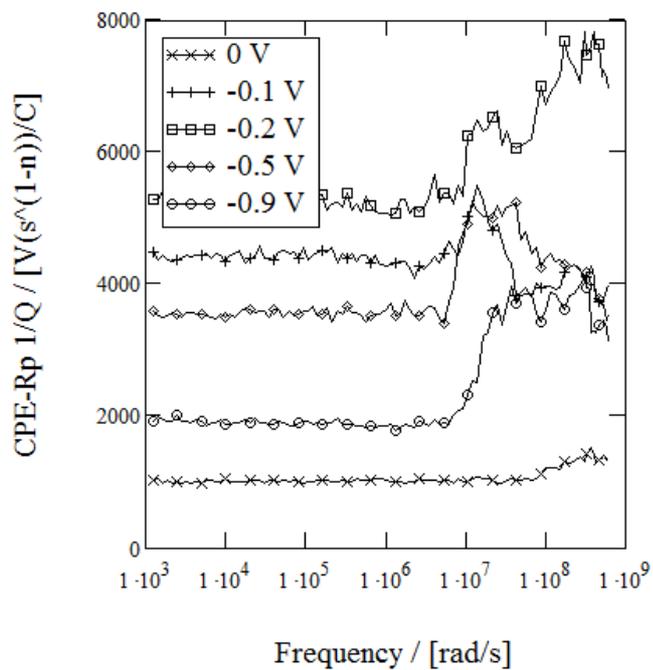
Fig. A1.1. Equivalent circuit (Fig. 3.4.3 in main text) element CPE-Rp parameter 1/*Q* frequency dependence on different applied reverse biases
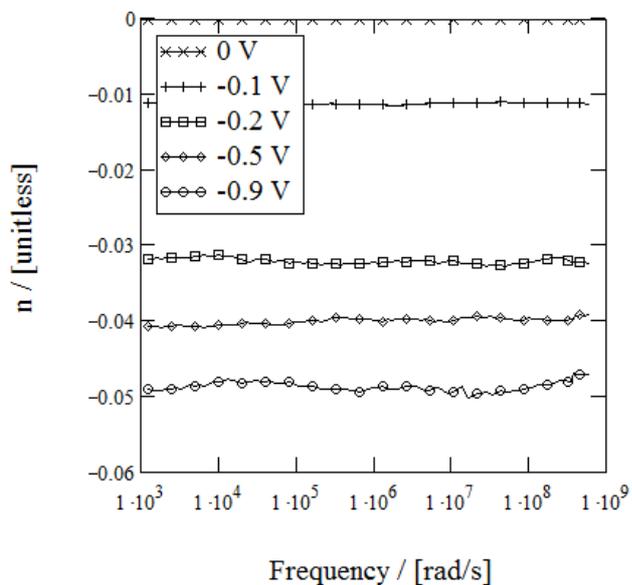
Fig. A1.2. Equivalent circuit (Fig. 3.4.3 in main text) element CPE-Rp parameter *n* frequency dependence on different applied reverse biases
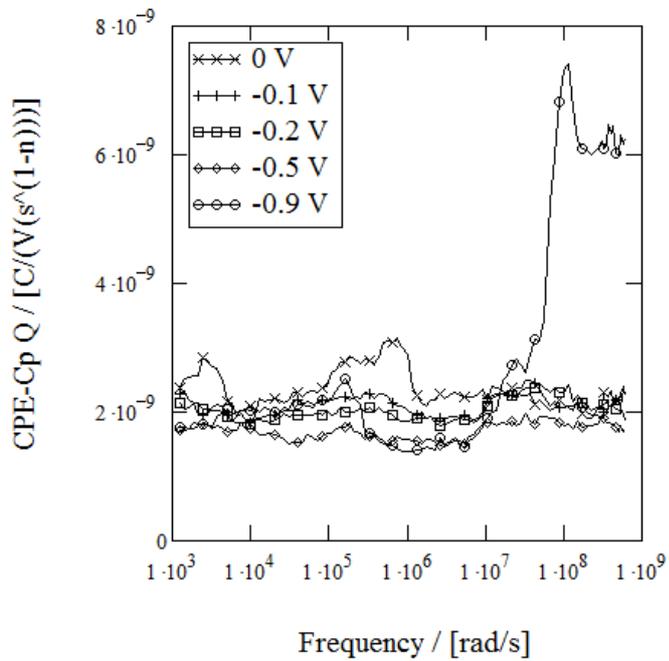
Fig. A1.3. Equivalent circuit (Fig. 3.4.3 in main text) element CPE-Cp parameter *Q* frequency dependence on different applied reverse biases
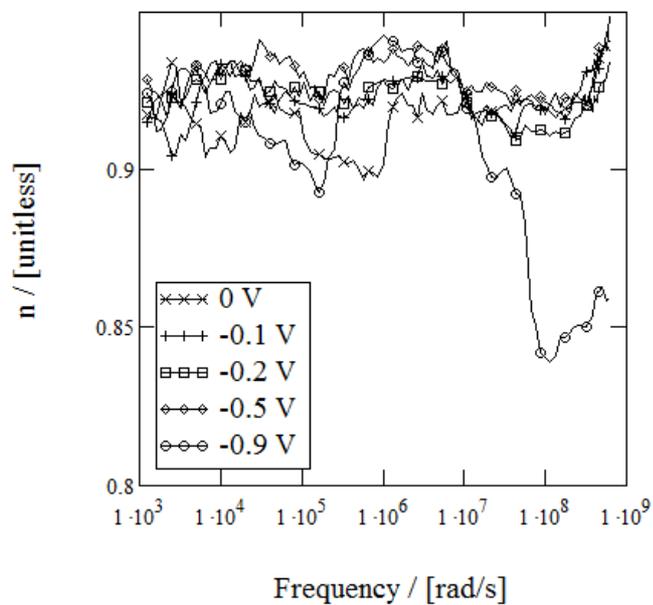
Fig. A1.4. Equivalent circuit (Fig. 3.4.3 in main text) element CPE-Cp parameter *n* frequency dependence on different applied reverse biases

114
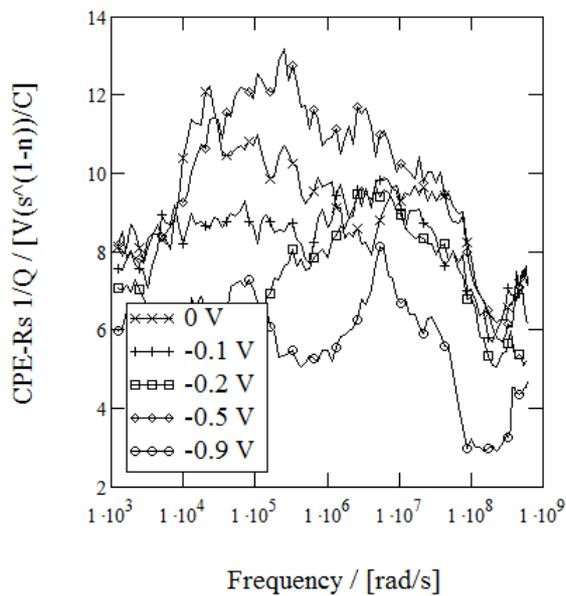
Fig. A1.5. Equivalent circuit (Fig. 3.4.3 in main text) element CPE-Rs parameter 1/*Q* frequency dependence on different applied reverse biases
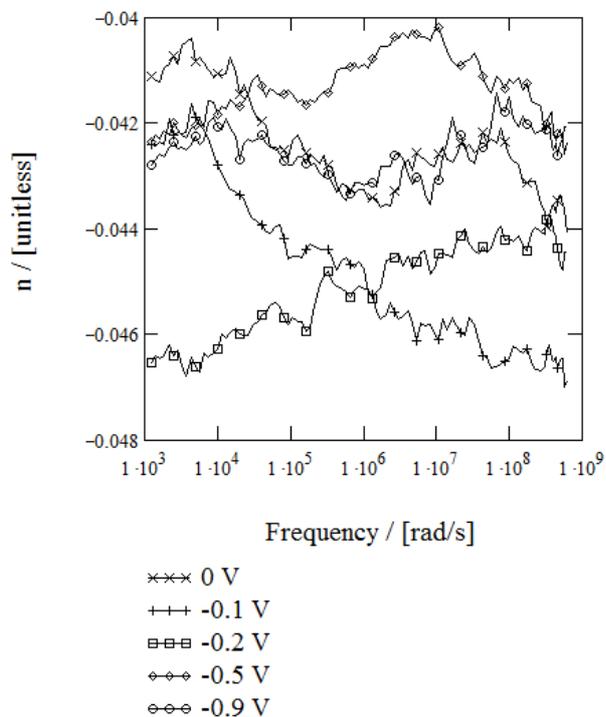
Fig. A1.6. Equivalent circuit (Fig. 3.4.3 in main text) element CPE-Rs parameter *n* frequency dependence on different applied reverse biases
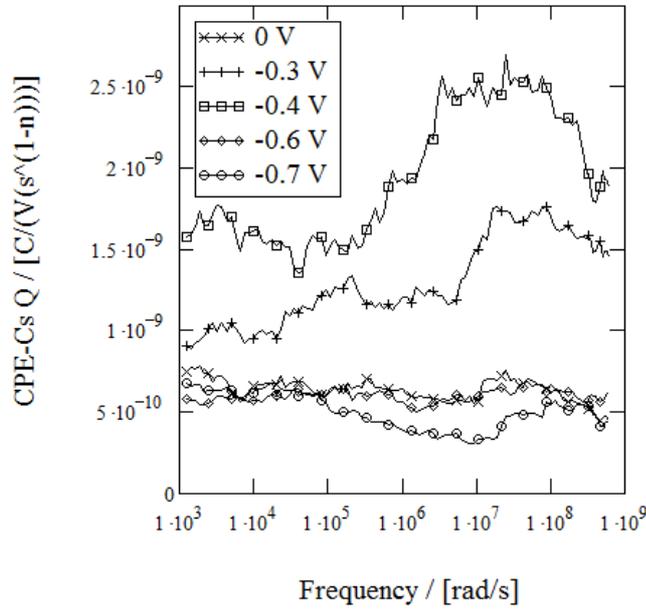
Fig. A1.7. Equivalent circuit (Fig. 3.4.3 in main text) element CPE-Cs parameter Q frequency dependence on different applied reverse biases
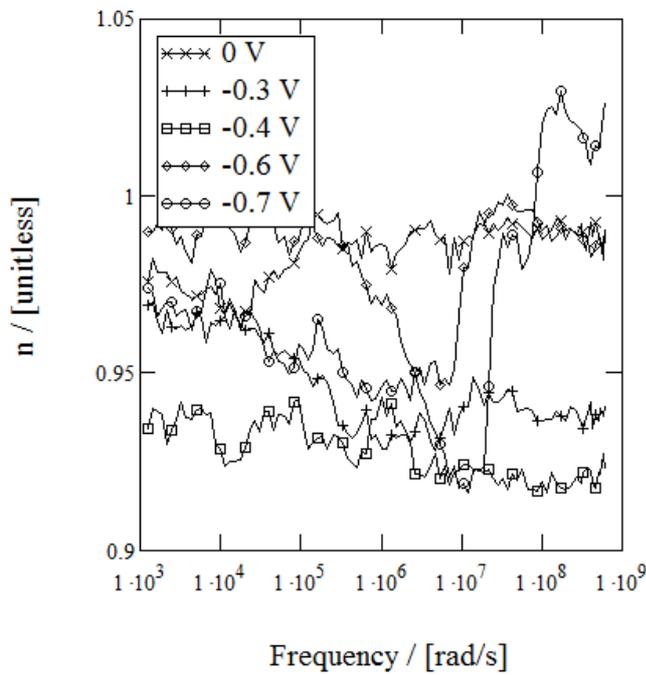
Fig. A1.8. Equivalent circuit (Fig. 3.4.3 in main text) element CPE-Cs parameter n frequency dependence on different applied reverse biases

116
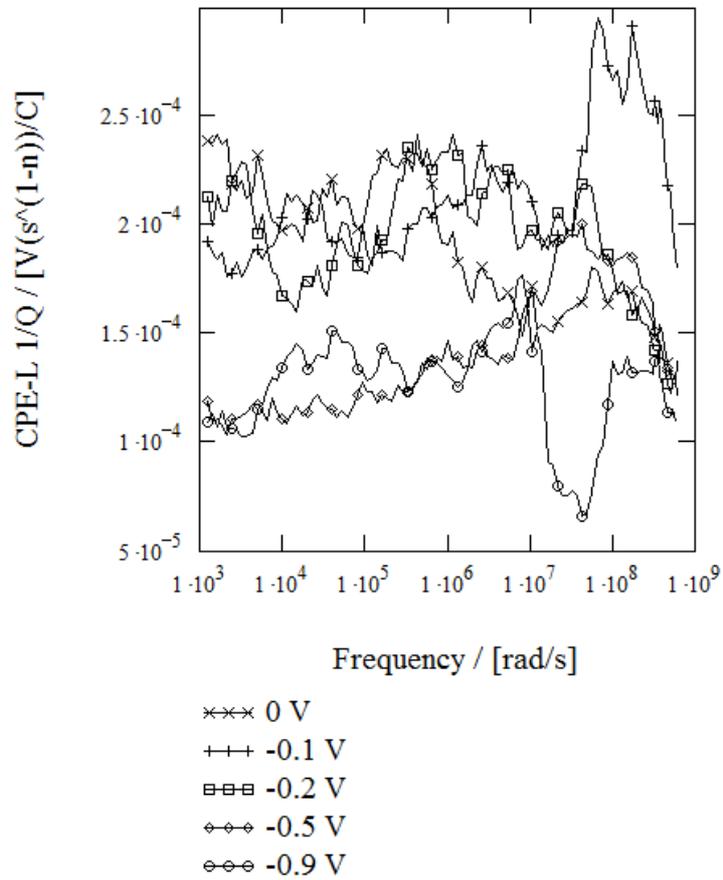
Fig. A1.9. Equivalent circuit (Fig. 3.4.3 in main text) element CPE-Ls parameter 1/Q frequency dependence on different applied reverse biases
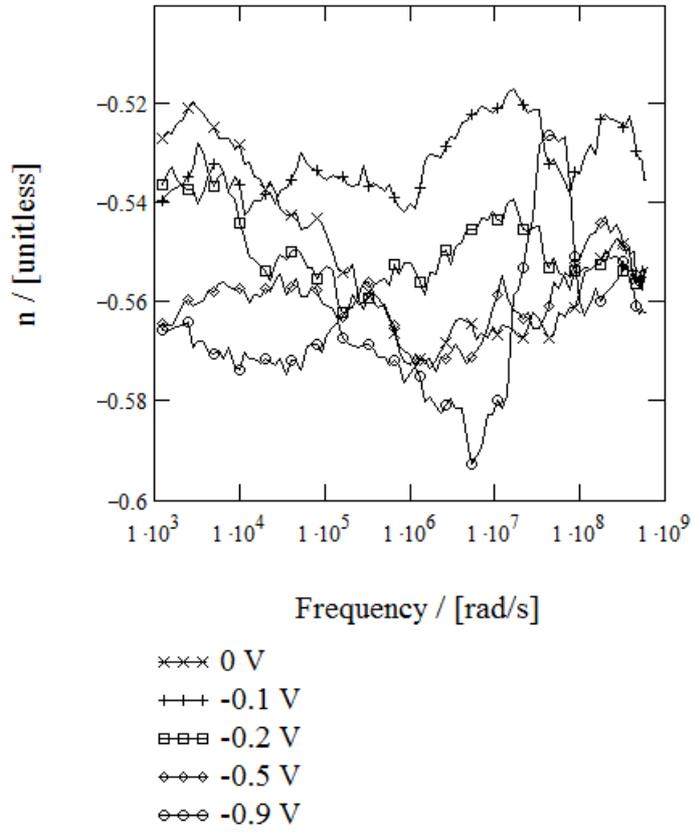
Fig. A1.10. Equivalent circuit (Fig. 3.4.3 in main text) element CPE-Ls parameter *n* frequency dependence on different applied reverse biases

APPENDIX A2

**GENERAL PARAMETRIC TRANSFORMATION FORMULA FOR
CONVERTING A CPE INTO TWO PARALLEL CPE**

On Fig. 1.6.1 there is represented the general idea that any CPE impedance or admittance can be transformed into series (Fig. 1.6.1 a) or parallel (Fig. 1.6.1. b) configuration of two CPE-s. This transformation is invariant and reversible if the exponential parameters (the exponential term of p in Eq. 1.6.1) of the two new CPE-s can be fixed.

If the exponential parameters are not fixed, the transformation is not invariant and possible ways of fixing these exponential parameters must be studied. In case of the transform into parallel connection of CPE-s, the question can be studied if one of these parameters is fixed as $p=1$ and there are possible to use the equation system consisting of Eq. 1.6.6 – 1.6.8.

It may be wrong to assume that one of the exponential parameters of p can be fixed preliminarily and the study of possible values of exponential parameters is more complicated. For such a study there is possible to use an equation system consisting of four equations that arise from principles of the circuit calculation. Here are presented formulas that can be constructed in the case of the transformation then the initial CPE is transformed into parallel connection of two subsequent CPE-s (Fig. 1.6.1 b). In case of the transformation into series connection (Fig. 1.6.1 a) analogous equations, but somewhat different in form, can be constructed.

These equations are:

$$\omega^{-p} \cdot Q^{-1} \cdot \cos\left(\frac{\pi}{2} \cdot p\right) = \blacksquare$$

$$\frac{Q1 \cdot \omega^{n} \cdot \cos\left(\frac{\pi}{2} \cdot n\right) + Q2 \cdot \omega^{t} \cdot \cos\left(\frac{\pi}{2} \cdot t\right)}{\left(Q1 \cdot \omega^{n} \cdot \cos\left(\frac{\pi}{2} \cdot n\right) + Q2 \cdot \omega^{t} \cdot \cos\left(\frac{\pi}{2} \cdot t\right)\right)^{2} + \left(Q1 \cdot \omega^{n} \cdot \sin\left(\frac{\pi}{2} \cdot n\right) + Q2 \cdot \omega^{t} \cdot \sin\left(\frac{\pi}{2} \cdot t\right)\right)^{2}} \quad \text{(A2.1),}$$

$$\omega^{-p} \cdot Q^{-1} \cdot \sin\left(\frac{\pi}{2} \cdot p\right) = \blacksquare$$

$$\frac{Q1 \cdot \omega^{n} \cdot \sin\left(\frac{\pi}{2} \cdot n\right) + Q2 \cdot \omega^{t} \cdot \sin\left(\frac{\pi}{2} \cdot t\right)}{\left(Q1 \cdot \omega^{n} \cdot \cos\left(\frac{\pi}{2} \cdot n\right) + Q2 \cdot \omega^{t} \cdot \cos\left(\frac{\pi}{2} \cdot t\right)\right)^{2} + \left(Q1 \cdot \omega^{n} \cdot \sin\left(\frac{\pi}{2} \cdot n\right) + Q2 \cdot \omega^{t} \cdot \sin\left(\frac{\pi}{2} \cdot t\right)\right)^{2}} \quad \text{(A2.2),}$$

$$E \cdot Q1 \cdot \omega^n = Q2 \cdot \omega^t \qquad \text{(A2.3) and}$$

$$B + n = t \qquad \text{(A2.4)}.$$

In these equations ω is the angular frequency, Q [C/(V·s$^{(1-p)}$)] is the parameter of the initial CPE, p [unitless] is the exponential parameter of the initial CPE, Q_1 [C/(V·s$^{(1-p)}$)] is the parameter of the first CPE after transformation, n [unitless] is the exponential parameter of the first CPE after transformation, Q_2 [C/(V·s$^{(1-p)}$)] is the parameter of the second CPE after transformation, t [unitless] is the exponential parameter of the second CPE after transformation, E [unitless] is the proportionality factor, B [unitless] is the difference of n and t.

Eqs. A2.1 and A2.2 can be rearranged together and can be substituted by equations of

$$s = \frac{Q1 \cdot \omega^n \cdot \sin\left(\frac{\pi}{2} \cdot n\right) + Q2 \cdot \omega^t \cdot \sin\left(\frac{\pi}{2} \cdot t\right)}{Q1 \cdot \omega^n \cdot \cos\left(\frac{\pi}{2} \cdot n\right) + Q2 \cdot \omega^t \cdot \cos\left(\frac{\pi}{2} \cdot t\right)} \qquad \text{(A2.1a) and}$$

$$\frac{\omega^{-2 \cdot n}}{Q^2} = \blacksquare$$

$$\frac{1}{2 \cdot Q1 \cdot \omega^{p+s} \cdot \cos\left(\frac{1}{2} \cdot \pi \cdot p\right) \cdot Q2 \cdot \cos\left(\frac{1}{2} \cdot \pi \cdot s\right) + Q1^2 \cdot \omega^{2 \cdot p} + 2 \cdot Q1 \cdot \omega^{p+s} \cdot \sin\left(\frac{1}{2} \cdot \pi \cdot p\right) \cdot Q2 \cdot \sin\left(\frac{1}{2} \cdot \pi \cdot s\right) + Q2^2 \cdot \omega^{2 \cdot s}}$$

$$\text{(A2.2a)}.$$

The parameter of s is defined with the Eq. 1.6.13 as earlier.

The Eq. A2.1 is the mathematical representation of the equality of the real part of the impedances of the initial CPE and the parallel connection of the two subsequent CPE-s. The Eq. A2.2 is the same for the imaginary part of the impedances. The Eq. A2.3 represents the simple circumstance that these two CPE-s in parallel have both admittances which magnitudes differ from each other by the factor of E.

The Eq. A2.4 represents similar consideration like the latter, but there are compared phases of both admittances which differ from each other by some additive term B.

Calculation suit of Mathcad 13 gives the set of analytic solutions to the system of equations of Eq. A2.1a, A2.2a, A2.3 and A2.4 with the symbolic solver.

These solutions can be studied analytically in respect of parameters of E and B in the same way as there is reported in chapters 1.6 – 1.7 and 3.5.3 – 3.5.6.

APPENDIX A3

PAPER I

APPENDIX A4

PAPER II

K. Laes, S. Bereznev, A. Tverjanovich, E.N. Borisov, T. Varema, O. Volobujeva, A. Öpik, Shallow defect density determination in CuIn₃Se₅ thin film photoabsorber by impedance spectroscopy, *Thin Solid Films, Volume 517, Issue 7, 2 February 2009, Pages 2286-2290*

APPENDIX A5

PAPER III

K. Laes, S. Bereznev, R. Land, A. Tverjanovich, O. Volobujeva, R. Traksmaa, T. Raadik, A. Öpik, The impedance spectroscopy of $CuIn_3Se_5$ photoabsorber films prepared by high vacuum evaporation technique, *Energy Procedia 2010*

APPENDIX B

ELULOOKIRJELDUS

1. Isikuandmed
   Ees- ja perekonnanimi   Kristjan Laes
   Sünniaeg ja -koht   4. 5. 1975, Tallinn Eesti
   Kodakondsus   Eesti Vabariik

2. Kontaktandmed
   Aadress   Järveotsa tee 2-71
   Telefon   6 20 28 21 (töö), 7 44 11 27 (kodu)
   E-posti aadress   kristjan.laes@gmail.com

3. Hariduskäik

Õppeasutus (nimetus lõpetamise ajal)	Lõpetamise aeg	Haridus (eriala/kraad)
Tartu Ülikool, Füüsika-keemia teaduskond, keemia	2004	füüsikaline ja elektrokeemia / MSc
Tartu Ülikool, Füüsika-keemia teaduskond, keemia	2001	keemia / BSc
Tallinna Nõmme Keskkool	1993	keskharidus

4. Keelteoskus (alg-, kesk- või kõrgtase)

Keel	Tase
eesti	kõrgtase
vene	kesktase
inglise	kesktase
saksa	algtase
soome	algtase

5. Täiendusõpe

Õppimise aeg	**Täiendusõppe läbiviija nimetus**
13–15 juuli 2009	International School on Organic Photovoltaics, Valencia, Hispaania
16–17 juuli 2009	Impedance Spectroscopy School 09, Jaume I Ülikool, Hispaania
2006–2008	Materjaliteaduse ja materjalitehnoloogia Doktorikool
Nov 2007	ELIS, Genti Ülikool, Belgia

6. Teenistuskäik

Töötamise aeg	**Tööandja nimetus**	**Ametikoht**
2009– käesoleva ajani	Tallinna Tehnikaülikool, Materjaliteadus Instituut	teadur
2006–2009	Tallinna Tehnikaülikool, Materjaliteadus Instituut	erakorraline teadur
2005–2006	Tehnilise Tõlke Keskus OÜ	keeletoimetaja/tõlk
2004–2005	Tallinna Tehnikaülikool, Keemiatehnika Instituut	tehniline töötaja

7. Kaitstud lõputööd

Tetrabutüülammooniumjodiidi adsorptsioonikineetika Bi(011) elektroodi tahul, magistritöö juhendajad vanemteadur Mart Väärtnõu, prof Enn Lust

Tetrabutüülammooniumjodiidi adsorptsioon vismuti monokristalli tahul (01-1), bakalaureusetöö, juhendajad teadur Gunnar Nurk, prof Enn Lust

8. Teadustöö põhisuunad

CISe fotoabsorbermaterjalid päikeseenergeetikas, impedantsispektroskoopia

CURRICULUM VITAE

1. Personal data
    Name   Kristjan Laes
    Date and place of birth   4th of May 1975, Tallinn Estonia

2. Contact information
    Address   Järveotsa tee 2-71
    Phone   372 6 20 28 21, 372 7 44 11 27
    E-mail   kristjan.laes@gmail.com

3. Education

Educational institution	Graduation year	Education (field of study/degree)
University of Tartu, Department of Physics and Chemistry, Institute of Chemistry	2004	Physical and electrochemistry / MSc
University of Tartu, Department of Physics and Chemistry, Institute of Chemistry	2001	Chemistry / BSc
Tallinn Nõmme Highschool	1993	Secondary education

4. Language competence/skills (fluent; average, basic skills)

Language	Level
estonian	fluent
russian	average
inglish	average
finnish	basic skills
german	basic skills

5.   Special Courses

Period	Educational or other organisation
13–15 july 2009	International School on Organic Photovoltaics, Valencia, Spain
16–17 july 2009	Impedance Spectroscopy School 09, University of Jaume I, Spain
Nov 2007	ELIS, University of Gent, Belgium
2006–2008	Doctoral School of Materials Sciense and Materials Technology

6.   Professional Employment

Period	Organisation	Position
2009–up to now	Tallinn University of Technology, Department of Material Science	researcher
2006–2009	Tallinn University of Technology, Department of Material Science	extraordinary researcher
2005–2006	Tehnilise Tõlke Keskus OÜ	editor and translator
2004–2005	Tallinn University of Technology, Department of Chemical engineering	technical assistant

7.   Defended theses

Adsorption kinetics of tetrabutylammonium cations on Bi(01-1) plane, master thesis (advisors: senior researcher Mart Väärtnõu, prof Enn Lust).

The Adsorption of Tetrabutylammoniumiodide At Bismuth (01-1) Grane, bachelor thesis (advisors: researcher Gunnar Nurk, prof Enn Lust).

8.   Main areas of scientific work/Current research topics

CISe photoabsorber materials in solar cell applications, impedance spectroscopy application in material research

9.   Publications

1)   Tverjanovich, A., Bereznev, S., Borisov, E.N., Kim, D., Kois, J., Laes, K., Volobujeva, O., Öpik, A., Mellikov, E., Tveryanovich, Yu.S. (2009). Polycrystalline $CuIn_3Se_5$ thin film photoabsorber deposited by pulsed laser deposition technique. Proceedings of the Estonian Academy of Sciences, 58(1), 24 - 28.

2)   Laes, K., Bereznev, S., Tverjanovich, A., Borisov, E.N., Varema, T., Volobujeva, O., Öpik, A. (2009). Shallow defect density determination in $CuIn_3Se_5$ thin film photoabsorber by impedance spectroscopy. Thin Solid Films, 517(7), 2286 - 2290.

3)   Laes, K., Bereznev, S., Land, R., Tverjanovich, Raadik, T., Traksmaa, R., A., Öpik, A. (2009). The impedance spectroscopy of well-oriented $CuIn_3Se_5$ films prepared by high vacuum evaporation technique. In: EMRS-2009 Spring Meeting, Strasbourg, France, June 8 – 12, 2009, Symposium B: EMRS-2009 Spring Meeting, Strasbourg, France, June 8 – 12, 2009. Strasbourg, France:, 2009, 46.

4)   Laes, K., Bereznev, S., Tverjanovich, A., Traksmaa, R., Raadik, T., Öpik, A. (2009). Morphology, electrical and optical characterization of oriented $CuIn_3Se_5$ films prepared by high vacuum evaporation technique. In: 3rd Nordic PV Conference, Catalogue of Abstracts: 3rd Nordic PV Conference, 18-19 May 2009, Tallinn, Estonia. (Toim.) TTÜ. Tallinn:, 2009, 14 - 15.

5)   Bereznev, S., Volobujeva, O., Laes, K., Kois, J., Öpik, A. (2008). Highly conductive PEDOT-PSS back contact layer for CdTe photoabsorber layer in the solar cell. In: ICSM-2008 International Conference of Science and Technology of Synthetic Metals. Book of Abstracts. : ICSM-2008 International Conference of Science and Technology of Synthetic Metals, Porto de Galinhas, Brazil, July 6-11, 2008. (Toim.) ICSM 2008 Organizing Committee. Brazil:, 2008, 160.

6)   Laes, K., Kasuk, H., Nurk, G., Vaartnou, M., Lust, K., Janes, A., Lust, E. (2004). Adsorption kinetics of tetrabutylammonium cations on Bi(011) plane. Journal of Electroanalytical Chemistry, 569(2), 241 - 256.

DISSERTATIONS DEFENDED AT
TALLINN UNIVERSITY OF TECHNOLOGY ON
NATURAL AND EXACT SCIENCES

1. **Olav Kongas**. Nonlinear dynamics in modeling cardiac arrhytmias. 1998.

2. **Kalju Vanatalu**. Optimization of processes of microbial biosynthesis of isotopically labeled biomolecules and their complexes. 1999.

3. **Ahto Buldas**. An algebraic approach to the structure of graphs. 1999.

4. **Monika Drews**. A metabolic study of insect cells in batch and continuous culture: application of chemostat and turbidostat to the production of recombinant proteins. 1999.

5. **Eola Valdre**. Endothelial-specific regulation of vessel formation: role of receptor tyrosine kinases. 2000.

6. **Kalju Lott**. Doping and defect thermodynamic equilibrium in ZnS. 2000.

7. **Reet Koljak**. Novel fatty acid dioxygenases from the corals *Plexaura homomalla* and *Gersemia fruticosa.* 2001.

8. **Anne Paju**. Asymmetric oxidation of prochiral and racemic ketones by using sharpless catalyst. 2001.

9. **Marko Vendelin**. Cardiac mechanoenergetics *in silico*. 2001.

10. **Pearu Peterson**. Multi-soliton interactions and the inverse problem of wave crest. 2001.

11. **Anne Menert**. Microcalorimetry of anaerobic digestion. 2001.

12. **Toomas Tiivel**. The role of the mitochondrial outer membrane in *in vivo* regulation of respiration in normal heart and skeletal muscle cell. 2002.

13. **Olle Hints**. Ordovician scolecodonts of Estonia and neighbouring areas: taxonomy, distribution, palaeoecology, and application. 2002.

14. **Jaak Nõlvak**. Chitinozoan biostratigrapy in the Ordovician of Baltoscandia. 2002.

15. **Liivi Kluge**. On algebraic structure of pre-operad. 2002.

16. **Jaanus Lass**. Biosignal interpretation: Study of cardiac arrhytmias and electromagnetic field effects on human nervous system. 2002.

17. **Janek Peterson**. Synthesis, structural characterization and modification of PAMAM dendrimers. 2002.

18. **Merike Vaher**. Room temperature ionic liquids as background electrolyte additives in capillary electrophoresis. 2002.

19. **Valdek Mikli**. Electron microscopy and image analysis study of powdered hardmetal materials and optoelectronic thin films. 2003.

20. **Mart Viljus**. The microstructure and properties of fine-grained cermets. 2003.

21. **Signe Kask**. Identification and characterization of dairy-related *Lactobacillus*. 2003.

22. **Tiiu-Mai Laht**. Influence of microstructure of the curd on enzymatic and microbiological processes in Swiss-type cheese. 2003.

23. **Anne Kuusksalu**. 2–5A synthetase in the marine sponge *Geodia cydonium*. 2003.

24. **Sergei Bereznev**. Solar cells based on polycristalline copper-indium chalcogenides and conductive polymers. 2003.

25. **Kadri Kriis**. Asymmetric synthesis of C_2-symmetric bimorpholines and their application as chiral ligands in the transfer hydrogenation of aromatic ketones. 2004.

26. **Jekaterina Reut**. Polypyrrole coatings on conducting and insulating substracts. 2004.

27. **Sven Nõmm**. Realization and identification of discrete-time nonlinear systems. 2004.

28. **Olga Kijatkina**. Deposition of copper indium disulphide films by chemical spray pyrolysis. 2004.

29. **Gert Tamberg**. On sampling operators defined by Rogosinski, Hann and Blackman windows. 2004.

30. **Monika Übner**. Interaction of humic substances with metal cations. 2004.

31. **Kaarel Adamberg**. Growth characteristics of non-starter lactic acid bacteria from cheese. 2004.

32. **Imre Vallikivi**. Lipase-catalysed reactions of prostaglandins. 2004.

33. **Merike Peld**. Substituted apatites as sorbents for heavy metals. 2005.

34. **Vitali Syritski**. Study of synthesis and redox switching of polypyrrole and poly(3,4-ethylenedioxythiophene) by using *in-situ* techniques. 2004.

35. **Lee Põllumaa**. Evaluation of ecotoxicological effects related to oil shale industry. 2004.

36. **Riina Aav**. Synthesis of 9,11-secosterols intermediates. 2005.

37. **Andres Braunbrück**. Wave interaction in weakly inhomogeneous materials. 2005.

38. **Robert Kitt**. Generalised scale-invariance in financial time series. 2005.

39. **Juss Pavelson**. Mesoscale physical processes and the related impact on the summer nutrient fields and phytoplankton blooms in the western Gulf of Finland. 2005.

40. **Olari Ilison**. Solitons and solitary waves in media with higher order dispersive and nonlinear effects. 2005.

41. **Maksim Säkki**. Intermittency and long-range structurization of heart rate. 2005.

42. **Enli Kiipli**. Modelling seawater chemistry of the East Baltic Basin in the late Ordovician–Early Silurian. 2005.

43. **Igor Golovtsov**. Modification of conductive properties and processability of polyparaphenylene, polypyrrole and polyaniline. 2005.

44. **Katrin Laos**. Interaction between furcellaran and the globular proteins (bovine serum albumin β-lactoglobulin). 2005.

45. **Arvo Mere**. Structural and electrical properties of spray deposited copper indium disulphide films for solar cells. 2006.

46. **Sille Ehala**. Development and application of various on- and off-line analytical methods for the analysis of bioactive compounds. 2006.

47. **Maria Kulp**. Capillary electrophoretic monitoring of biochemical reaction kinetics. 2006.

48. **Anu Aaspõllu.** Proteinases from *Vipera lebetina* snake venom affecting hemostasis. 2006.

49. **Lyudmila Chekulayeva**. Photosensitized inactivation of tumor cells by porphyrins and chlorins. 2006.

50. **Merle Uudsemaa**. Quantum-chemical modeling of solvated first row transition metal ions. 2006.

51. **Tagli Pitsi**. Nutrition situation of pre-school children in Estonia from 1995 to 2004. 2006.

52. **Angela Ivask**. Luminescent recombinant sensor bacteria for the analysis of bioavailable heavy metals. 2006.

53. **Tiina Lõugas**. Study on physico-chemical properties and some bioactive compounds of sea buckthorn (*Hippophae rhamnoides* L.). 2006.

54. **Kaja Kasemets**. Effect of changing environmental conditions on the fermentative growth of Saccharomyces cerevisae S288C: auxo-accelerostat study. 2006.

55. **Ildar Nisamedtinov**. Application of ^{13}C and fluorescence labeling in metabolic studies of Saccharomyces spp. 2006.

56. **Alar Leibak**. On additive generalisation of Voronoï's theory of perfect forms over algebraic number fields. 2006.

57. **Andri Jagomägi**. Photoluminescence of chalcopyrite tellurides. 2006.

58. **Tõnu Martma**. Application of carbon isotopes to the study of the Ordovician and Silurian of the Baltic. 2006.

59. **Marit Kauk**. Chemical composition of CuInSe$_2$ monograin powders for solar cell application. 2006.

60. **Julia Kois**. Electrochemical deposition of CuInSe$_2$ thin films for photovoltaic applications. 2006.

61. **Ilona Oja Açik**. Sol-gel deposition of titanium dioxide films. 2007.

62. **Tiia Anmann**. Integrated and organized cellular bioenergetic systems in heart and brain. 2007.

63. **Katrin Trummal**. Purification, characterization and specificity studies of metalloproteinases from *Vipera lebetina* snake venom. 2007.

64. **Gennadi Lessin**. Biochemical definition of coastal zone using numerical modeling and measurement data. 2007.

65. **Enno Pais**. Inverse problems to determine non-homogeneous degenerate memory kernels in heat flow. 2007.

66. **Maria Borissova**. Capillary electrophoresis on alkylimidazolium salts. 2007.

67. **Karin Valmsen**. Prostaglandin synthesis in the coral *Plexaura homomalla*: control of prostaglandin stereochemistry at carbon 15 by cyclooxygenases. 2007.

68. **Kristjan Piirimäe**. Long-term changes of nutrient fluxes in the drainage basin of the gulf of Finland – application of the PolFlow model. 2007.

69. **Tatjana Dedova**. Chemical spray pyrolysis deposition of zinc sulfide thin films and zinc oxide nanostructured layers. 2007.

70. **Katrin Tomson**. Production of labelled recombinant proteins in fed-batch systems in *Escherichia coli*. 2007.

71. **Cecilia Sarmiento**. Suppressors of RNA silencing in plants. 2008.

72. **Vilja Mardla**. Inhibition of platelet aggregation with combination of antiplatelet agents. 2008.

73. **Maie Bachmann**. Effect of Modulated microwave radiation on human resting electroencephalographic signal. 2008.

74. **Dan Hüvonen**. Terahertz spectroscopy of low-dimensional spin systems. 2008.

75. **Ly Villo**. Stereoselective chemoenzymatic synthesis of deoxy sugar esters involving *Candida antarctica* lipase B. 2008.

76. **Johan Anton**. Technology of integrated photoelasticity for residual stress measurement in glass articles of axisymmetric shape. 2008.

77. **Olga Volobujeva**. SEM study of selenization of different thin metallic films. 2008.

78. **Artur Jõgi**. Synthesis of 4'-substituted 2,3'-dideoxynucleoside analogues. 2008.

79. **Mario Kadastik**. Doubly charged Higgs boson decays and implications on neutrino physics. 2008.

80. **Fernando Pérez-Caballero**. Carbon aerogels from 5-methylresorcinol-formaldehyde gels. 2008.

81. **Sirje Vaask**. The comparability, reproducibility and validity of Estonian food consumption surveys. 2008.

82. **Anna Menaker**. Electrosynthesized conducting polymers, polypyrrole and poly(3,4-ethylenedioxythiophene), for molecular imprinting. 2009.

83. **Lauri Ilison**. Solitons and solitary waves in hierarchical Korteweg-de Vries type systems. 2009.

84. **Kaia Ernits**. Study of In_2S_3 and ZnS thin films deposited by ultrasonic spray pyrolysis and chemical deposition. 2009.

85. **Veljo Sinivee**. Portable spectrometer for ionizing radiation "Gammamapper". 2009.

86. **Jüri Virkepu**. On Lagrange formalism for Lie theory and operadic harmonic oscillator in low dimensions. 2009.

87. **Marko Piirsoo**. Deciphering molecular basis of Schwann cell development. 2009.

88. **Kati Helmja**. Determination of phenolic compounds and their antioxidative capability in plant extracts. 2010.